FAST SOLUTION OF DYADIC GREEN'S FUNCTIONS FOR PLANAR MULTILAYERED MEDIA

DING PINGPING

NATIONAL UNIVERSITY OF SINGAPORE

AND

ÉCOLE SUPÉRIEURE D'ÉLECTRICITÉ

2011

FAST SOLUTION OF DYADIC GREEN'S FUNCTIONS FOR PLANAR MULTILAYERED MEDIA

DING PINGPING

(B. ENG. UESTC, M. ENG. WUHAN UNIVERSITY)

A THESIS SUBMITTED FOR

THE JOINT DEGREE OF DOCTOR OF PHILOSOPHY

DEPARTMENT OF ELECTRICAL AND COMPUTER ENGINEERING

NATIONAL UNIVERSITY OF SINGAPORE AND

ÉCOLE SUPÉRIEURE D'ÉLECTRICITÉ

2011

Acknowledgments

First and foremost, I would like to give my wholehearted thanks and gratitude to my supervisors, Prof. Swee-Ping Yeo, Prof. Cheng-Wei Qiu, and Prof. Saïd Zouhdi, who offer me the opportunity to learn about the theory of electromagnetic waves and fields, recommend me to the NUS-Supélec Joint PhD programme and provide constant support and inestimable guidance for this research work. I am particularly grateful to Professor Le-Wei Li, who taught me a lot about dyadic Green's function when he was at NUS. Moreover, I am also indebted to many people in the faculty and staff of Department of Electrical and Computer Engineering who assisted and encouraged me in various ways during my research studies.

I would like to thank all my fellow graduates in microwave group, who are Dr. Tao Yuan, Dr. Yu Zhong, Dr. Yu-Ming Wu, Ms. Hui-Zhe Liu, Ms. Xiu-Zhu Ye, Ms. Xuan Wang, Mr. Hua-Peng Ye and Mr. Jack Ng, for their helpful discussions of research work and sincere friendship. I am also thankful to the kind help from Ms. Yu Zhu, Dr. Pei-Qing Yu and Ms. Samantha Lacroix when I was studying in Supélec, France.

Last but not least, I am deeply grateful to my dear grandparents, parents, brother and boyfriend, for their constant encouragement and support and never-ending love.

ABSTRACT

Integral equation methods have been a versatile tool for the electromagnetic analysis of microwave integrated circuits implemented in planar multilayered substrates. The electric and magnetic fields in the multilayered structures can be easily derived from the dyadic Green's function. Consequently, a large amount of research work has been dedicated to the study of fast methods for calculating the dyadic Green's functions in the multilayered media.

The fast Hankel transform filter technique has been proved to be an efficient method for calculating the dyadic Green's functions. However, the fast Hankel transform method is only applicable for shielded multilayered geometries, due to the branch-point singularity. To overcome this limitation, the proposed modified fast Hankel transform method deforms the integration path of Sommerfeld integral from the real axis to the quadrant and the Bessel function with a complex argument is expanded as a sum of terms. Numerical results confirm that the modified fast Hankel transform method has a good performance in accuracy and wide applications.

The discrete complex image method, the window function method and the modified fast Hankel transform method are three popular fast techniques for calculating the dyadic Green's functions in a multilayered medium. In order to provide detailed knowledge of

the accuracy, efficiency and application range of the three fast methods, the robustness and efficiency of the three methods are carefully examined. The results indicate that discrete complex image method is effective for general multilayered cases and modified fast Hankel transform method is also a powerful tool, while the accuracy and efficiency of window function method is strongly dependent on the multilayered geometry.

Next, another aim of the research work is to systematically derive the spectral-domain Green's function used in the electric field integral equation for the multilayered uniaxial anisotropic medium and gyrotropic medium. Then, the spatial-domain Green's functions in the two kinds of media are calculated based on the fast methods. More importantly, the influence of material's anisotropy upon these dyadic Green's functions is investigated. The *kDB* coordinate system is exploited and integrated with the wave iterative technique to derive the spectral-domain Green's function. From the view of numerical results, it can be deduced that the dyadic Green's functions in both the spectral domain and spatial domain for the multilayered uniaxial anisotropic medium and gyrotropic medium are very accurate.

In conclusion, this study is the first to provide valuable insight into the merits and limitations of three popular fast methods for calculating the dyadic Green's functions in a multilayered medium. Moreover, the spatial-domain Green's functions in the multilayered uniaxial anisotropic medium and gyrotropic medium are successfully obtained for the first time. Finally, in view of the increasing application of anisotropic media to the integrated circuits and microstrip antenna, it is worthwhile to employ the dyadic Green's functions associated with the method of moments to analyze their properties for the future research study.

Contents

List of Figures

List of Tables

List of Abbreviations

DCIM Discrete Complex Image Method

DGF Dyadic Green's Function

DNI Direct Numerical Integration

EFIE Electric Field Integral Equation

FHT Fast Hankel Transform

GPOF Generalized Pencil of Function

MFHT Modified Fast Hankel Transform

MMIC Millimeter-Wave Integrated Circuits

MoM Method of Moments

MPIE Mixed Potential Integral Equation

PEC Perfect Electric Conducting

SDP Steepest Descent Path

SI Sommerfeld Integral

SIP Sommerfeld Integration Path

SWP Surface Wave Pole

TE Transverse Electric

TM Transverse Magnetic

VWEET Vector Wave Eigenfunction Expansion Technique

WFM Window Function Method

WIT Wave Iterative Technique

Chapter 1

Introduction

One of the most interesting research topics in computational electromagnetics is the study of wave interactions with the planar multilayered media. The attraction in this subject stems from its relevance to numerous applications of practical interests, ranging from geophysical prospecting and remote sensing [1, 2, 3, 4] to the electromagnetic performance prediction of microwave antennas [5, 6, 7, 8, 9] and waveguides for microwave/ millimeter-wave integrated circuits (MMIC) [10, 11, 12, 13, 14, 15, 16, 17, 18]. It is widely accepted that the method of moments (MoM) is one of the most commonly used numerical techniques for the rigorous analysis of multilayered problems [19, 20, 21, 22, 23, 24, 25]. In the case of multilayered problems, the application of MoM for the solution of integral equations, either in spectral domain or spatial domain, usually requires the knowledge of dyadic Green's functions (DGF's) in the corresponding domain [26, 27, 28, 29]. The DGF's for a multilayered medium are obtained in closed-form expressions in the spectral domain, and are generally represented by the Sommerfeld integrals (SI's) in the spatial domain from their spectral-domain counterparts [30]. How-

ever, the numerical direct integration of SI's is a time-consuming and computationally expensive procedure due to the oscillating and slowly decaying behavior of the integrands [31, 32, 33]. Consequently, a considerable amount of research work has been dedicated to the development of methodologies used for calculating the spatial-domain Green's functions accurately and efficiently for a multilayered medium over the decades [34, 35, 36, 20, 37, 38, 39, 40, 41]. Among these methodologies, the most popular ones are the discrete complex image method (DCIM) [42, 43, 44, 45, 46, 47, 48, 49, 50, 51], the fast Hankel transform (FHT) method [52, 16, 53], the steepest descent path (SDP) method [30, 54], and the window function method (WFM) [55].

Although the spectral-domain Green's function and spatial-domain Green's function for the multilayered isotropic medium have been derived and discussed comprehensively in previous research work, the DGF's for the multilayered anisotropic media have not been systematically studied so far due to the complexity of wave propagation in the anisotropic media. Besides the application range of MMIC and microwave antennas, anisotropic materials have also been found to have important applications in optical devices and radar absorbing materials [18, 56, 57, 58, 59, 60]. Due to the emergence of practical application of anisotropic materials in multilayered geometries [61, 62, 63, 64, 65], the accurate and expedient calculation of the multilayered Green's function in both the spectral and spatial domains is highly necessary and important as a characterization tool. Several algorithms have been proposed for the derivation of the spectral-domain Green's function in the multilayered anisotropic media, e.g., vector wave eigenfunction expansion technique (VWEET) [66, 67] and wave iterative technique (WIT) [68, 69, 70].

This chapter will provide a brief overview of field integral equation and potential integral equation and four popular fast methods for calculating the multilayered DGF's. Then the attention will be given to the derivation of spectral-domain Green's function for a multilayered anisotropic medium.

1.1 Method of Moments in Spatial Domain

It is known that the MoM analysis can be carried out either in the spectral domain [71, 72, 73, 74, 75] or the spatial domain [76, 77, 78]. The spectral-domain method is often applied to regularly shaped structures since the basis functions are usually selected to be those with analytical Fourier transforms. One pitfall of this method is the necessity of laborious evaluation of double infinite integration to generate the impedance matrix. Compared with the spectral-domain method, the spatial-domain method provides better physical insight since the problem remains in the physical domain. The basis functions can be arbitrary, which renders the approach very versatile. It is known that two popular equations used for the MoM in the spatial domain to solve the multilayered media problems are the electric field integral equation (EFIE) and the mixed potential integral equation (MPIE).

1.1.1 Electric Field Integral Equation

The EFIE used in MoM is an effective method to treat the scattering problems by buried objects [79, 54]. The general procedures for the EFIE applied to surface scatterers are to split the field at conducting surfaces into incident and scattered fields, and then, to

satisfy the appropriate surface boundary conditions. The scattered field is expressed by the standard kernel of the EFIE, which is expressed by the Green's functions in the corresponding environment.

Compared with the MPIE, one major advantage of the EFIE is that the EFIE can be utilized to handle the multilayered anisotropic media problems. Some researchers have conducted the studies of deriving spectral-domain Green's function, used in EFIE, for the multilayered anisotropic media recently and provided useful experience and knowledge from such studies. In the early work, Tsalamengas (1985, 1989, 1990) studied the electromagnetic fields in the form of DGF's and the radiation properties from an arbitrarily oriented dipole in the presence of the multilayered gyrotropic medium [80, 81, 82]. Ali et al. (1992) derived the formulation of the spectral-domain Green's function for a multilayered chiral medium resulting from the arbitrary distribution of sources, and expressed the fields in terms of electric- and magnetic-type dyadic Green's functions. Tan et al. (2001) utilized the cylindrical wave vector functions to derive the spectral-domain Green's functions for planar multilayered bianisotropic media, used in the EFIE [83]. Subsequently, Li et al. (2004) presented a complete eigenfunction expansion of the DGF's for planar, arbitrary multilayered anisotropic media in terms of cylindrical vector wave functions [67]. It can be deduced that the employment of the EFIE in MoM may provide a powerful tool to deal with the multilayered anisotropic media problems.

However, as pointed out by Michalski and Zheng (1990), for the multilayered isotropic or uniaxial anisotropic medium, the EFIE is not attractive since it has a highly singular kernel, which makes the evaluation of the SI's required by the MoM procedure difficult when the observation point is within the integration interval [20]. In addition, it

should be noted that another drawback of the EFIE is that the required differentiation of the SI's adversely affects their convergence, which results in the slow convergence of the kernels of EFIE. These difficulties can be avoided by introducing one of divergent operators inside the integral and then transferring it to act on the current by a series of transformations. The solution is the mixed potential integral equation discussed below.

1.1.2 Mixed Potential Integral Equation

The continuous theoretical and numerical developments of the MPIE have made it one of the most efficient computational tools for the analysis of printed microwave circuits and antennas [84, 85, 20, 24, 86, 87]. It is widely accepted that the efficiency of the MPIE to deal with an arbitrarily distributed source in the multilayered medium relies on the accurate and fast calculation of the Green's functions related to the vector and scalar potentials. The distinguishing feature of the MPIE is that the vector and scalar potentials are employed and expressed in terms of the current and charge densities, respectively.

A lot of research work has been done to demonstrate the advantages of the MPIE in solving antenna problems in the multilayered medium. Mosig and Gardiol applied the MPIE in conjunction with Glisson and Wilton's MoM procedure to a rectangular microstrip antenna [88, 89]. Subsequently, Johnson used a similar approach to solve the problem of a vertical cylinder penetrating the interface between contiguous half-spaces [90]. The utilization of the MPIE to non-planar conductors in multilayered media was later proposed by Michalski [91]. Then, Michalski and Zheng developed three alternative MPIE formulations [20] for multilayered media, referred to as Formulation A, B,

and C [92]. Later, the formulation C was applied to the analysis of microstrip transmission lines of arbitrary cross section [93] and vertical probe-fed microstrip patch antennas [94]. Furthermore, the modified formulations of MPIE were proposed, in which the expression of scalar potential is added by a correction term [95, 96]. Recently, Liu et al. applied the formulation C of MPIE to the simulation of three-dimensional perfectly electrical conduction objects in the multilayered medium [44]. Based on the above review, it can be seen that the MPIE associated with the MoM paved the way for the simulation of the scattering of three-dimensional objects in the multilayered medium.

As mentioned above, the MPIE formulations are preferable to other forms of the EFIE, because they involve less singular kernels and faster convergent spectral integrals, and are amenable to the well-established MoM solution procedures, originally developed for arbitrarily shaped conducting scatterers in free space [19, 88, 85]. Although the great versatility of the MPIE makes it one of the most popular methods in the multilayered problems, one limitation of the MPIE procedure is its inability to deal with multilayered media problems other than isotropic and uniaxial anisotropic media. Since two distinct characteristic waves of the anisotropic medium, type I wave and type II wave, are coupled to each other, the transmission line method used for the derivation of MPIE cannot be used anymore. Thus, the derivation of MPIE in the anisotropic medium may be impossible.

In view of the two issues presented above, i.e., the highly singular kernel of EFIE for the multilayered isotropic medium, as well as the inability of MPIE to deal with the multilayered anisotropic media problems, the EFIE is the preferred choice for handling the multilayered anisotropic problems, while the MPIE is more suitable for studying the

multilayered isotropic problems.

1.2 Fast Methods for Calculating Dyadic Green's Function

The efficiency of both EFIE and MPIE mainly depends on the evaluation of the spatial-domain Green's functions. The calculation of DGF's includes two tedious steps. The first step is to derive the spectral-domain Green's functions analytically, which gives rise to many lengthy expressions of the spectral functions for different combinations of source and field locations in the multilayered geometry. The second step is to calculate the spatial-domain Green's functions from the inverse Fourier transforms of the spectral-domain Green's functions, which are referred to Sommerfeld integrals. The numerical evaluation of this integral usually requires the integration path along the real axis from $-\infty$ to $+\infty$ for each operating frequency and each combination of source and field locations. Generally speaking, the analytical solution of SI's is unavailable, and the numerical integration of SI's is a tedious task due to the highly oscillating and slowly decaying behavior of the integrands and the singularities near the integration path. Since these integrals must be repetitiously evaluated in filling the MoM matrix, to accelerate the integration is of paramount importance and has been an attractive research subject. In the last decades, to accelerate the integration, extensive research work has focused on the development of fast algorithms used for calculating the spatial-domain Green's functions in the multilayered media. Since theoretical investigation of this subject has

extended over many years, it is desirable to present a brief historical sketch of various developments. Next, we will present a detailed review of four popular fast methods: discrete complex image method, the steepest descent path method, the window function method, and the fast Hankel transform method.

1.2.1 Discrete Complex Image Method

The essence of DCIM is to approximate the spectral-domain Green's function in terms of complex exponentials using either the generalized pencil of function (GPOF) method or the Prony's method. Then, these exponentials are transformed into a set of complex images analytically in the spatial domain with the use of the Sommerfeld identity.

The first research work published on this method for the multilayered problems was carried out by Fang et al. in 1988 [98]. However, there were two issues that rendered this method ineffective. The first issue is the lack of accuracy of the approximation results at the intermediate and far fields. The other one is the noise sensitivity and instability brought from the exponential approximation algorithm, the Prony's method [99]. As a result, they computed the DGF's by using DCIM only within the near field, beyond which the contribution of surface-wave poles (SWP's) was used to represent the DGF's. However, the difficulty of predefining the switching point urged the researchers to improve this algorithm which could compute the DGF's over all distance ranges involved. Subsequently, Chow et al. (1991) presented an algorithm to compute the closed-form Green's function for thick microstrip substrates. The contributions of quasi-static terms and the SWP's were extracted, and then, the rest terms of spectral-domain Green's func-

tion were approximated in terms of complex exponentials via the Prony's method. But due to geometry-based extraction of quasi-static terms and noise sensitivity of Prony's method, the modification and improvement of DCIM were inspired. Subsequently, Aksun (1996) proposed the well-known two-level sampling algorithm which could significantly reduce the number of samples required for the exponential approximation [43], in addition to employing a less noise-sensitive method, GPOF [100, 101], for the exponential approximation and unnecessary procedure to extract the geometry-based contribution of quasi-static terms [102]. However, the two-level approach, together with the explicit extraction of the SWP's, is capable of approximating spherical and cylindrical wave components, but not the lateral waves, which are due to the branch points in the spectral-domain. In order to overcome this shortcoming, Alparslan (2010) recently proposed the three-level algorithm [51] to provide a better sampling of the spectral-domain Green's functions around the branch points. But this algorithm is limited only for multilayered structures supporting a single lateral wave component and the complicated procedure of extraction of SWP's is still required.

The DCIM is a major milestone in the development of fast solution for calculating Green's functions associated with MoM, since it can completely avoid the laborious and time-consuming integration of Hankel transform and cast the spatial-domain Green's function into a closed form. Due to the obviation of numerical integration, DCIM affords at least an order-of-magnitude speed-up in the MoM matrix filling time. However, to gain this advantage, the objects should be confined to an invariable vertical position. Also, DCIM has no built-in convergence measures and its accuracy can only be ascertained posteriorly by checking the results against those obtained by numerical in-

tegration. Furthermore, the application of this method in the multilayered medium is currently impeded by the lack of reliable automated procedures for locating SWP's.

1.2.2 Fast Hankel Transform Method

The FHT method transforms the SI's with a smooth spectral-domain Green's function into a linear discrete convolution in the spatial domain. The convolution results can be considered as the system response of a linear filter. The linear filter method for calculating Hankel transform has been a research subject of numerous papers in the geophysical literature since it was introduced by Ghosh [103, 104]. At the beginning, the research work mainly focused on short filters with a limited number of coefficients [105, 106]. Bernabini et al. (1975) later obtained the filter coefficients by direct integration of the convolution integral containing the Bessel function [107]. Then, Anderson presented a widely used FORTRAN computer routine capable of performing a Hankel transform of order 0 and 1 [108, 109]. Subsequently, Christensen (1990) developed an approach to the calculation of the filter coefficients for the optimized digital filters [110]. In this approach, the sampling density of filter length is minimized by choosing the parameters determining the filter characteristics according to the analytical properties of the input function. Recently, Hsieh et al. (1998) firstly applied the FHT algorithm to the calculation of spatial-domain Green's functions for the analysis of planar microstrip circuits.

However, since the FHT only provides an efficient procedure for computing the integration with a smooth input function, the accuracy and efficiency of this method applied to the SI's are mainly dependent on how to obtain a smooth amplitude of the spectral-

domain Green's function and proper discrete convolution coefficients. When both of the conditions are satisfied, the FHT method can greatly accelerate the calculation of SI's. It is known that for the spectral-domain Green's functions, there are two basic types of singularities, i.e., the SWP's singularities and the branch-point singularities. In order to obtain a smooth amplitude of spectral-domain Green's function, it is necessary to locate the positions of SWP's and extract their contribution from the spectral-domain Green's function. Then the contribution in the spatial domain is analytically evaluated via the residue calculus technique. Although various techniques [32, 111, 33, 49] have been proposed to extract the contribution of SWP's, it is still complicated to accurately locate their positions, and more importantly, it is still lack of reliable automated procedures for the extraction of SWP's. Furthermore, the branch-point singularity is unavoidable along the integration path of the traditional FHT method, e.g., in the case of semi-open and open multilayered structures. Hence, until now, the FHT method was only applicable to shielded multilayered geometries, which is due to the fact that the branch-point singularities are associated with the outermost layers and only absent for the shielded multilayered geometry. There is thus a desirable need to modify and improve the traditional FHT method to power more applications to the general multilayered structure problems.

1.2.3 Steepest Descent Path Method

The method of steepest descent path deals with asymptotic expansion of an integral with an exponential term. A saddle point is a point in the domain of a function that is a station-

ary point and the constant-phase path on the exponential function descends steeply away from the saddle point, which is known as the steepest descent path. Cui et al. (1999) first introduced the SI's along SDP and the leading-order approximations to speed up the computation of spatial-domain Green's function for the multilayered medium [54]. However, a serious shortcoming of this method is that the saddle points have to be determined corresponding to the different exponential terms in the formulations of spectral-domain Green's functions, which is a computationally intractable procedure, especially in the case of scatterers penetrating different layers in the multilayered geometry. Another problem with this method is that the steepest-descent path corresponding to each saddle point also has to be computed before the integration. Therefore, it can be deduced that the SDP method is only effective for the case of multilayered structures with only one or two layers and it is not suitable for solving the general multilayered geometry problems.

1.2.4 Window Function Method

The WFM utilizes a window function as a convolution kernel to the spatial-domain Green's function. The main idea of the convolution with the window function in the spatial domain is equivalent to a low-pass filter in the spectral domain used in signal processing and Gabor transformation in wavelet theory [112]. The fast decaying property of the window function in the spectral domain effectively provides a steep descent path for the SI without the existence or the information of the location of a possible steep descent path for the spectral-domain Green's function. Cai et al. (2000) introduced the

WFM for the calculation of DGF's in the case of analyzing electromagnetic scattering of objects embedded in a multilayered medium. The advantage of this method is that since the integration path is deformed into the first quadrant, the extraction of SWP's singularities is completely avoided. Thus, the computational process of time-consuming SI's can be simplified. Nevertheless, for each combination of source and field locations, the approximation of SI usually requires six integral terms for the calculation of spatial-domain Green's function, which renders this method laborious and complicated. In addition, the precision requirement of calculating the six integrals in the approximation process is quite high, due to a preset small value of the support parameter of the window function. Hence, the efficiency of the window function method may deteriorate significantly because of the high precision requirement.

1.3 Methods for Deriving the Spectral-Domain Green's Function in a Multilayered Anisotropic Medium

As the development of material theory and technology, more and more complex novel materials are analyzed for various applications [113, 114, 115, 116, 117]. Hence, the accurate and expedient calculation of the corresponding dyadic Green's function in both the spectral and spatial domains is highly necessary and important as a characterization tool. Compared to the multilayered isotropic medium, the analytical expressions of DGF's for the multilayered anisotropic media would suffer more severe algebraic complication. Thus, it is a challenging work to obtain the solutions in a compact and

systematic form. Currently, there are two typical techniques for deriving the DGF's in the spectral domain for the multilayered anisotropic medium, which are the vector wave eigenfunction expansion technique (VWEET) and the wave iterative technique (WIT). A brief overview of the two methods is given below.

1.3.1 Vector Wave Eigenfunction Expansion Technique

The main idea of VWEET is to expand the unbounded Green's function in terms of solenoidal and irrotational vector wave functions according to the Ohm-Rayleigh method [66, 118, 64, 119] and the scattered dyadic Green's function is thereafter derived by applying the principle of scattering superposition. The research work on the vector wave functions was first carried out by Hansen (1935) for the analysis of electromagnetic problems [120, 121]. In his work, three kinds of vector wave functions were introduced and denoted by $\boldsymbol{L}$, $\boldsymbol{M}$ and $\boldsymbol{N}$, which are solutions of the homogeneous vector Helmhotz equation. Pathak (1983) described a relatively simple approach for developing the complete eigenfunction expansion of electric and magnetic fields with an arbitrarily oriented electric current point source. The expansion of electric and magnetic fields only contained the solenoidal type eigenfunctions [122]. Later, the vector wave functions were applied to the expansion of Green's function for a planar multilayered medium by Tai [66]. Subsequently, Tan et al. (2001) employed the vector wave expansion approach to derive the spectral-domain Green's functions for planar multilayered bianisotropic media [83]. More recently, Li et al. (2004) presented the cylindrical vector eigenfunction expansion of DGF's for planar multilayered anisotropic media.

The VWEET provides a straightforward methodology for the derivation of DGF's in the multilayered medium, because vector wave functions can be easily applied to the expansion of wave functions. Nevertheless, the expansion coefficients of scattered dyadic Green's function usually cannot be analytically expressed by explicit formulations for an arbitrary number of planar layers. Although the calculation of scattering coefficients is still possible when the medium is composed of one or two layers, it becomes a cumbersome step for the case of multilayered media. Therefore, it is difficult, if not impossible, to employ VWEET for the systematic derivation of DGF's for multilayered anisotropic media.

1.3.2 Wave Iterative Technique

To facilitate discussions on wave behavior and solutions for the fields vectors inside a general homogeneous medium, Kong [123] first established a convenient coordinate system called the *kDB* coordinate system. Habashy et al. (1991) employed the *kDB* coordinate system to obtain the characteristic field vectors and the Fourier transform to derive unbounded Green's function in a planar multilayered gyrotropic medium [70]. Subsequently, based on the boundary condition and WIT, the scattered Green's function in the spectral domain was derived. The spectral-domain Green's functions are expressed in terms of ordinary and extraordinary waves and the derivation process is straightforward and flexible. However, there is one primary problem for the derivation of the spectral-domain Green's function in his work [70]. In the derivation of the Green's function of the total field, the vertical position of one interface of the source

layer has to be set to zero. This implies that, whenever the source position is changed, the whole coordinate system should be reset, which in turn will introduce particular complexity in the implementation of numerical computation. Therefore, the theoretical formulations in [70] are not able to effectively treat general multilayered problems with arbitrary positions of the source.

1.4 Objectives and Significance

In view of the previous review, one primary objective of the present study was to develop the modified fast Hankel transform (MFHT) method by deforming the integration path of SI from the real axis to the quadrant and expand the Bessel function with a complex argument as a sum of terms. Compared to the traditional FHT method, the major merit of the MFHT technique is that it successfully extends the application range to the general multilayered structure problems. The MFHT method should be a valuable and robust development and improvement of the traditional FHT method to calculate the DGF's for a general multilayered structure.

In order to provide detailed knowledge of the accuracy and efficiency and application range of three fast methods, the discrete complex image method, the window function method and the modified fast Hankel transform method, one of aims of the present study is to carefully examine the robustness and efficiency of the three fast methods for calculating the DGF's for a multilayered medium. The comparison of accuracy and efficiency for the three fast methods may have significant impact on both offering a clearer explanation for the advantage and shortcoming of each method and provide

guidelines for the development of computer-aided design tools for the electromagnetic performance prediction of practical problems.

Another aim of the research work is to systematically derive the spectral-domain Green's function used in the electric field integral equation for the multilayered uniaxial anisotropic medium and gyrotropic medium, and then, to calculate the spatial-domain Green's functions in the two kinds of media based on the fast methods, and more importantly, to investigate the influence of material's anisotropy upon the DGF's. The *kDB* coordinate system is exploited and integrated with the WIT to derive the spectral-domain Green's function. This systematic derivation procedure can be easily applied to more complex multilayered media. Moreover, the study of DGF's for the multilayered anisotropic media may be valuable to enhance the understanding of electromagnetic properties in the anisotropic media and pave the path for modeling emerging microwave and optical devices involving composite birefringent materials.

In this thesis, the steepest descent path method is not explicitly discussed. The application of the fast methods is restricted to multilayered isotropic and anisotropic media problems. Studies of other multilayered media are excluded from this work because currently the multilayered problems related with the analysis of the microwave circuits and microstrip antennas mainly deal with isotropic and anisotropic media. It should also be noted that the focus here is the planar multilayered structures; other multilayered structures, i.e., the cylindrical multilayered structure and spherical multilayered structure are beyond the scope of this study.

The fields are assumed to be time-harmonic and, for convenience, the associated factor $e^{i\omega t}$ will not be expressly included throughout this thesis.

1.5 Publications

1. Ping-Ping Ding, Cheng-Wei Qiu, Saïd Zouhdi, Swee-Ping Yeo, "Rigorous Derivation and Fast Solution of Dyadic Green's Functions for Uniaxial Anisotropic Multilayers", *IEEE Trans. Microwave Theory Tech*, vol. 60, no. 2, pp. 205-217, Feb. 2012.

2. Ping-Ping Ding, Cheng-Wei Qiu, Saïd Zouhdi, Swee-Ping Yeo, "Robust Closed-Form Dyadic Green's Functions for Planar Multilayered Uniaxial Anisotropic Media", submitted to *J. Comput. Phys*.

3. Le-Wei Li, Ping-Ping Ding, Saïd Zouhdi, Swee-Ping Yeo, "An Accurate and Efficient Evaluation of Planar Multilayered Green's Functions Using Modified Fast Hankel Transform Method", *IEEE Trans Microwave Theory Tech*, vol. 59, no. 11, pp. 2798-2807, Nov. 2011.

4. Ping-Ping Ding, Saïd Zouhdi, Le-Wei Li, Swee-Ping Yeo, "Closed-form Green's Functions for Stratified Uniaxial Anisotropic Medium", *Piers Online*, vol. 7, no. 2, pp. 136-140, 2011.

5. Ping-Ping Ding, Saïd Zouhdi, Le-Wei Li, Swee-Ping Yeo, Niels Bøie Christensen, "A Modified Fast Hankel Transform Algorithm for Calculating Planar Multilayered Green's Function", *International Conference on Electromagnetics in Advanced Applications*, pp. 47-50, Sep. 2010.

Chapter 2

Modified Fast Hankel Transform Method

2.1 Introduction

The MoM solution to the integral equation has been widely used for handling multilayered media problems. A crucial computational process for the accurate and efficient MoM analysis is the calculation of DGF's for the multilayered media, which are expressed in terms of SI's [92, 124, 24]. An efficient way of evaluating SI's is to use the fast Hankel transform method, which transforms the SI into a linear discrete convolution to improve the computational efficiency. Nevertheless, due to the fact that the traditional FHT technique requires that the integrand should be a smooth input function, the robustness and effectiveness of this method applied to the SI's are mainly determined on how to obtain smooth amplitude of spectral-domain Green's function and correct discrete convolution coefficients. When the two conditions are satisfied, the FHT method can

be applied to the acceleration of the calculation of SI's. In the spectral-domain Green's functions, there are two basic types of singularities, which are the SWP singularities and the branch-point singularities. In order to obtain the smooth amplitude of the spectral-domain Green's function, it is necessary to locate the positions of SWP's and extract their contribution from the spectrum. Then the contribution of SWP's in the spatial domain can be analytically obtained via the residue calculus technique. Although several techniques [32, 111, 33, 49] have been proposed to extract the contribution of the SWP's, to accurately locate all of their positions is still a tedious step, and more importantly, reliable automated procedures for the extraction of the SWP's have not been obtained yet. Furthermore, the branch-point singularity is unavoidable on the integration path of the traditional FHT method, for the case of semi-open and open multilayered structures. This is due to the fact that the branch-point singularities are associated with the outermost layers and only absent for the shielded multilayered geometry. Thus, until now, the traditional FHT method was only applicable to shielded multilayered geometries. There is thus a desirable need to modify and improve the traditional FHT method to extend its application range.

To overcome this limitation, this chapter will propose a modified fast Hankel transform (MFHT) filter algorithm to calculate the spatial-domain Green's functions for the general multilayered geometries. Firstly, the Sommerfeld integral path (SIP) is deformed from the real axis into the first quadrant to move away from the branch-point singularity and the SWP singularity. In this way, without the necessity of extracting the contribution of singularities, a relatively smooth integrand of the SI can be obtained. Secondly, we express the Bessel function with a complex argument in terms of the prod-

uct of a Bessel function with the real part of the argument and another Bessel function with the imaginary part of the argument. For each expansion term, the traditional FHT filter algorithm can be used. Although each term has a different order of Hankel function, the algorithm for the calculation of high-order Hankel transform filter coefficients has been developed by Christensen (1990) [110]. Hence, in this work, we develop the MFHT filter algorithm making use of the FHT filters proposed in [110] which can be readily obtained for high orders. The parameters involved in the deformed integration path and the number of expansion terms determines the accuracy and efficiency of the MFHT method. To minimize the truncation error and reduce the computational time, the number of expansion terms has to be carefully chosen. Next, a brief overview of the planar multilayered Green's functions will be provided. Then, a detailed presentation of the MFHT will be described where the criteria of selecting the deformed integration path and other crucial parameters are explicitly explained. Finally, the accuracy and efficiency of the proposed method will be demonstrated by numerical examples and the conclusion will be provided.

2.2 Dyadic Green's Function for the Multilayered Isotropic Medium

When the currents are unknown variables, which usually happens in the scattering and antenna problems, DGF's may be employed to formulate integral equations for true or equivalent currents, which can be solved numerically by the MoM [19]. The hyper-

singular behavior of some integral equation kernels brings difficulties to the solution procedure [20], which can be avoided if the fields are expressed in terms of vector and scalar potentials with weakly singular kernels. This resulted in the development of MPIE for arbitrarily shaped scatterers. In the multilayered medium, an important advantage of the MPIE's is that the spectral-domain Green's functions as the kernels of SI's converge more rapidly and are easier to accelerate than those associated with the EFIE. To tackle arbitrarily shaped conducting objects, Michalski [91] proposed to use the scalar potential kernel, which necessitated a proper correction term of those elements of the vector potential kernel associated with the vertical current. This approach was later improved by Michalski and Zheng [20], who described three distinct MPIE formulations (referred to as A, B, and C) for a multilayered medium and discussed their relative merits and limitations. The C form of these MPIE's, which was deemed preferable for objects penetrating an interface, was implemented and validated for the case of a two-layer medium [92]. A detailed explanation of the integral equations is described as below.

2.2.1 Mixed Potential Integral Equation

Consider the isotropic media consisting of N homogeneous dielectric layers separated by $N-1$ planar interfaces parallel to the x and y planes of Cartesian coordinate system and located at $z = z_j$, $j = 1, \ldots, N$, as shown in Fig. 2.1. The layers are assumed to be laterally infinite. The medium of the layer j is characterized by constant electromagnetic parameters ϵ_j and μ_0. The layers may be lossy and the uppermost and lowermost layers may be perfect electric conducting (PEC) planes or free space. Electromagnetic fields in

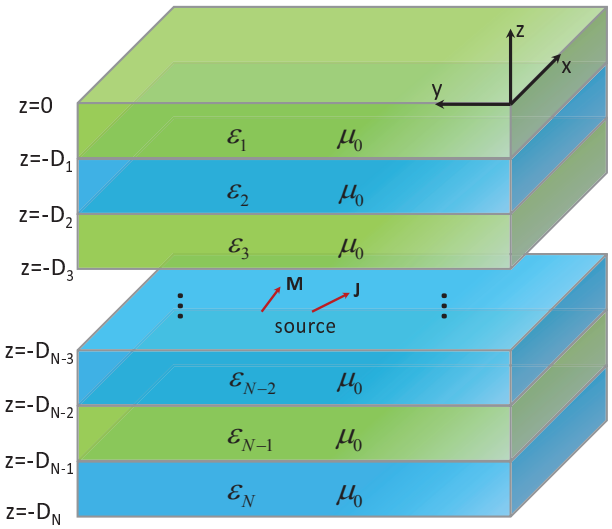

Figure 2.1: General multilayered geometry with arbitrary electric and magnetic currents.

the structure are excited by the arbitrary electric current density $\mathbf{J}$ and magnetic current density $\mathbf{M}$. The vectors $\mathbf{r}$ and $\mathbf{r}'$ identify the vector locations of the observation point and the source point, respectively. The electromagnetic fields due to arbitrary current densities may be expressed as

$$\mathbf{E}(\mathbf{r}) = \frac{1}{j\omega\varepsilon}(\nabla\nabla\cdot + k^2)\langle \overline{\mathbf{G}}^{EJ}; \mathbf{J}\rangle - \nabla\times\langle \overline{\mathbf{G}}^{EM}; \mathbf{M}\rangle \tag{2.1}$$

$$\mathbf{H}(\mathbf{r}) = \frac{1}{j\omega\mu}(\nabla\nabla\cdot + k^2)\langle \overline{\mathbf{G}}^{HM}; \mathbf{M}\rangle + \nabla\times\langle \overline{\mathbf{G}}^{HJ}; \mathbf{J}\rangle \tag{2.2}$$

Here, the notation $\langle , \rangle$ is used for integrals of products of two functions separated by the comma over their common spatial domain, with a dot over the comma indicating a dot product. Operators $\overline{\mathbf{G}}^{EJ/EM}$ and $\overline{\mathbf{G}}^{HJ/HM}$ are the electric and magnetic type dyadic Green's functions due to the electric and magnetic sources, respectively. Once the Green's functions for a multilayered medium are available, we can use (2.1) and (2.2) to compute the electromagnetic fields.

All of the Green's functions in (2.1) and (2.2) are not uniquely defined in a multilayered medium. Employing different forms of boundary conditions at the interfaces, the Green's functions may take traditional or alternative form [84, 125]. Here, we choose the traditional form of Green's function [91].

$$\overline{\mathbf{G}} = (\widehat{xx} + \widehat{yy})G_{xx} + \widehat{zx}G_{zx} + \widehat{zy}G_{zy} + \widehat{zz}G_{zz} \tag{2.3}$$

Although the DGF's in the form (2.1) and (2.2) can be employed for the calculation of electric and magnetic fields, the presence of the mixed tangential derivatives $\nabla\nabla\cdot$ in the calculation process makes the formula hyper-singular and less suitable for objects of arbitrary shape. Michalski and Mosig introduced a scalar potential function and a vector function into the Green's function to handle this problem. By changing the order of integration and differentiation and by applying the Gauss divergence theorem, the scalar potential function $G^{VJ/VM}$ can be expressed as

$$\nabla \cdot \langle \overline{\mathbf{G}}^{J/M}; \mathbf{J}/\mathbf{M} \rangle = -\langle \nabla' G^{VJ/VM}; \mathbf{J}/\mathbf{M} \rangle = \langle G^{VJ/VM}, \nabla' \cdot \mathbf{J}/\mathbf{M} \rangle \tag{2.4}$$

In a multilayered medium, the scalar potential function $G^{VJ/VM}$ does not exist generally. This is due to the fact that the scalar potential Green's functions of the horizontal and vertical dipoles in a multilayered medium are generally different. A usual remedy to this problem is to introduce a vector potential function (correction factor) $\mathbf{C}^{J/M}$ according to

$$\nabla \cdot \overline{\mathbf{G}}^{J/M} = -\nabla' G^{VJ/VM} + \mathbf{C}^{J/M} \tag{2.5}$$

The choice of the scalar potential and the correction factor is not unique, giving rise to to many possible formulations. Among these Green's functions, three useful choices referred as Formulations A, B and C are given in [20]. In the general case, Formulation C has a clear advantage over Formulations A and B, because it does not have undesirable contour integrals and its scalar potential kernel is continuous at the interfaces with respect to z. The detailed discussion in [20] shows that it is preferable to choose Michalski-Zheng's C-formulation which defines the correction factor as

$$\mathbf{C}^{J/M} = C^{J/M}\widehat{z} \tag{2.6}$$

Equations (2.1)-(2.2) can be converted into the following mixed potential forms by incorporating the correction factor into the vector potential Green's function:

$$\begin{aligned}\mathbf{E}(\mathbf{r}) = &- j\omega\mu \iint_s \overline{\mathbf{G}}^{AJ}(\mathbf{r},\mathbf{r}')\cdot\mathbf{J}(\mathbf{r}')dS' \\ &+ \frac{1}{j\omega\epsilon}\nabla \iint_s G^{VJ}(\mathbf{r},\mathbf{r}')\nabla'\cdot\mathbf{J}(\mathbf{r}')dS' \\ &- \iint_s \overline{\mathbf{G}}^{EM}(\mathbf{r},\mathbf{r}')\cdot\mathbf{M}(\mathbf{r}')dS'\end{aligned} \tag{2.7}$$

$$\begin{aligned}\mathbf{H}(\mathbf{r}) = &- j\omega\epsilon \iint_s \overline{\mathbf{G}}^{AM}(\mathbf{r},\mathbf{r}')\cdot\mathbf{M}(\mathbf{r}')dS' \\ &+ \frac{1}{j\omega\mu} \bigtriangledown \iint_s G^{VM}(\mathbf{r},\mathbf{r}') \bigtriangledown' \cdot\mathbf{M}(\mathbf{r'})dS' \\ &+ \iint_s \overline{\mathbf{G}}^{HJ}(\mathbf{r},\mathbf{r}')\cdot\mathbf{J}(\mathbf{r}')dS'\end{aligned} \tag{2.8}$$

$\overline{\mathbf{G}}^{AJ/AM}$ represents the dyadic Green's functions for magnetic vector potentials due to an electric/magnetic source, $G^{VJ/VM}$ represents the Green's functions for electric/magnetic

scalar potentials, and $\overline{\mathbf{G}}^{HJ/EM}$ represents the dyadic Green's functions for coupled magnetic/electric field due to an electric/magnetic source.

2.2.2 Formulation of Dyadic Green's Function

In a multilayered medium, the DGF's can usually be derived in the closed form only in the spectral domain. Here we adopt the dipole source method [30, 126, 127] to construct the Green's functions in the spectral domain. Due to an electric source, the scalar potential function and the correction factor in the spectral-domain Green's functions can be expressed as

$$\widetilde{G}^{VJ} = \frac{1}{\varepsilon_m}(F_n^{TE} + \frac{\partial}{\partial z'}V_n^{TM}) \tag{2.9}$$

$$\widetilde{C}^{AJ} = \frac{\mu_m}{\mu_n}V_n^{TM} \tag{2.10}$$

Here, F_n^{TE} and V_n^{TM} are potential functions. They can be obtained via iterative technique. After the proper mathematical simplification, the spectral-domain Green's functions can be concisely expressed as

$$\widetilde{\overline{\mathbf{G}}}^{AJ} = \begin{bmatrix} \mu_m F_n^{TE} & 0 & -jk_x\mu_m V_n^{TM} \\ 0 & \mu_m F_n^{TE} & -jk_y\mu_m V_n^{TM} \\ jk_x\mu_n V_n^{TE} & jk_y\mu_n V_n^{TE} & \mu_m\frac{\varepsilon_m}{\varepsilon_n}F_n^{TM} - \mu_n\frac{\partial}{\partial z'}V_n^{TE} \end{bmatrix} \tag{2.11}$$

$$\widetilde{\widetilde{\mathbf{G}}}^{AM} = \begin{bmatrix} \varepsilon_m F_n^{TM} & 0 & -jk_x\varepsilon_m V_n^{TE} \\ 0 & \varepsilon_m F_n^{TM} & -jk_y\varepsilon_m V_n^{TE} \\ jk_x\varepsilon_n V_n^{TM} & jk_y\varepsilon_n V_n^{TM} & \varepsilon_m\frac{\mu_m}{\mu_n}F_n^{TE} - \varepsilon_n\frac{\partial}{\partial z'}V_n^{TM} \end{bmatrix} \tag{2.12}$$

$$\widetilde{\widetilde{\mathbf{G}}}^{HJ} = \begin{bmatrix} -k_xk_yV_n^{TE} & -\frac{\mu_m}{\mu_n}\frac{\partial}{\partial z}F_n^{TE} - k_y^2V_n^{TE} & jk_yF_n^{TM} \\ \frac{\mu_m}{\mu_n}\frac{\partial}{\partial z}F_n^{TE} + k_x^2V_n^{TE} & k_xk_yV_n^{TE} & jk_xF_n^{TM} \\ -\frac{\mu_m}{\mu_n}jk_yF_n^{TE} & \frac{\mu_m}{\mu_n}jk_xF_n^{TE} & 0 \end{bmatrix} \tag{2.13}$$

$$\widetilde{\widetilde{\mathbf{G}}}^{EM} = \begin{bmatrix} k_xk_yV_n^{TM} & \frac{\varepsilon_m}{\varepsilon_n}\frac{\partial}{\partial z}F_n^{TM} + k_y^2V_n^{TM} & -jk_yF_n^{TE} \\ -\frac{\varepsilon_m}{\varepsilon_n}\frac{\partial}{\partial z}F_n^{TM} - k_x^2V_n^{TM} & -k_xk_yV_n^{TM} & -jk_xF_n^{TE} \\ \frac{\varepsilon_m}{\varepsilon_n}jk_yF_n^{TM} & -\frac{\varepsilon_m}{\varepsilon_n}jk_xF_n^{TM} & 0 \end{bmatrix} \tag{2.14}$$

$$\widetilde{G}^{VJ} = \frac{1}{\varepsilon_m}(F_n^{TE} + \frac{\partial}{\partial z'}V_n^{TM}) \tag{2.15}$$

$$\widetilde{G}^{VM} = \frac{1}{\mu_m}(F_n^{TM} + \frac{\partial}{\partial z'}V_n^{TE}) \tag{2.16}$$

$$V_n^{TE/TM} = -\frac{1}{k_\rho^2}[c\cdot\partial z(F_n^{TE/TM} - b) + \partial z'(F^{TM/TE} - b)] \tag{2.17}$$

where

$$c = \begin{cases} \mu_m/\mu_n & for\ V_n^{TE} \\ \epsilon_m/\epsilon_n & for\ V_n^{TM} \end{cases}$$

$$b = \begin{cases} e^{-jk_{mz}|z-z'|}/2jk_{mz} & m = n \\ 0 & m \neq n \end{cases}$$

The terms F_n^{TE} and F_n^{TM} can be described by an unbounded wave plus the scattered wave in the layer n due to the corresponding dipole source in the layer m [30]. The expressions are given in detail:

when $m = n$

$$F_m^{TE/TM} = \frac{1}{2jk_{mz}} \left(e^{-jk_{mz}|z-z'|} + B_m^{TE/TM} e^{jk_{mz}z} + D_m^{TE/TM} e^{-jk_{mz}z} \right) \tag{2.18}$$

when $m > n$

$$\begin{aligned} F_n^{TE/TM} = & \frac{1}{2jk_{mz}} \left(T_{mn}^{TE/TM,+} \left[e^{jk_{mz}(D_{m-1}+z')} + \widetilde{R}_{m,m+1}^{TE/TM} e^{-jk_{mz}(2D_m - D_{m-1}+z')} \right] \right. \\ & \left. \cdot \left[e^{-jk_{nz}(D_n+z)} + \widetilde{R}_{n,n-1}^{TE/TM} e^{-jk_{nz}(D_n - 2D_{n-1}-z)} \right] \widetilde{M}_m^{TE/TM} \right) \end{aligned} \tag{2.19}$$

when $m < n$

$$\begin{aligned} F_n^{TE/TM} = & \frac{1}{2jk_{mz}} \left(T_{mn}^{TE/TM,-} \left[e^{-jk_{mz}(D_m+z')} + \widetilde{R}_{m,m-1}^{TE/TM} e^{-jk_{mz}(D_m - 2D_{m-1}-z')} \right] \right. \\ & \left. \cdot \left[e^{-jk_{nz}(-D_{n-1}-z)} + \widetilde{R}_{n,n+1}^{TE/TM} e^{-jk_{nz}(2D_n - D_{n-1}+z)} \right] \widetilde{M}_m^{TE/TM} \right) \end{aligned} \tag{2.20}$$

where

$$B_m^{TE/TM} = \widetilde{R}_{m,m-1}^{TE/TM} \, \widetilde{M}_m^{TE/TM} \left(e^{jk_{mz}(2D_{m-1}+z')} + R_{m,m+1}^{TE/TM} e^{-jk_{mz}(2D_m - 2D_{m-1}+z')} \right) \tag{2.21}$$

$$D_m^{TE/TM} = \widetilde{R}_{m,m+1}^{TE/TM} \, \widetilde{M}_m^{TE/TM} \left(e^{-jk_{mz}(2D_m+z')} + R_{m,m-1}^{TE/TM} e^{-jk_{mz}(2D_m - 2D_{m-1}-z')} \right) \tag{2.22}$$

$$\widetilde{M}_m^{TE/TM} = \left[1 - \widetilde{R}_{m,m+1}^{TE/TM}\, \widetilde{R}_{m,m-1}^{TE/TM}\, e^{-2jk_{mz}(D_m - D_{m-1})}\right]^{-1} \tag{2.23}$$

and μ_m, μ_n, ϵ_m and ϵ_n are the relative permeabilities and permittivities in source and field layers, respectively.

The notation $\widetilde{R}^{TE/TM}$ represents the generalized reflection coefficients for TE- and TM-wave components and they can be obtained through the iterative method:

$$\widetilde{R}_{m,m+1}^{TE/TM} = \frac{R_{m,m+1}^{TE/TM} + \widetilde{R}_{m+1,m+2}^{TE/TM}\, e^{-2jk_{(m+1)z}(D_{m+1} - D_m)}}{1 + R_{m,m+1}^{TE/TM}\, \widetilde{R}_{m+1,m+2}^{TE/TM}\, e^{-2jk_{(m+1)z}(D_{m+1} - D_m)}} \tag{2.24}$$

$$\widetilde{R}_{m,m-1}^{TE/TM} = \frac{R_{m,m-1}^{TE/TM} + \widetilde{R}_{m-1,m-2}^{TE/TM}\, e^{-2jk_{(m-1)z}(D_{m-1} - D_{m-2})}}{1 + R_{m,m-1}^{TE/TM}\, \widetilde{R}_{m-1,m-2}^{TE/TM}\, e^{-2jk_{(m-1)z}(D_{m-1} - D_{m-2})}} \tag{2.25}$$

Assuming that there are N layers in Fig. 2.1 (the uppermost and lowermost layers are free space and a PEC plane respectively), we have the following boundary conditions:

$$\widetilde{R}_{N,N+1}^{TE} = -1 \tag{2.26}$$

$$\widetilde{R}_{N,N+1}^{TM} = 1 \tag{2.27}$$

$$\widetilde{R}_{1,0}^{TE/TM} = R_{1,0}^{TE/TM} \tag{2.28}$$

The notation $R^{TE/TM}$ denotes the Fresnel reflection coefficients which can be expressed by

$$R_{m,m+1}^{TE} = \frac{\mu_{m+1}\, k_{mz} - \mu_m\, k_{(m+1)z}}{\mu_{m+1}\, k_{mz} + \mu_m\, k_{(m+1)z}} \tag{2.29}$$

$$R^{TM}_{m,m+1} = \frac{\epsilon_{m+1}\, k_{mz} - \epsilon_m\, k_{(m+1)z}}{\epsilon_{m+1}\, k_{mz} + \epsilon_m\, k_{(m+1)z}} \tag{2.30}$$

$$R^{TE}_{m,m-1} = \frac{\mu_{m-1}\, k_{mz} - \mu_m\, k_{(m-1)z}}{\mu_{m-1}\, k_{mz} + \mu_m\, k_{(m-1)z}} \tag{2.31}$$

$$R^{TM}_{m,m-1} = \frac{\epsilon_{m-1}\, k_{mz} - \epsilon_m\, k_{(m-1)z}}{\epsilon_{m-1}\, k_{mz} + \epsilon_m\, k_{(m-1)z}} \tag{2.32}$$

$$k^2_{iz} = \epsilon_{ri} k^2_0 - k^2_\rho \tag{2.33}$$

The notation $T^{TE/TM,+}_{mn}$ represents the generalized transmission coefficient from the source region m to the field region n for TE- and TM-wave, which can be calculated iteratively according to the following expression

$$T^{TE/TM,+}_{mn} = \prod_{i=n+1}^{m} e^{-jk_{iz}(D_i - D_{i-1})} S^{+}_{i,i-1} \tag{2.34}$$

where $D_1 = D_0$ is assumed, and

$$S^{+}_{i,i-1} = \frac{1 + R_{i,i-1}}{1 - R_{i-1,i} \cdot \widetilde{R}_{i-1,i-2} \cdot e^{-2jk_{(i-1)z}(D_{i-1} - D_{i-2})}} \tag{2.35}$$

$T^{TE/TM,-}_{mn}$ can be expressed as

$$T^{TE/TM,-}_{mn} = \prod_{i=m}^{n-1} e^{-jk_{iz}(D_i - D_{i-1})} S^{-}_{i,i+1} \tag{2.36}$$

where $D_1 = D_0$ and

$$S^{-}_{i,i+1} = \frac{1 + R_{i,i+1}}{1 - R_{i+1,i} \cdot \widetilde{R}_{i+1,i+2} \cdot e^{-2jk_{(i+1)z}(D_{i+1} - D_i)}} \tag{2.37}$$

Generally, the planar multilayered Green's functions of vector and scalar potentials in the spatial domain are expressed in terms of SI's of their corresponding spectral-domain counterpart:

$$\overline{\mathbf{G}} = \frac{1}{2\pi}\int_0^\infty \widetilde{\overline{\mathbf{G}}}(k_\rho) J_n(k_\rho \rho) k_\rho^{n+1} dk_\rho \tag{2.38}$$

where $\widetilde{\overline{\mathbf{G}}}$ is the spectral domain counterpart of $\overline{\mathbf{G}}$, J_n is the first kind Bessel function of order n, $k_\rho = \sqrt{k_x^2 + k_y^2}$, and $\rho = \sqrt{(x-x')^2 + (y-y')^2}$.

2.3 Fast Hankel Transform Algorithm

An efficient method of evaluating Hankel transforms is to use digital filter technique, first proposed by Ghosh [103, 104] and later improved by Anderson [128], Christensen [110] and many others [129, 130]. Compared with numerical integration, the employment of FHT filter technique is beneficial to the substantial reduction in computational time. One important procedure of application of FHT technique is the calculation of filter coefficients, which are usually obtained by solving convolution equations transformed from the Hankel transform function. Filters calculated in this way depend on the choice of transform function, and the accuracy of these filters in their practical applications is mainly determined by the property of the input function. Currently, it is possible to find explicit series expansions for the filter coefficients [131], and more importantly, derive a majorant for the error in the application of the filters. Based on a required accuracy criterion, the sampling density and filter length can be minimized by selecting the suitable parameters determining the filter characteristics. These parameters are dependent on the analytical properties of the input function.

Here,we consider the Hankel integral

$$G(\rho) = \frac{1}{2\pi} \int_0^\infty \widetilde{G}(k_\rho) J_\nu(k_\rho \rho) k_\rho dk_\rho \tag{2.39}$$

by the substitutions

$$k_\rho = e^{-u} \tag{2.40}$$

$$\rho = e^{\upsilon} \tag{2.41}$$

and the definitions

$$\widetilde{G}'(u) = \frac{1}{2\pi} e^{-u} \widetilde{G}(e^{-u}) \tag{2.42}$$

$$G'(\upsilon) = e^{\upsilon} G(e^{\upsilon}) \tag{2.43}$$

$$H(u) = e^{u} J_\nu(e^{u}) \tag{2.44}$$

Then, (2.39) may be rewritten as a convolution integral:

$$G'(\upsilon) = \int_{-\infty}^{\infty} \widetilde{G}'(u)\, H_\nu(\upsilon - u)\, du = \widetilde{G}' * H_\nu \tag{2.45}$$

Using the convolution theorem, we can get

$$\widehat{G}'(s) = \widehat{\widetilde{G}}'(s) \cdot \widehat{H}_\nu(s) \tag{2.46}$$

where

$$\widehat{H}_\nu(s) = \int_{-\infty}^{\infty} H_\nu(\upsilon) e^{-j2\pi\upsilon s} d\upsilon \tag{2.47}$$

and analogously for $\widehat{\widetilde{G}}'$ and $\widehat{G}'$.

The term $\widehat{H}_\nu(s)$ may be evaluated explicitly by:

$$\widehat{H}_\nu(s) = 2^{-j2\pi s} \frac{\Gamma(\frac{\nu+1}{2} - j\pi s)}{\Gamma(\frac{\nu+1}{2} + j\pi s)} \tag{2.48}$$

and has the property $|\widehat{H}_\nu(s)| \equiv 1$.

The numerical problem of calculating $G'(\upsilon)$ is formulated by substituting the function $\widetilde{G}'^*$ defined by

$$\widetilde{G}'^*(u) = \sum_{n=-\infty}^{\infty} \widetilde{G}'(n\triangle) \cdot P(\frac{u}{\triangle} - n) \tag{2.49}$$

which is the sampled and interpolated version of $\widetilde{G}'$. The sampling interval $\triangle$ is usually expressed in terms of N_{DEC}, the number of sampling points per decade.

$$\triangle = \frac{\ln(10)}{N_{DEC}} \tag{2.50}$$

Substituting (2.49) into (2.45), we can obtain the approximation of G'^*.

$$G'^*(\upsilon) = \int_{-\infty}^{\infty} \widetilde{G}'^*(u) \cdot H_\nu(\upsilon - u) du = \sum_{n=-\infty}^{\infty} \widetilde{G}'(n\triangle) \cdot H_\nu^*(\upsilon - n\triangle) \tag{2.51}$$

with

$$\widetilde{G}'^*(\upsilon) = \int_{-\infty}^{\infty} P(\frac{u}{\triangle}) \cdot H_\nu(\upsilon - u) du = P(\frac{u}{\triangle}) * H_\nu(u) \tag{2.52}$$

Considering values of $\upsilon = m\triangle (m \in R)$, we have

$$G'^{*}(m\triangle) = \sum_{n=-\infty}^{\infty} \widetilde{G}'(n\triangle) \cdot H_{\nu}^{*}[(m-n)\triangle] \tag{2.53}$$

The term G'^{*} is thus obtained at discrete points as a discrete convolution between sampled values of $\widetilde{G}'$ and the filter coefficients $H_{\nu}^{*}(k\triangle)$. We may then construct an approximation $G'^{**}(\upsilon)$ to $G'(\upsilon)$ by the usual interpolation scheme

$$G'^{**}(\upsilon) = \sum_{m=-\infty}^{\infty} G'^{*}(m\triangle) \cdot P'(\frac{\upsilon}{\triangle} - m) \tag{2.54}$$

$$P(u) = a\frac{\sin(\pi u)}{\sinh(\pi a u)} \tag{2.55}$$

$$\widehat{P}(s) = \frac{1}{2}\tanh\left[\frac{\pi}{a}(s+\frac{1}{2})\right] - \frac{1}{2}\tanh\left[\frac{\pi}{a}(s-\frac{1}{2})\right] \tag{2.56}$$

The terms P and P' are interpolating functions in (2.49) and (2.54) and a is the smoothness parameter. The filter coefficients $H_{\nu}^{*}(\upsilon)$, which have explicit series representations, are calculated by using the convolution theorem and the filter function transform pair.

It is worth noting that this Hankel transform filter algorithm has two attractive advantages. Firstly, for a given accuracy requirement, the filter with adequate length and sampling density $(1/\triangle)$ can always be achieved by choosing a suitable a value according to the analytical properties of the input function $\widetilde{G}'(u)$. Secondly, the filter coefficients can be calculated for an arbitrary order of Hankel transform.

When applied to the computation of DGF's, the FHT filter technique transforms the

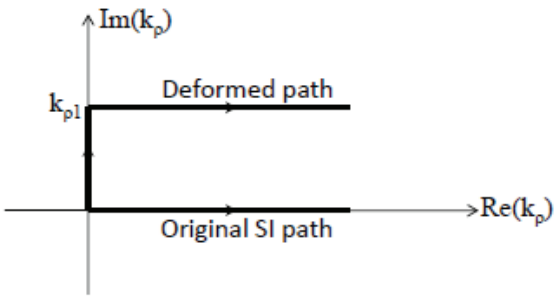

Figure 2.2: The deformed Sommerfeld integration path.

SI with a smooth spectral-domain Green's function into a linear discrete convolution in the spatial domain. As briefly outlined above, because of the branch-point singularity, the traditional FHT method was only applicable to shielded multilayered geometries so far. Next, we will propose a newly developed method to overcome this shortcoming and apply the new method to general multilayered problems.

2.4 Modified Fast Hankel Transform Algorithm

In this section, a MFHT filter algorithm is proposed to calculate the spatial-domain Green's functions for general multilayered geometries. In order to move away from surface wave poles and branch points to obtain a smooth spectrum of Green's function, the Sommerfeld integration path (SIP) is deformed from the real axis to the first quadrant, as shown in Fig. 2.2. Then the SI can be written as:

$$\begin{aligned} G(r,r') =& \frac{1}{2\pi}\int_0^{jk_{\rho 1}} \widetilde{G}(k_\rho;z,z')J_n(k_\rho\rho)k_\rho^{n+1}dk_\rho \\ &+\frac{1}{2\pi}\int_{jk_{\rho 1}}^{\infty+jk_{\rho 1}} \widetilde{G}(k_\rho;z,z')J_n(k_\rho\rho)k_\rho^{n+1}dk_\rho \end{aligned} \tag{2.57}$$

where $k_{\rho 1}$ is a real number. The first integral can be efficiently calculated by adaptive Simpson quadrature method with a computational time quite small compared with the total computational time. The second integral is evaluated by the MFHT method.

2.4.1 Formulation of MFHT

The second integral in (2.57) can be written as:

$$\begin{aligned} G_2(\rho) &= \frac{1}{2\pi}\int_{jk_{\rho 1}}^{\infty+jk_{\rho 1}} \widetilde{G}(k_\rho; z, z')J_n(k_\rho\rho)k_\rho^{n+1}dk_\rho \\ &= \frac{1}{2\pi}\int_0^{\infty} \widetilde{G}'(k'_\rho; z, z')J_n(k'_\rho\rho + jk_{\rho 1}\rho)dk'_\rho \end{aligned} \tag{2.58}$$

with

$$k'_\rho = k_\rho - jk_{\rho 1} \tag{2.59}$$

$$\widetilde{G}'(k'_\rho; z, z') = \widetilde{G}(k_\rho; z, z') \cdot k_\rho^{n+1} \tag{2.60}$$

where $\rho > 0$ and the input function $\widetilde{G}'$ is a complex function of the real argument k'_ρ. Although the input function of this integral becomes a smooth function along the deformed integration path, the argument of the Bessel function becomes complex. Since the FHT filters developed thus far only permit the argument of Bessel function in the Hankel integral to be real, the traditional FHT method is not directly applicable here.

In order to use the FHT method, a Bessel function with a complex argument can be expressed as [132]:

$$J_n(u \pm v) = \sum_{k=-\infty}^{\infty} J_{n\mp k}(u)J_k(v) \tag{2.61}$$

The two arguments, u and v, can be arbitrary values and the Bessel functions with com-

plex arguments in (2.58) are expanded by the sum:

$$J_n(k'_\rho\rho + jk_{\rho 1}\rho) = \sum_{k=-\infty}^{\infty} J_{n-k}(jk_{\rho 1}\rho)J_k(k'_\rho\rho) \tag{2.62}$$

so that (2.58) can be written as:

$$\begin{aligned} G_2(\rho) &= \frac{1}{2\pi}\int_0^\infty \widetilde{G}'(k'_\rho; z, z')J_n(k'_\rho\rho + jk_{\rho 1}\rho)dk'_\rho \\ &= \frac{1}{2\pi}\sum_{k=-\infty}^{\infty} J_{n-k}(jk_{\rho 1}\rho)\int_0^\infty \widetilde{G}'(k'_\rho; z, z')J_k(k'_\rho\rho)dk'_\rho \end{aligned} \tag{2.63}$$

where

$$J_m(jk_{\rho 1}\rho) = e^{jm\pi/2}\cdot I_m(k_{\rho 1}\rho) = j^m \cdot I_m(k_{\rho 1}\rho) \tag{2.64}$$

The modified Bessel function I_m is a monotonic increasing function. Each expansion term in the equation (2.63) can be efficiently and accurately evaluated by the traditional FHT method. Here, we choose the optimized FHT filter method proposed by [110] to calculate the Hankel integrals since the FHT coefficients for the Hankel transform with an arbitrary order can be easily obtained.

In the optimized FHT filter technique, two functions are introduced related with the functions in (2.63).

$$h(k'_\rho) = \widetilde{G}'(k'_\rho; z, z') \tag{2.65}$$

$$H(\rho) = \rho \cdot G_2(\rho) \cdot 2\pi \cdot [J_k(jk_{\rho 1}\rho)]^{-1} \tag{2.66}$$

Then each expansion term in (2.63) can be re-written as:

$$H(\rho) \cdot \rho^{-1} = \int_0^{\infty} h(k'_\rho) \cdot J_{n-k}(k'_\rho \rho) dk'_\rho \tag{2.67}$$

Eq. (2.67) is transformed to a linear convolution-type integral by using the substitutions $x = \ln(\rho)$ and $y = \ln(1/k'_\rho)$:

$$H(e^x) \cdot e^{-x} = \int_{-\infty}^{\infty} h(e^{-y}) \cdot [e^{-y} \cdot J_{n-k}(e^{x-y})] dy \tag{2.68}$$

where h is the input function related with the spectral-domain Green's function, H is the output function related with the spatial-domain Green's function, and the product in the bracket is the filter-response function of the linear system. The continuous convolution in (2.68) is discretized to obtain the linear convolution in a general form:

$$H^*(j\Delta) = \sum_{i=-\infty}^{\infty} h(i\Delta) \cdot L^*[(j-i)\Delta] \tag{2.69}$$

where

$$\Delta = \frac{\ln(10)}{N_{DEC}} \tag{2.70}$$

$$L^*(x) = \int_{-\infty}^{\infty} P(\frac{y}{\Delta}) L(x-y) dy = P(\frac{y}{\Delta}) * L(y) \tag{2.71}$$

$$P(y) = a \frac{\sin(\pi y)}{\sinh(\pi a y)} = \text{sinsh}(y) \tag{2.72}$$

where $L^*[(j-i)\Delta]$ is the linear digital-filter response, Δ is the sampling interval, N_{DEC} is the number of samples per decade, H^* is the approximation of H, $P(y)$ is the interpolation function, and a is the smoothness parameter. The filter coefficients $L^*(j\Delta)$ may be calculated by using the convolution theorem. H^* is obtained at discrete points as a discrete convolution between the samples of h and $L^*(j\Delta)$. Based on the characteristics of the input function $h(k_\rho)$ and a scheduled truncation tolerance parameter, the sampling interval and the length of digital filter coefficients can be determined. In order to adequately capture the behavior of the input function near the singularities, N_{DEC} is chosen as 350 in this thesis.

2.4.2 Parameters of SIP and MFHT

The value of $k_{\rho 1}$ involved in the deformed integration path is the key to the accuracy and efficiency of the MFHT algorithm. To determine the value range of $k_{\rho 1}$, a well-known Sommerfeld identity is chosen as an example.

$$\frac{e^{-jk_0 r}}{r} = \int_0^\infty \frac{e^{-jk_z z}}{jk_z} J_0(k_\rho \rho) k_\rho dk_\rho \tag{2.73}$$

where

$$k_0 = \sqrt{{k_\rho}^2 + {k_z}^2} \tag{2.74}$$

$$r = \sqrt{\rho^2 + z^2} \tag{2.75}$$

It is noticed that the input function $\frac{e^{-jk_z z}}{jk_z} \cdot k_\rho$ has singularities at the points $k_\rho = \pm k_0$. Thus, the traditional FHT filter is not applicable for this case. Along the deformed inte-

gration path, the singularity is avoided and the input function becomes smooth. As for the choice of the parameters involved in the path, the required accuracy of the MFHT filter algorithm determines the minimum value of $k_{\rho 1}$. In order to achieve accurate numerical results, sampling of the input function has to adequately describe its magnitude behavior. Here, the operating frequency is set at 3 GHz and the vertical distance z is 1 mm. When the value of $k_{\rho 1}$ is respectively selected as $0.001k_0$, $0.005k_0$ and $0.01k_0$, the samples of the input function compared with the exact values are shown in Figs. 2.3-2.5. It is seen that when $k_{\rho 1}$ is selected as $0.001k_0$ or $0.005k_0$, the characteristic of the singularity in the input function is still obvious and the oscillating behavior of the input function cannot be adequately captured by the samples, even with a quite small sampling interval. Here, the sampling interval cannot be infinitesimal since it has a limited minimum value and the length of the FHT filter would greatly increase as the decreasing of the sampling interval. When $k_{\rho 1} = 0.01k_0$, the input function is quite smooth and the sampling is adequate to describe the behavior of the pulse. Corresponding to the three different values of $k_{\rho 1}$, the relative errors of estimated results compared with the exact analytical results are shown in Fig. 2.6. When the value of $k_{\rho 1}$ is from $0.001k_0$ to $0.01k_0$, the accuracy of estimated results can be greatly improved in the intermediate field and the relative error remains below -3 dB over a large range of the variable ρ when $k_{\rho 1} = 0.01k_0$. It is deduced that based on the MFHT filter algorithm, the estimated results of the SI can be relied upon when $k_{\rho 1} \geq 0.01k_0$.

On the other hand, the efficiency and accuracy determine the maximum value of $k_{\rho 1}$. As the product of $k_{\rho 1}$ and ρ becomes larger, the magnitude of input function would become smoother and thus the sampling density could decrease. However, since the

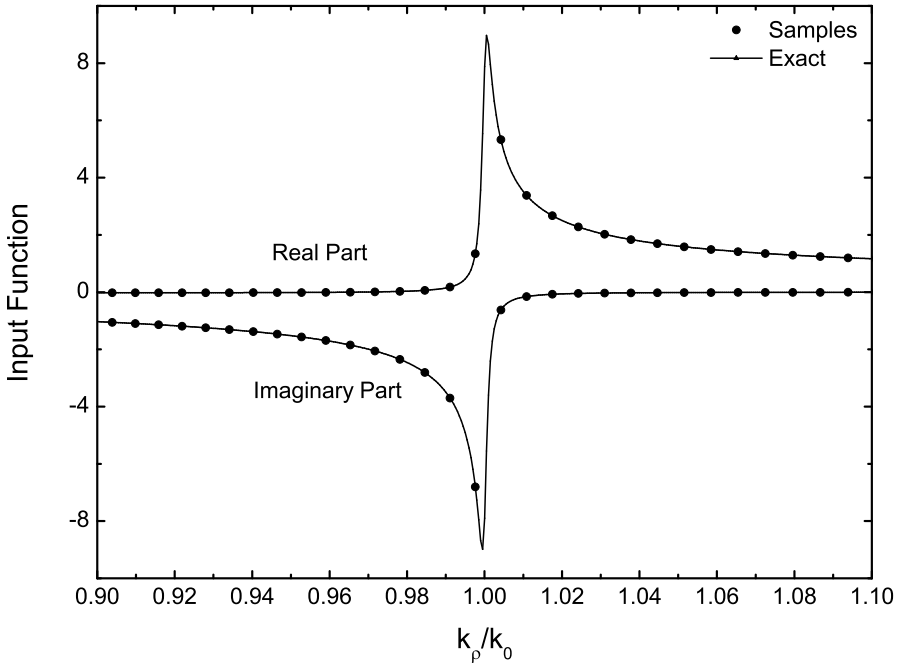

Figure 2.3: The comparison between the exact input function and the samples used for MFHT, when $k_{\rho 1} = 0.001k_0$.

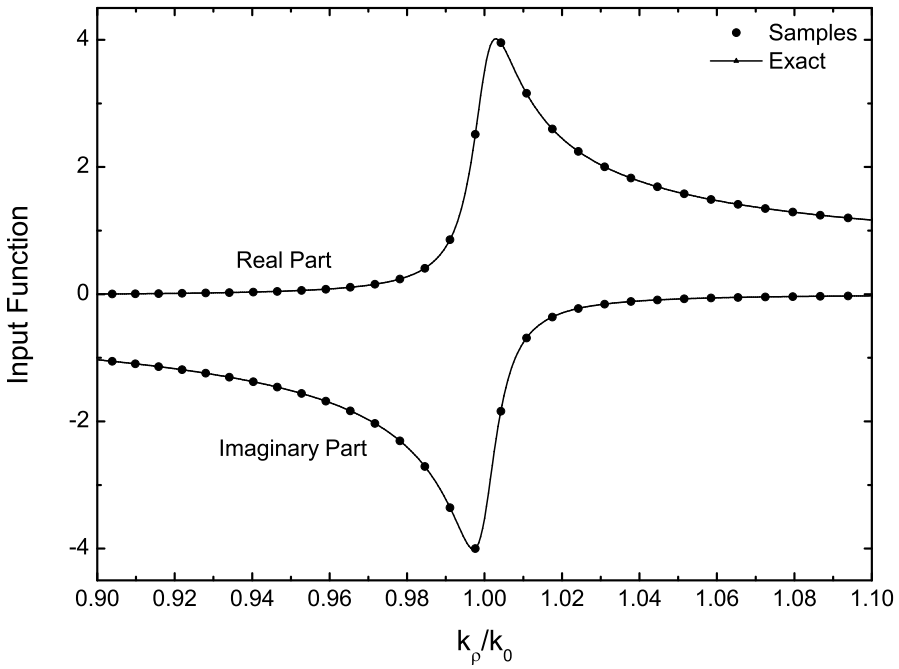

Figure 2.4: The comparison between the exact input function and the samples used for MFHT, when $k_{\rho 1} = 0.005k_0$.

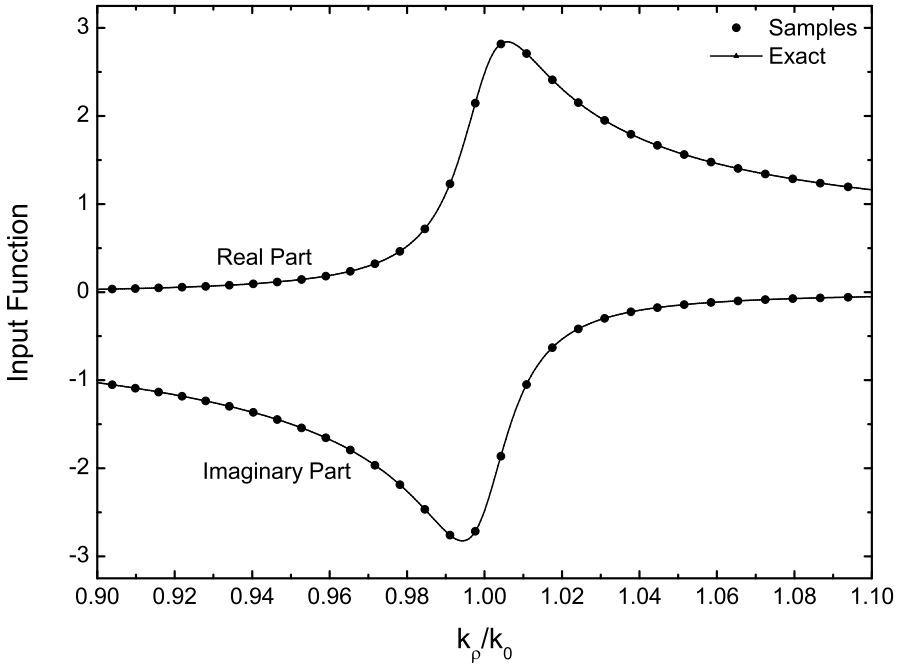

Figure 2.5: The comparison between the exact input function and the samples used for MFHT, when $k_{\rho 1} = 0.010k_0$.

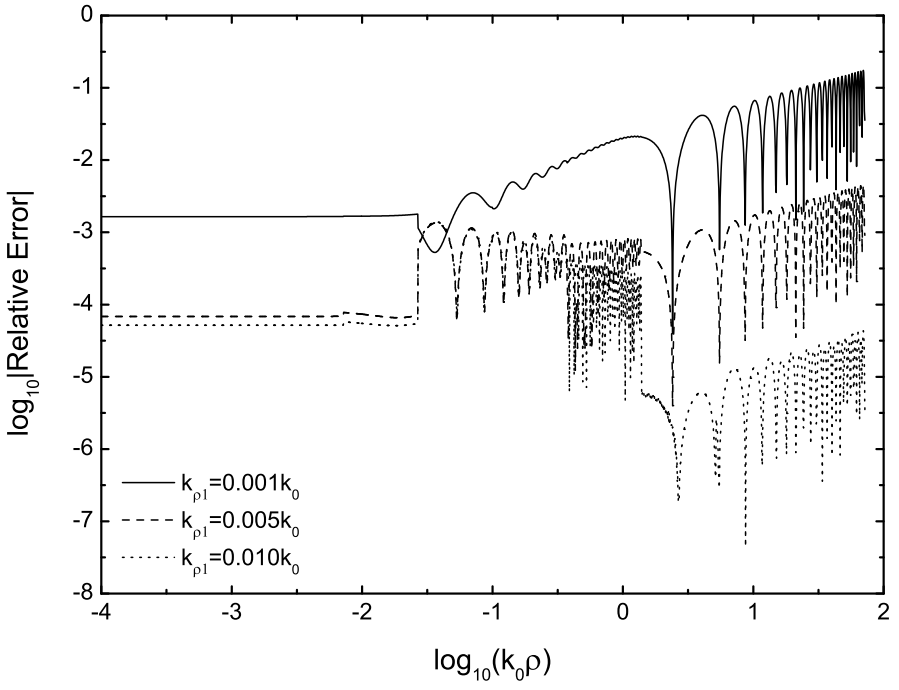

Figure 2.6: Relative errors of the results calculated by the MFHT filter for the Sommerfeld identity (2.73) when $k_{\rho 1}$=$0.001k_0$, $0.005k_0$ and $0.010k_0$, respectively.

function $J_{n-k}(jk_{\rho 1}\rho)$ in (2.63) is a monotonic increasing function of the argument, with a scheduled accuracy requirement, the number of expansion terms in (2.63) should be large enough to decrease the truncation error for the expansion of Bessel function. However, the increase of expansion terms reduces the efficiency of the MFHT filter algorithm and probably induces a relatively large numerical error. Therefore, the maximum value of the product of $k_{\rho 1}$ and ρ should be determined. Here, the maximum value of ρ is set to $10^{2.2}/k_0$. When the truncation error is chosen as 10^{-9}, the number of expansion terms needed in (2.63) is shown in Fig. 2.7, corresponding to the different values of $k_{\rho 1}$. In order to guarantee the efficiency of the MFHT filter algorithm, the number of expansion terms should be below the maximum value of 29 and the corresponding value of $k_{\rho 1}$ is $0.026k_0$. Figure 2.8 shows the relative errors of the evaluated results when the number of the expansion terms is chosen as 11, 17 and 27, respectively. The relative errors have a large difference until $\rho \geq 10^{1.5}/k_0$, since more expansion terms are required for a larger value of ρ.

In order to simultaneously guarantee the efficiency and accuracy of the MFHT filter algorithm, the value range of $k_{\rho 1}$ is suggested from $0.01k_0$ to $0.026k_0$ and the number of the expansion terms k is from 23 to 29, as shown in Fig. 2.7. In the examples of this thesis, the number of expansion terms is selected to be 27. The smoothness parameter a is set to be 8.3764×10^{-3}, which is determined by the sampling interval.

In the planar multilayered problems, the order of Bessel function in (2.63) usually has three values: zero, one and two. Corresponding to each value, (2.62) can be written

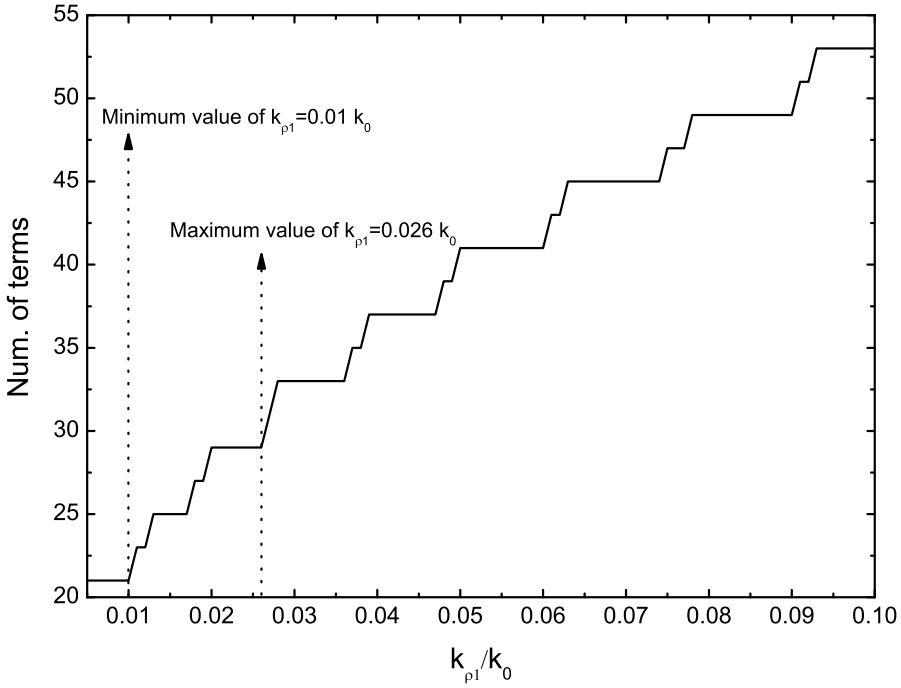

Figure 2.7: The number of expansion terms needed in (2.63) when the truncation error is set to 10^{-9} and $\log_{10}(k_0\rho_{max}) = 2.2$.

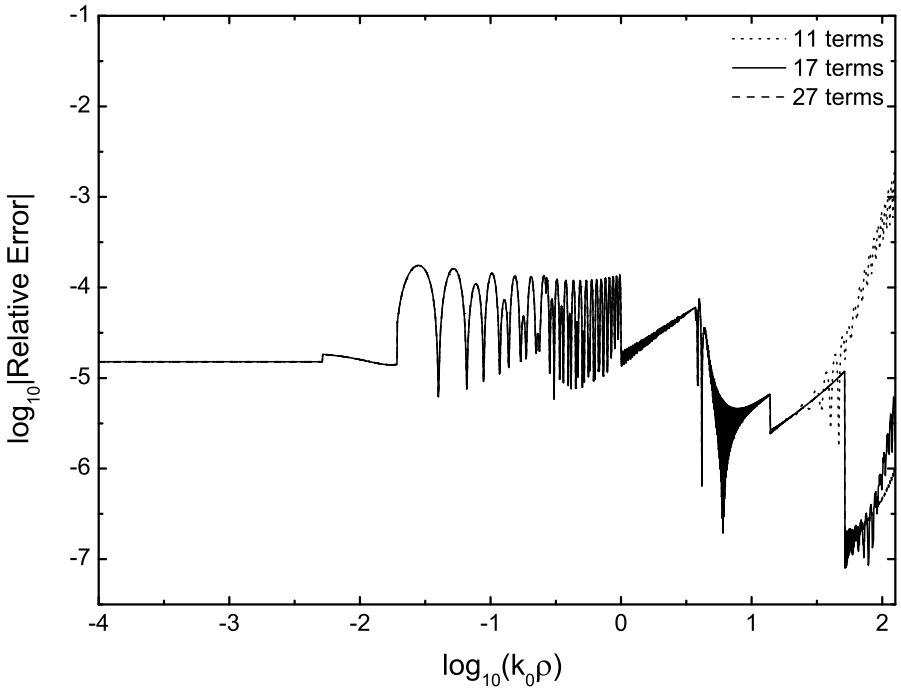

Figure 2.8: Relative errors of the results calculated by the MFHT filter when $f = 3$ GHz, $k_{\rho 1} = 0.02k_0$, the number of expansion terms k =11, 17 and 27, respectively.

as:

$$\begin{aligned} & J_0(jk_{\rho 1}\rho + k'_\rho\rho) \\ =& \sum_{k=-13}^{13} J_{-k}(jk_{\rho 1}\rho)J_k(k'_\rho\rho) \\ =& J_0(jk_{\rho 1}\rho)J_0(k'_\rho\rho) + 2\sum_{k=1}^{13}(-1)^k J_k(jk_{\rho 1}\rho)J_k(k'_\rho\rho) \end{aligned} \tag{2.76}$$

$$\begin{aligned} & J_1(jk_{\rho 1}\rho + k'_\rho\rho) \\ =& \sum_{k=-13}^{13} J_{1-k}(jk_{\rho 1}\rho)J_k(k'_\rho\rho) \\ =& \sum_{k=1}^{13}(-1)^{k-1}[J_k(jk_{\rho 1}\rho)J_{k-1}(k'_\rho\rho) + J_{k-1}(jk_{\rho 1}\rho)J_k(k'_\rho\rho)] \\ & - J_{14}(jk_{\rho 1}\rho)J_{13}(k'_\rho\rho) \end{aligned} \tag{2.77}$$

$$\begin{aligned} & J_2(jk_{\rho 1}\rho + k'_\rho\rho) \\ =& \sum_{k=-13}^{13} J_{2-k}(jk_{\rho 1}\rho)J_k(k'_\rho\rho) \\ =& \sum_{k=0}^{11}(-1)^k[J_{k+2}(jk_{\rho 1}\rho)J_k(k'_\rho\rho) + J_k(jk_{\rho 1}\rho)J_{k+2}(k'_\rho\rho)] \\ & - J_{15}(jk_{\rho 1}\rho)J_{13}(k'_\rho\rho) + J_{14}(jk_{\rho 1}\rho)J_{12}(k'_\rho\rho) \\ & + J_1(jk_{\rho 1}\rho)J_1(k'_\rho\rho) \end{aligned} \tag{2.78}$$

It is noticed that the actual terms needed for the FHT are 14, much less than 27 expansion terms. Generally, due to the inherent numerical error, the expansion accuracy has a maximum limitation as the increase of the expansion terms.

2.5 Numerical Results

This section is to investigate and discuss the accuracy and efficiency of the MFHT filter algorithm. Firstly, three widely used Sommerfeld identities (2.73)(2.79)(2.80) are used as the numerical examples. The input functions in the three identities $\frac{e^{-jk_z z}}{jk_z} \cdot {k_\rho}^n$ have the same singularities located at the points $k_\rho = \pm k_0$. Thus, the traditional FHT method cannot be directly used here. When the MFHT method is applied for the three integrals, the formulae (2.76)-(2.78) are used for the expansion of the Bessel function, respectively.

$$\frac{\rho(1 + jk_0 r)e^{-jk_0 r}}{r^3} = \int_0^\infty \frac{e^{-jk_z z}}{jk_z} J_1(k_\rho \rho){k_\rho}^2 dk_\rho \tag{2.79}$$

$$\frac{\rho^3(3 + 3jk_0 r - k_0^2 r^2)e^{-jk_0 r}}{r^5} = \int_0^\infty \frac{e^{-jk_z z}}{jk_z} J_2(k_\rho \rho){k_\rho}^3 dk_\rho \tag{2.80}$$

In order to validate the applicability of the value range of $k_{\rho 1}$, corresponding to the three SI's, the relative errors of the evaluated results compared with the exact analytical results are shown in Figs. 2.9-2.11. In the three figures, the value of $k_{\rho 1}$ is selected to be $0.01k_0$, $0.02k_0$ and $0.026k_0$, respectively. Figure 2.9 shows the relative errors for the first identity (2.73) when the operating frequency is 10 MHz. Figure 2.10 depicts the relative errors for the second identity (2.79) when the operating frequency is 1 GHz. When the operating frequency is 100 GHz, Fig. 2.11 shows the relative errors for the third identity (2.80). It can be seen that all the relative errors of the numerical results remain below -3 dB when the value range of $k_{\rho 1}$ is from $0.01k_0$ to $0.026k_0$. Corresponding to the three identities, the relative errors are also plotted at different frequencies to demonstrate the robustness of the MFHT method, as shown in Figs. 2.12-2.14. In the

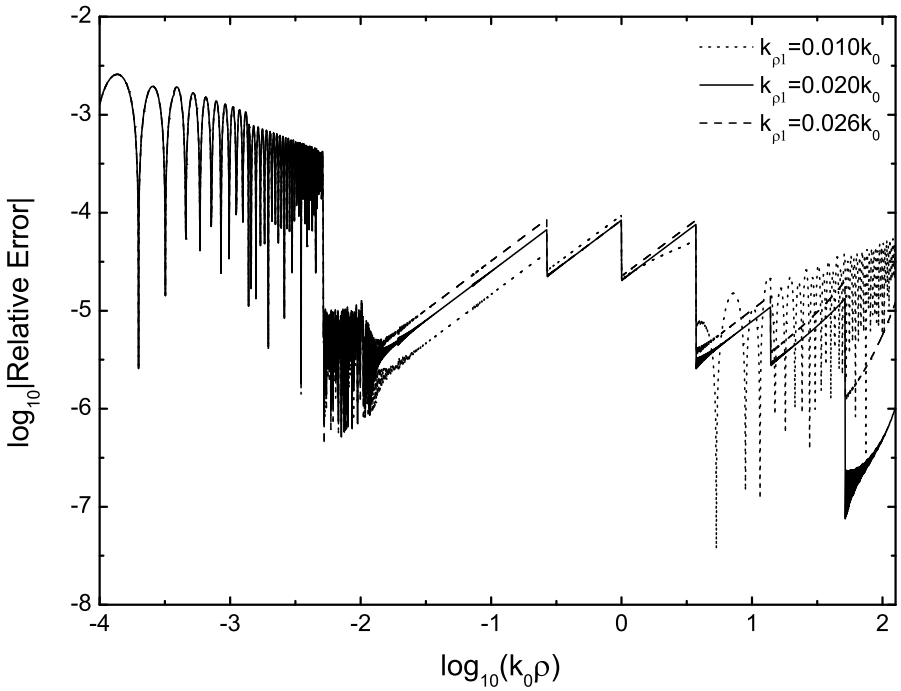

Figure 2.9: Relative errors of the results calculated by the MFHT filter for the Sommerfeld identity (2.73), when $z = 1$ mm, $f = 10$ MHz, and $k_{\rho 1} = 0.01k_0$, $0.02k_0$ and $0.026k_0$, respectively.

three figures, the following parameters are kept unchanged: $k_{\rho 1} = 0.02k_0$, f_{req}=10 MHz, 1 GHz and 100 GHz, respectively. Figures 2.12-2.14 show the relative errors for the identities (2.73), 2.79) and (2.80), respectively. It is illustrated that in the three figures, all the relative errors remain below -3 dB over wide bandwidth (4 orders) in frequency and wide range of ρ (6 orders) in magnitude. The results confirm that the proposed algorithm is strongly reliable without the extraction of the contribution of singularities. In addition, although the number of the expansion terms are 14, all numerical calculations are completed within 5 seconds on a 2.8 GHz personal computer with 1 GB RAM. Successive application of the MFHT filter algorithm to the three Sommerfeld identities validates its great performance on the accuracy and efficiency.

Secondly, the MFHT filter algorithm is applied for the calculation of the spatial-

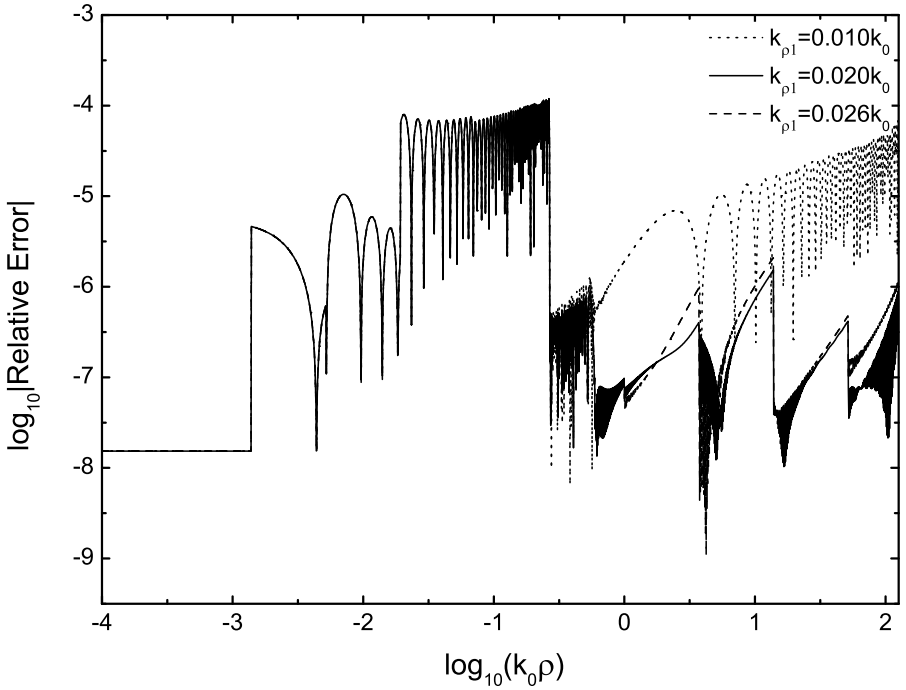

Figure 2.10: Relative errors of the results calculated by the MFHT filter for the Sommerfeld identity (2.79), when $z = 1$ mm, $f = 1$ GHz, and $k_{\rho 1} = 0.01k_0$, $0.02k_0$ and $0.026k_0$ respectively.

domain Green's function for the planar multilayered media. For notation purposes, m represents the layer number of the source point, n represents the layer number of the field point, z' represents the source position and z represents the field position. For the lossless medium shown in Fig. 2.15, when $z' = z = -1$ mm and $f = 30$ GHz, the SWP's are located at $1.736k_0$ and $2.436k_0$, and branch-point singularity is located at k_0. Figure 2.16 shows the samples of the spectral-domain Green's function and the exact values when $k_{\rho 1} = 0.015k_0$. Along the deformed SIP, the three singularities are avoided and the behavior of the spectral-domain Green's function $\widetilde{G}_{xz}^{AJ}$ is adequately captured by the sampling. Figure 2.17 and Figure 2.18 depict the MFHT-based results for G_{xz}^{AJ} and G_{zz}^{AJ}, respectively. There is an excellent agreement between the MFHT-based results and the numerical integration results, when the operating frequencies are 0.3 GHz, 3

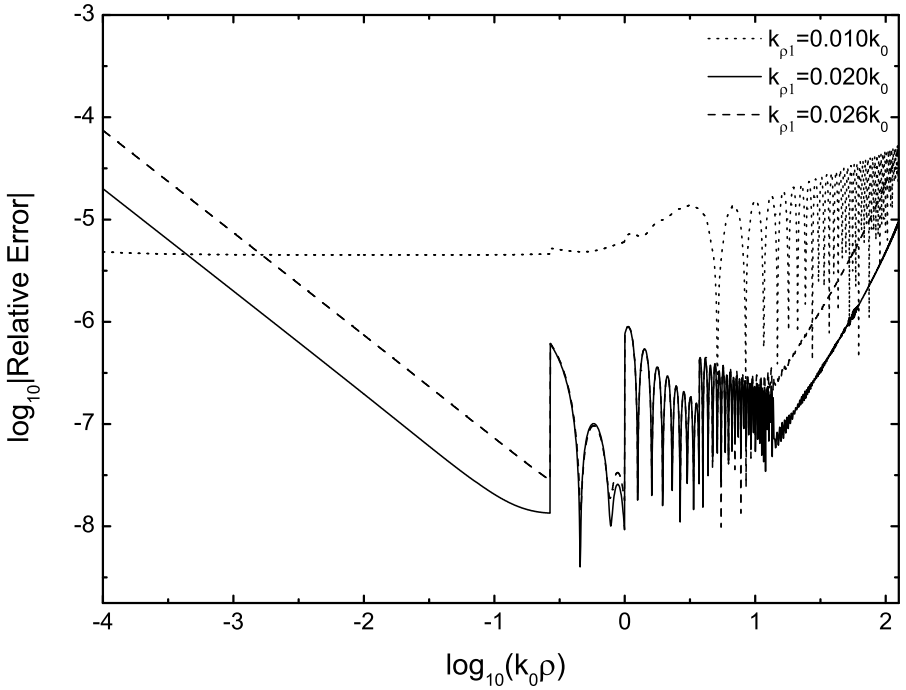

Figure 2.11: Relative errors of the results calculated by the MFHT filter for the Sommerfeld identity (2.80), when $z = 1$ mm, $f = 100$ GHz, and $k_{\rho 1} = 0.01k_0$, $0.02k_0$ and $0.026k_0$, respectively.

GHz and 30 GHz, respectively. For the two elements of the dyadic Green's function, G_{xz}^{AJ} and G_{zz}^{AJ}, the formulations of (2.77) and (2.76) are used for the MFHT method, respectively. For the lossy media shown in Fig. 2.19 [133], the material at the bottom is chosen as FR-4, which is widely used as the dielectric substrate on printed circuit boards. The top material is less lossy than FR-4, referred to as material A. The complex permittivities of the FR-4 and material A are dependent on the operating frequency [134, 133], which are not explicitly expressed here. The source point is located at the interface between the two lossy layers, while the observation point is at the interface between the free space and the first lossy layer. The SWP's are in the fourth quadrant of k_ρ plane and the branch-point singularity is on the real axis. When $k_{\rho 1} = 0.015k_0$, the smooth input function of the SI is obtained along the deformed SIP, as shown in

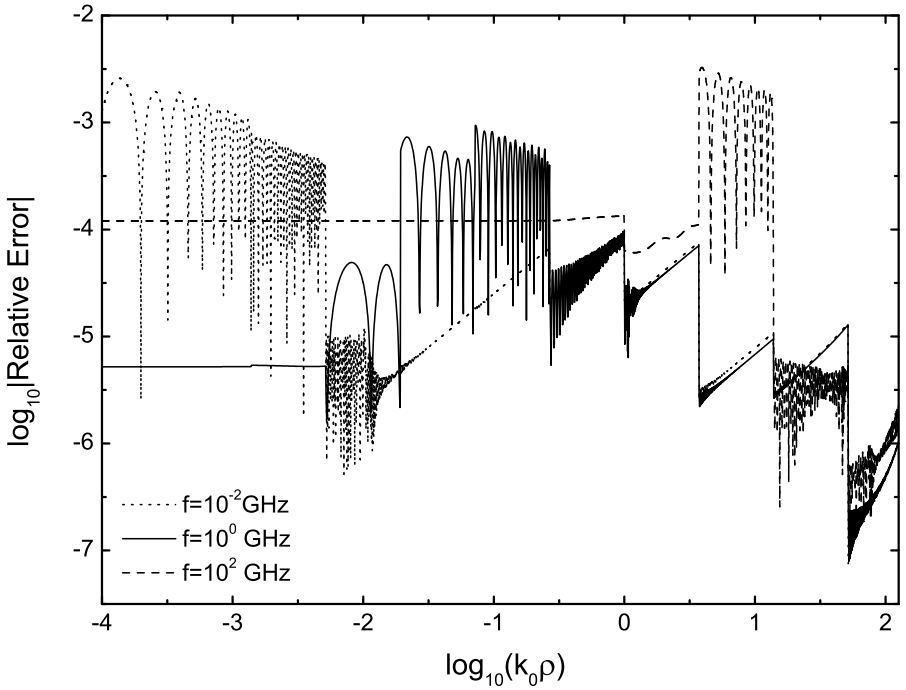

Figure 2.12: Relative errors of the results calculated by the MFHT filter for the Sommerfeld identity (2.73), where $z = 1$ mm and $k_{\rho 1} = 0.02k_0$, at $f = 10$ MHz, 1 GHz and 100 GHz, respectively.

Fig. 2.20. The sampling is adequate to capture the characteristic of the spectral-domain Green's function $\widetilde{G}_{xx}^{AJ}$. Figure 2.21 and Figure 2.22 demonstrate the MFHT-based results for G_{xx}^{AJ} and G_{zx}^{AJ}, respectively. The computational results based on the MFHT method agree very well with the numerical integration results when the operating frequencies are 0.3 GHz, 3 GHz and 30 GHz, respectively. For each case above, the CPU time used for the MFHT algorithm is within 20 seconds on a 2.8 GHz personal computer with 1 GB RAM.

It can be inferred from the numerical examples that the MFHT filter algorithm has excellent accuracy and efficiency when solving the problems with singularities in the input function. When the MFHT method is applied to the calculation of the spatial-domain Green's function, the complicated extraction of contribution of the SWP's is

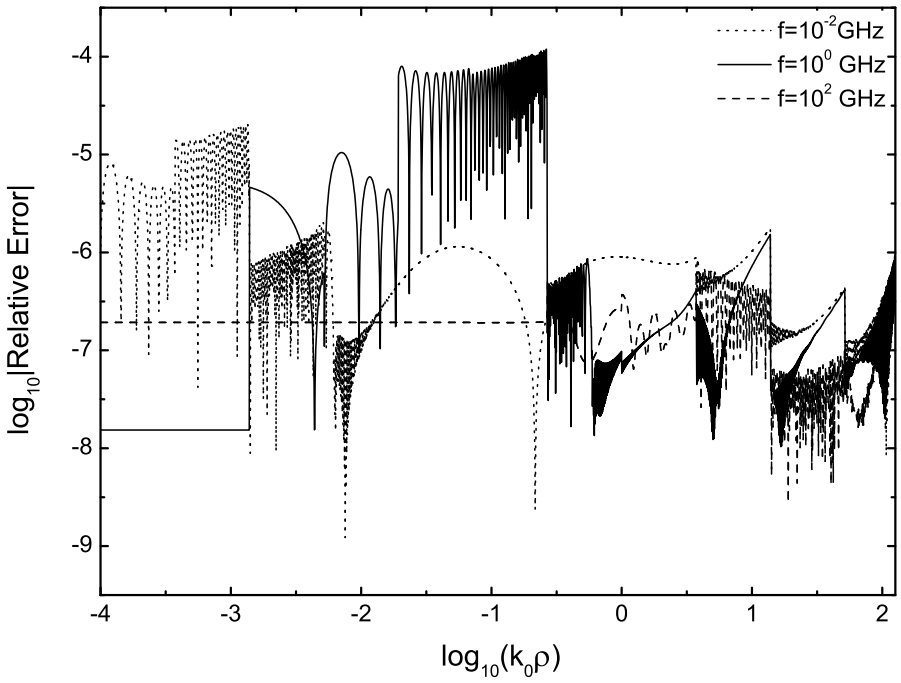

Figure 2.13: Relative errors of the results calculated by the MFHT filter for the Sommerfeld identity (2.79), when $z = 1$ mm and $k_{\rho 1} = 0.02k_0$, at $f = 10$ MHz, 1 GHz and 100 GHz, respectively.

completely avoided. In addition, the MFHT method proposed in this thesis overcomes the difficulties arising when the traditional FHT method fails, since it can successfully deal with the semi-open and open multilayered problems. But it should be noticed that the accuracy of this method cannot be guaranteed when ρ exceeds the scheduled maximum value. Therefore, the valid application range of the MFHT method is limited to the near and intermediate fields. As such, a remedy of this method is to apply the extrapolation method to the extension of the valid range of ρ.

2.6 Conclusion

In this chapter, a modified fast Hankel transform filter algorithm has been proposed to calculate the DGF's for the planar multilayered isotropic media. After deforming the

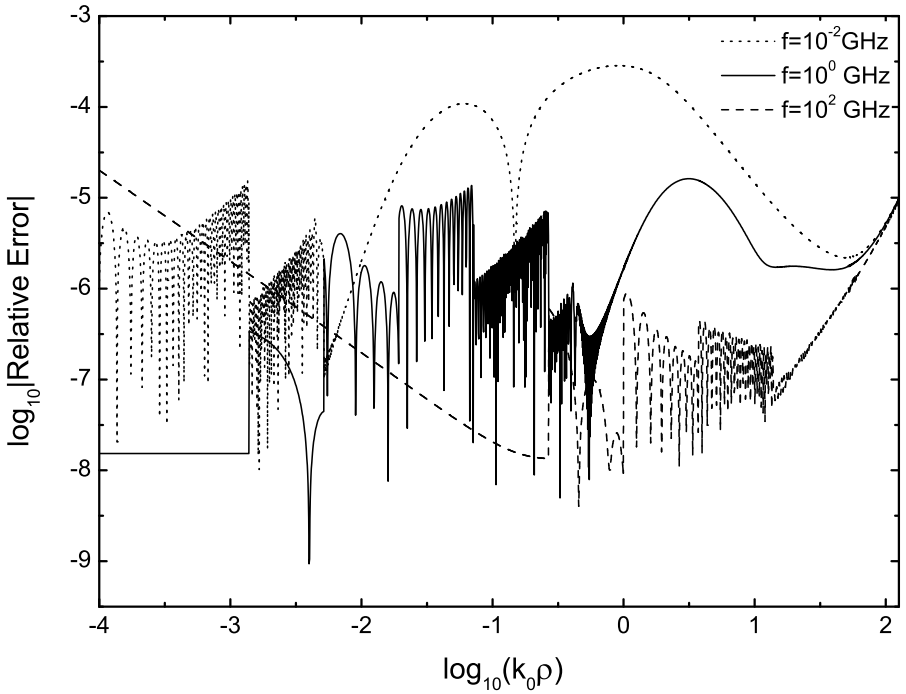

Figure 2.14: Relative errors of the results calculated by the MFHT filter for the Sommerfeld identity (2.80), when $z = 1$ mm and $k_{\rho 1} = 0.02k_0$, at $f = 10$ MHz, 1 GHz and 100 GHz, respectively.

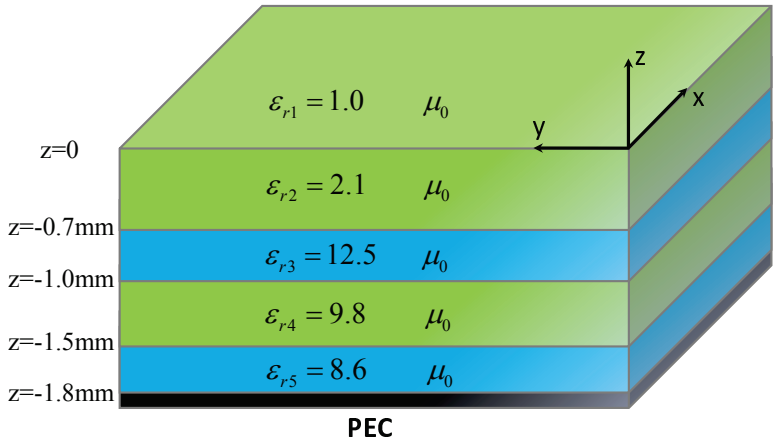

Figure 2.15: Geometry of a four-layer lossless medium above a PEC.

integration path so as to avoid the singularities, the original real integral kernel becomes a complex number and the argument of the Bessel function becomes complex. After

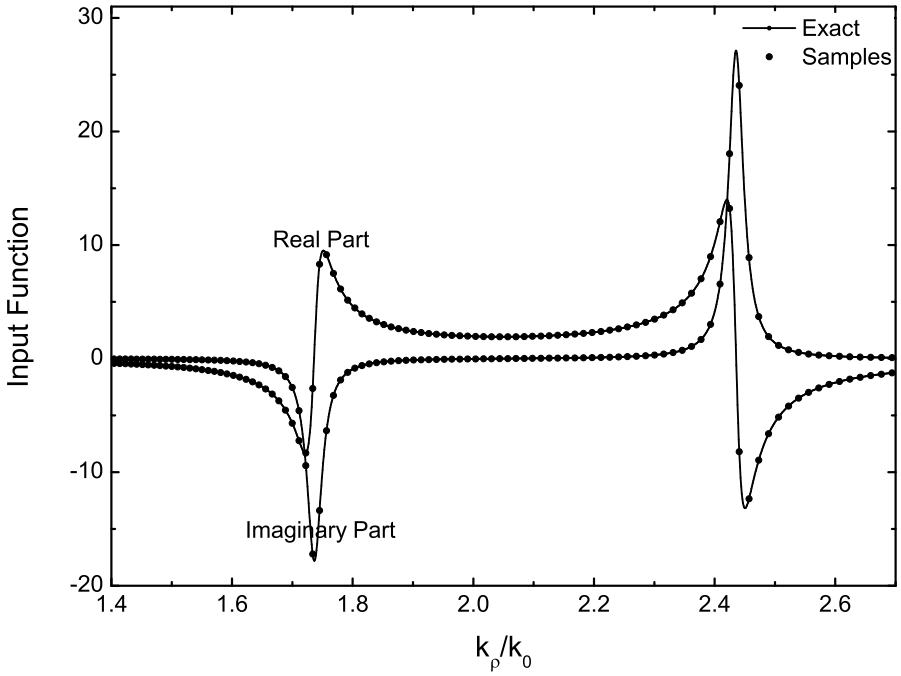

Figure 2.16: Magnitude of $\widetilde{G}_{xz}^{AJ}$ versus k_ρ/k_0, when $m = n = 3$, $z' = z = -1.0$ mm, $k_{\rho 1} = 0.015k_0$ and $f = 30$ GHz.

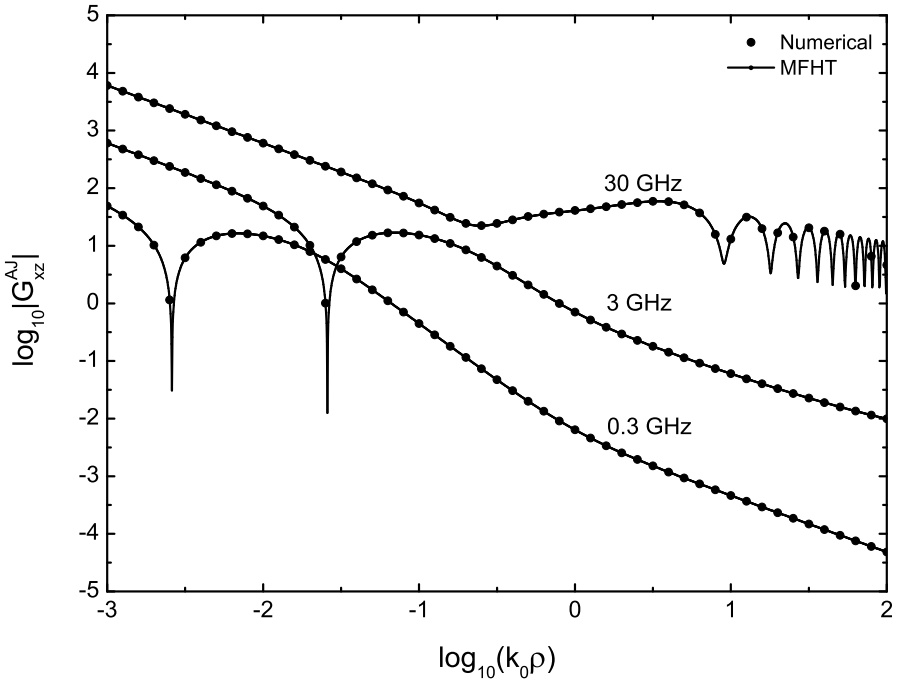

Figure 2.17: Magnitude Comparison of G_{xz}^{AJ} versus ρ, when $m = n = 3$, $z' = z = -1.0$ mm and $k_{\rho 1} = 0.015k_0$, at f=0.3, 3 and 30 GHz, respectively.

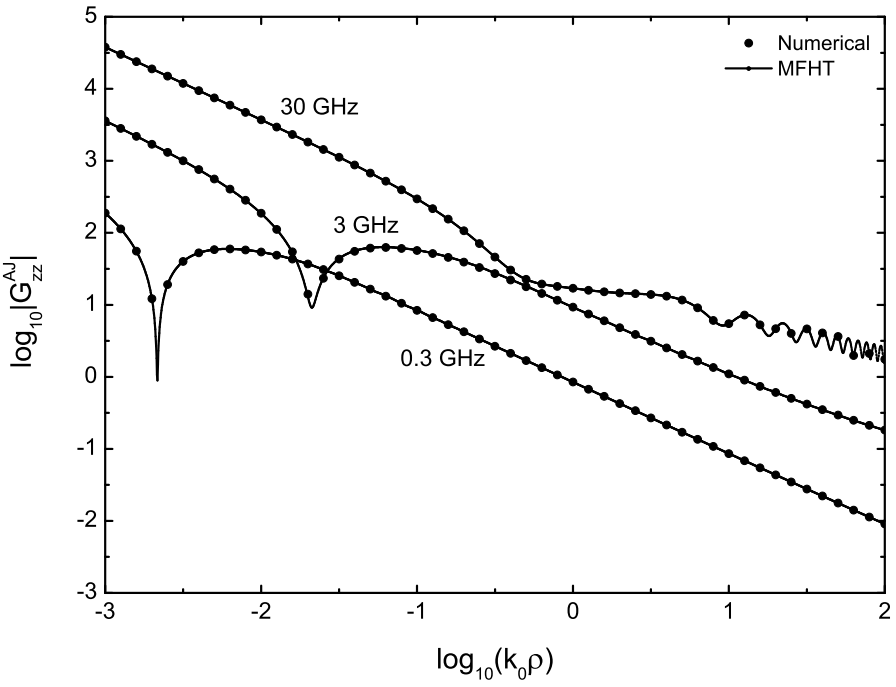

Figure 2.18: Magnitude Comparison of G_{zz}^{AJ} versus ρ, when $m = n = 3$, $z' = z = -1.0$ mm and $k_{\rho 1} = 0.015k_0$, at f=0.3, 3 and 30 GHz, respectively.

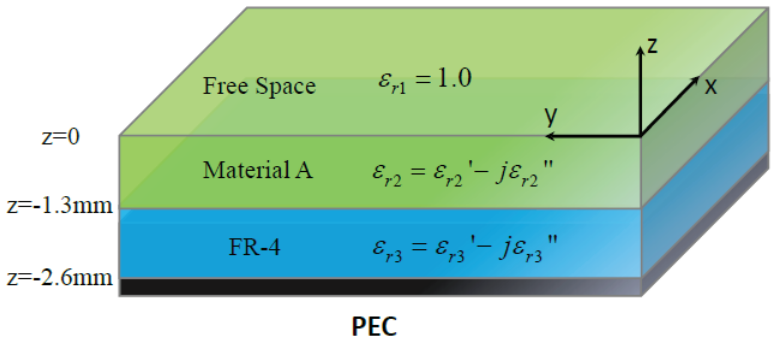

Figure 2.19: Geometry of two-layer lossy media above a PEC.

certain mathematical treatment of complex-argument Bessel function, the traditional FHT filter algorithm is used for each expansion term. The valid range of crucial parameters involved in the deformed integration path have been discussed and determined through numerical examples. One key benefit of the method is that the complicated extraction of contribution of the SWP's singularity can be completely avoided, which is

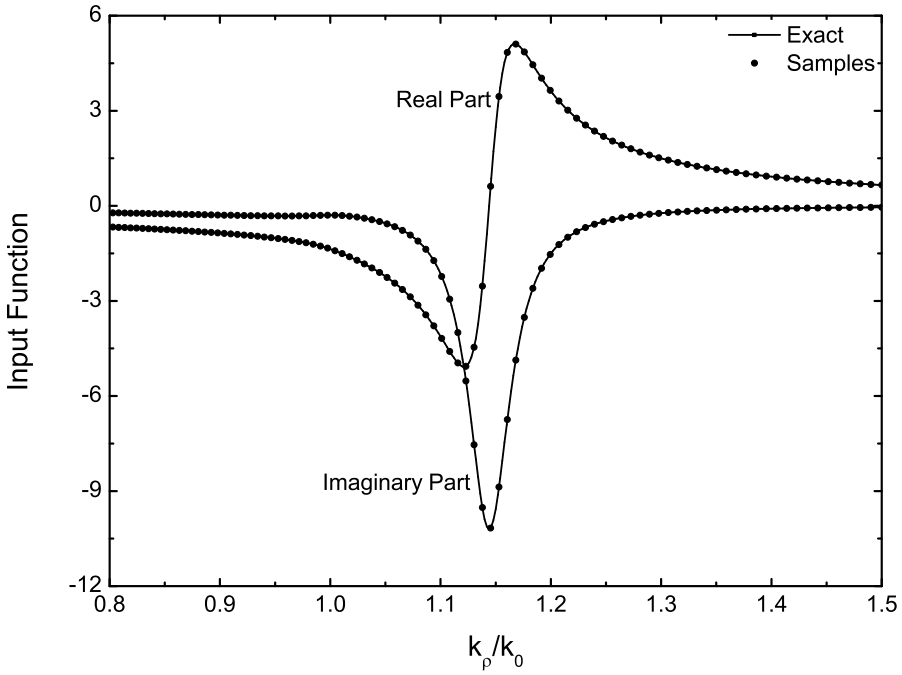

Figure 2.20: Magnitude of $\widetilde{G}_{xx}^{AJ}$ versus k_ρ/k_0, when $m = 2$, $n = 1$, $z' = -1.3$ mm, $z = 0$ mm, $k_{\rho 1} = 0.015k_0$ and f =30 GHz.

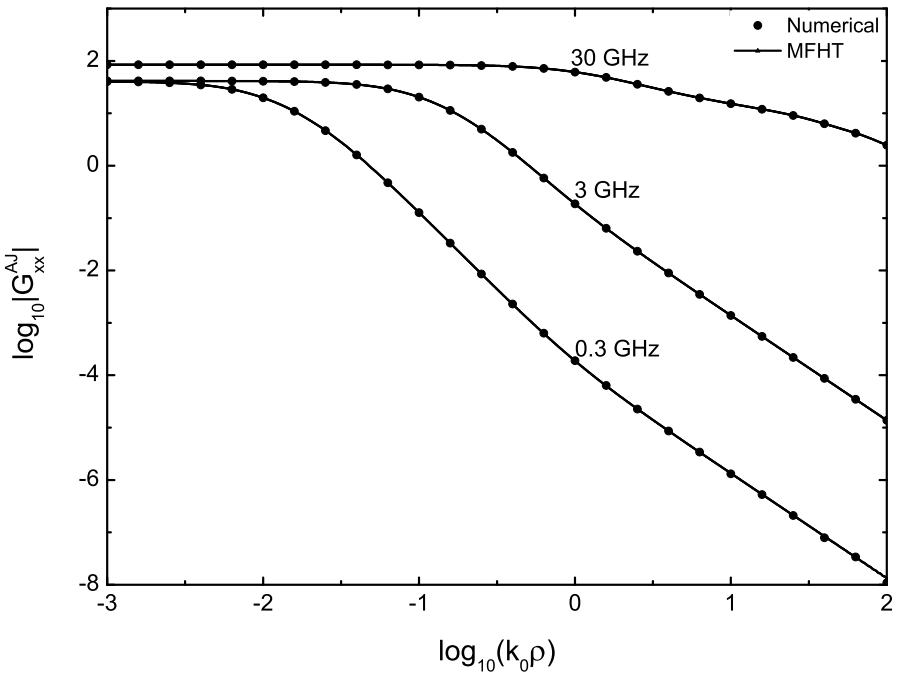

Figure 2.21: Magnitude Comparison of G_{xx}^{AJ} versus ρ, when $m = 2$, $n = 1$, $z' = -1.3$ mm, $z = 0$ mm and $k_{\rho 1} = 0.015k_0$, at f =0.3, 3 and 30 GHz, respectively.

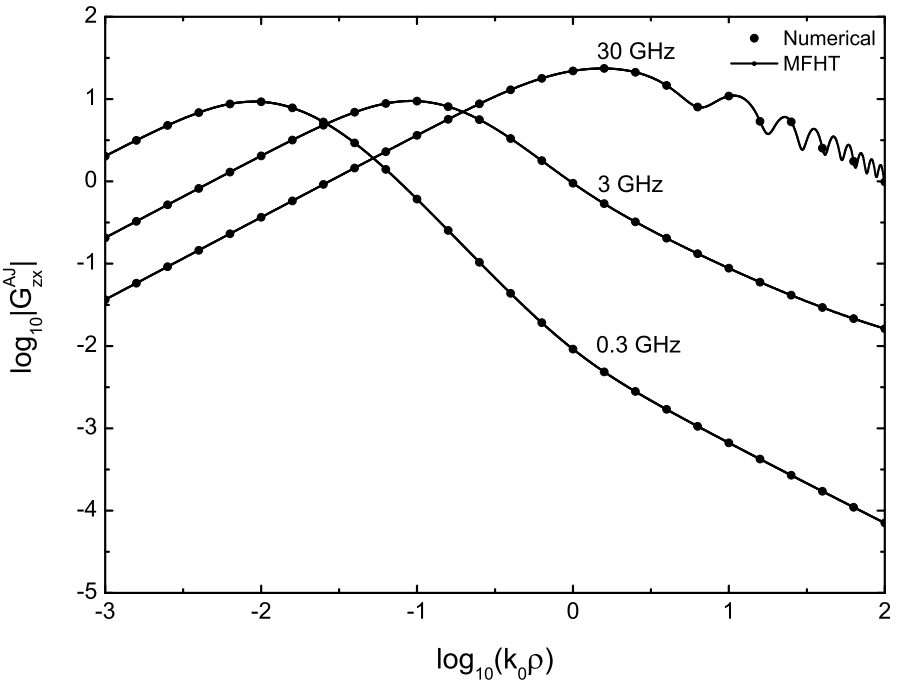

Figure 2.22: Magnitude Comparison of G_{zx}^{AJ} versus ρ, when $m = 2$, $n = 1$, $z' = -1.3$ mm, $z = 0$ mm and $k_{\rho 1} = 0.015k_0$, at f =0.3, 3 and 30 GHz, respectively.

attributed to the deformed SIP. Since the rapidly oscillating and slowly convergent SI's are transformed into the discrete convolution, the efficiency of the calculation of SI's can be greatly improved. The great accuracy and efficiency of the modified algorithm have been demonstrated by the numerical examples of Sommerfeld identities and multilayered problems. In addition, another significance of the MFHT method, in view of its excellent performance in both accuracy and robustness, is that it can overcome the difficulties arising when the traditional FHT method fails. It can successfully deal with the semi-open and open multilayered problems. Thus, the MFHT method provides a powerful tool for the calculation of DGF's for a general multilayered problem. But one limitation of the MFHT method is that the valid application range is confined to the near and intermediate fields.

Chapter 3

Fast Solution of Dyadic Green's Function for Multilayered Isotropic Medium

3.1 Introduction

All these studies on the efficient evaluation of DGF's in the multilayered medium have been motivated by the fact that printed geometries in the multilayered environment have found increasingly more use in the designs of low-profile, light-weight and multifunction antennas, and microwave integrated circuits [5, 6, 7, 8, 9, 135, 45, 17, 18]. Generally, the DGF's are expressed in terms of SI's, which cannot be analytically calculated. The numerical integration of SI's requires an enormous amount of computational time since the spectral-domain Green's function associated with Bessel functions and singularities is highly oscillating and slowly decaying. To address this bottleneck,

several efficient methods have been proposed to expedite the computation of the SI's [34, 35, 36, 20, 37, 38, 39, 40, 41]. Since theoretical investigation of these methods has extended over many years, it is desirable to present a brief sketch of various algorithms.

The essence of DCIM is to approximate spectral-domain Green's functions in terms of complex exponentials using the GPOF method, so the spatial-domain Green's function can be analytically derived in closed form via the Sommerfeld identity. The first research work published on this method for the multilayered problems was carried out by Fang [98]. Then, the well-known two-level sampling algorithm was proposed to reduce the number of samples required for the exponential approximation [43]. However, the two-level approach, together with the explicit extraction of the SWP's [32, 33, 49, 126], is capable of approximating spherical and cylindrical wave components, but not the lateral waves. To overcome this shortcoming, the three-level algorithm [51] and the uniform asymptotic expansion technique [136] were recently proposed to calculate the DGF's over all distance ranges.

The WFM utilizes a window function as a convolution kernel to the spatial-domain Green's function in order to accelerate the function's decay in the spectral domain. The fast-decaying window function in the spectral domain effectively provides a steep descent path for the integration, without any information of a possible steep descent path. Then the spatial-domain Green's function is approximated by the second-order Taylor expansion.

The MFHT method transforms the SI's with a smooth integrand into linear discrete convolutions. The convolution results can be considered as the system response of a digital filter. In order to avoid the SWP's and branch-point singularities, the SIP is

deformed into the first quadrant, but the original real integral kernel becomes a complex number. The Bessel function with a complex argument can be split into the product of two Bessel functions. Then, the traditional FHT filter algorithm is used for each expansion term.

Practically, the motivation of studying the fast approximation methods is to improve the efficiency of the evaluation of multilayered Green's functions. The DCIM, WFM, and MFHT method are well known fast approximation techniques used for the SI's. But the previous work only deal with the fast methods in an independent manner and lack a highly comparable scheme. Their accuracy and efficiency for calculating the DGF's have not yet been examined and compared so far. one of the aims of the present study is to carefully examine the robustness and efficiency of the three fast methods for calculating the DGF's in a multilayered medium. The explicit discussion on the valid application ranges of the three fast methods may provide a useful guideline for the multilayered problems in selection of suitable fast methods to calculate the DGF's. The comparison of accuracy and efficiency for the three fast methods may have significant impact on both offering a clearer explanation for the pros and cons of each method and providing guidelines for the development of corresponding computer-aided design tools.

This chapter starts with a brief introduction of the two fast methods, i.e., DCIM and WFM. Since the MFHT method has been introduced in the preceding chapter, its formulations are omitted in this chapter. The introduction is in an itemized format that would help to clearly point out the main concepts of these methods and parameterized studies. Then, in an effort to provide a quantitative measure of the applicable range and limitations, the accuracy and efficiency of the three methods will be examined through

numerical examples. Then we will give a critical discussion on the possible sources of errors, their remedies, detailed discussions on the advantages, disadvantages, restrictions and range of validity for the three fast methods.

3.2 Discrete Complex Image Method

The DCIM basically approximates the spectral-domain Green's function in terms of complex exponentials using the Prony's method or the GPOF method, and then, the spatial-domain Green's function can be represented in closed form via the well-known Sommerfeld identity. According to the number of sampling subsections of the integration path, the DCIM is usually categorized into one-level DCIM and two-level DCIM [42, 37, 43]. Compared to the two-level DCIM, the one-level approximation approach is lack of enough robustness and availability of the development of CAD software. This is due to the fact that the one-level DCIM requires the prior investigation of the behavior of spectral-domain Green's functions and then the iterative performance to find the most suitable selection of approximation parameters. Therefore, the popular two-level DCIM is employed in this work. The detailed procedure of the two-level DCIM and the selection of crucial parameters are discussed in the following sections.

3.2.1 Formulation of two-level DCIM

There are two major advantages for the DCIM approximation to be performed in two levels. The first one is to alleviate the necessity of studying the property of spectral-domain Green's functions in advance. The second one is to overcome the difficulties

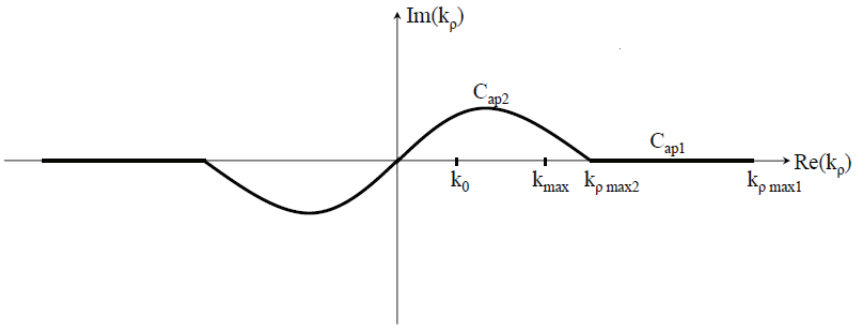

Figure 3.1: The Sommerfeld integral path of two-level DCIM.

caused by the trade-off between the sampling range and the sampling period. The first level of the approximation is carried out along the path C_{ap1} while the second level is along the path C_{ap2}, as shown in Fig. 3.1.

In the spectral domain, according to the horizontal distance between the source point and the observation point, there are two different sampling approaches. For the near field region, the sampling approach is to directly sample the spectrum for a constant value of z. For the far field region, the sampling approach is to extract the representations of the contribution of SWP's $\widetilde{G}_{sw}$ from the spectral-domain Green's function, and then, sample the resulting terms, $\widetilde{G} - \widetilde{G}_{sw}$. The sampling path for both approaches, as shown in Fig. 3.1, is defined by the mappings:

1. For the first level and along C_{ap1},

$$k_{zm} = -jk_m \left[T_{02} + t\right] \qquad 0 \le t \le T_{01} \tag{3.1}$$

2. For the second level and along C_{ap2},

$$k_{zm} = k_m \left[-jt + (1 - \frac{t}{T_{02}}) \right] \quad 0 \leq t \leq T_{02} \tag{3.2}$$

where t is the real running variable of the sampling along the corresponding path. k_m and k_{zm} are the wavenumber and its z component in the source layer m, respectively. Since the integration path in Fig. 3.1 is in the first and third quadrants to exclude the singularities, the smoothness of the integrand can be obtained, which is the requirement of the approximation algorithm. However, since both approximation methods require uniform sampling along a real variable, it is necessary to map the complex variable k_ρ to the real variable t, as defined in (3.1) and (3.2). It should be noted that, compared to the Prony's method, the GPOF method is more robust and less noise sensitive [137, 101].

Note that in the one-level approach, the quasistatic terms of the spectral-domain Green's function should be extracted, which can be found by looking for the limiting terms as $k_\rho \to \infty$ in the form of exponentials. In the application of the two-level approach, the approximation of the spectral-domain Green's functions on the path C_{ap1} via complex images can be considered as the extraction of quasistatic terms in addition to some dynamic terms [102].

Then, the sampled spectral-domain Green's functions are approximated in terms of

complex exponentials by the GPOF method

$$\begin{aligned}\widetilde{G} &\cong \frac{1}{2jk_{zm}}\left[\sum_{n=1}^{N_1}\alpha_{n1}e^{\beta_{n1}t}+\sum_{n=1}^{N_2}\alpha_{n2}e^{\beta_{n2}t}\right] \\ &= \frac{1}{2jk_{zm}}\left[\sum_{n=1}^{N_1}a_{n1}e^{-b_{n1}k_{zm}}+\sum_{n=1}^{N_2}a_{n2}e^{-b_{n2}k_{zm}}\right]\end{aligned} \tag{3.3}$$

where α and β are the coefficients and exponnents obtained from the GPOF method, $N_{1,2}$ is the number of exponentials used at the corresponding level, and a and b are obtained in terms of α and β in (3.1)-(3.2).

It is widely recognized that when the spectral-domain Green's functions are approximated by exponentials, the SI's can be evaluated analytically by the well-known Sommerfeld identity.

$$\frac{e^{-jk_m r}}{r} = \int_{-\infty}^{\infty}\frac{e^{-jk_{zm}|z|}}{2jk_{zm}}H_0^{(2)}(k_\rho\rho)k_\rho\,dk_\rho \tag{3.4}$$

where $r = \sqrt{\rho^2+z^2}$ is the distance between the source and observation points and the left-hand expression represents a spherical wave in the spatial domain. According to the Sommerfeld identity (3.4), the spatial-domain Green's function can be obtained by:

$$G \cong \frac{1}{4\pi}\left[\sum_{n=1}^{N_1}a_{n1}\frac{e^{-jk_m r_{n1}}}{r_{n1}}+\sum_{n=1}^{N_2}a_{n2}\frac{e^{-jk_m r_{n2}}}{r_{n2}}\right] \tag{3.5}$$

where $r_{n1,n2} = \sqrt{\rho^2-b_{n1,n2}^2}$. Note that (3.5) is the spatial-domain version of (3.3). Moreover, the spatial-domain representations for the contribution of SWP's can also be analytically expressed by the residue technique in closed form.

As briefly outlined above, the two-level DCIM is successful in casting the spatial-domain Green's functions in closed form.

3.2.2 Parameters of DCIM

For the multilayered geometry where the uppermost and lowermost layers are semi-infinite dielectric media, there are two branch-point singularities in the spectral-domain Green's functions, specifically in the wavenumbers of the outermost layers. In addition to the branch-point singularities, there are some SWP's between the minimum and maximum wavenumbers involved in the geometry, that is, in the range of $k_{min}(= k_0\sqrt{\epsilon_{rmin}}) < k_\rho < k_{max}(= k_0\sqrt{\epsilon_{rmax}})$. The number and location of SWP's are dependent on the electrical thicknesses and dielectric constants of the layers involved.

Before applying the two-level DCIM to the practical problems, four important parameters that must be fixed beforehand are: 1) the values of the sampling ranges T_{01} and T_{02}; 2) the number of samples along the first level C_{ap1} and the second level C_{ap2}.

1. Choose T_{01} to determine the value of $k_{\rho\,max1}$. The value of T_{01} is not critical as long as $k_{\rho\,max1}$ is large enough to pick up the behavior of the spectral-domain Green's function for large k_ρ. Typically, T_{01} is set to be 500.

2. Choose the number of samples along C_{ap1}. Since the magnitudes of the spectral-domain Green's functions are usually smooth beyond $k_{\rho\,max2}$, it is not necessary to have a large number of samples in the period $\left[k_{\rho\,max2},\, k_{\rho\,max1}\right]$. The number of samples along C_{ap1} can be chosen to be 200.

3. Choose T_{02} to make sure $k_{\rho\,max2} > k_{max}$. In order to avoid the singularities along

C_{ap2}, T_{02} can be safely chosen to be 5 based on the permittivities of practical materials.

4. Choose the number of samples along C_{ap2}. Because the singularities still influence the spectrum between 0 and $k_{\rho max2}$ to some extent, the samples in the path C_{ap2} should sufficiently capture the property of the spectrum. Here, we choose the number of samples along C_{ap2} to be 200.

The choice of these parameters does not need a prior investigation of the spectral-domain Green's functions because their values are only based on the parameters of the interested geometries.

3.3 Window Function Method

The WFM utilizes a window function as a convolution kernel to the spatial-domain Green's function, for the sake of accelerating the convergence of spectral-domain Green's function. The fast decaying property of the window function in the spectral domain can successfully result in a steep descent path for the SI without the need of the inherent steep descent path of the spectral-domain Green's function, which may or may not exist.

3.3.1 Formulation of WFM

In order to accelerate the calculation of SI's, the mth-order window function $\psi_a(\rho)$ is expressed as:

$$\psi_a(\rho) = \begin{cases} \left[1 - \left(\frac{\rho}{a}\right)^2\right]^m & \text{if } \rho \le a \\ 0 & \text{otherwise.} \end{cases} \tag{3.6}$$

where a is the support size of the window function [55].

When the window function is convoluted with the spectral-domain Green's function, an identity related with the window function is given by

$$G(\rho; z, z') * \psi_a(\rho) = S_0[\widetilde{G}(k_\rho; z, z')\widetilde{\psi}_a(k_\rho)](\rho) \tag{3.7}$$

where

$$S_n[\widetilde{g}(k_\rho)](\rho) = \int_0^\infty \widetilde{g}(k_\rho) J_n(k_\rho \rho) k_\rho^{n+1} dk_\rho \tag{3.8}$$

$$\widetilde{\psi}_a(k_\rho) = S_0[\psi_a(\rho)](k_\rho) \tag{3.9}$$

For the sake of recovering the function $G(\rho; z, z')$ from its Hankel transform, another formula related to the window function needs to be employed.

$$G(\rho; z, z') * \psi_a(\rho) = M_0 \cdot G(\rho; z, z') + O(a^2) \qquad \rho > a \tag{3.10}$$

where

$$M_0 = \int_{\rho \le a} \psi_a(\rho) d\rho = \frac{\pi a^2}{m+1} \tag{3.11}$$

As a result of (3.7) and (3.10), we can approximate $G(\rho; z, z')$ as

$$G(\rho; z, z') = \frac{1}{M_0} W_0(\rho) + O(a^2), \qquad \rho > a,\ a \to 0 \tag{3.12}$$

To assure the accuracy of the approximation method, an alternative formulation of the spatial-domain Green's function recovered from the convolution is expressed by

$$G(\rho; z, z') = \frac{1}{M_0 r^2} \left[r^2 W_0(\rho) - 2\rho W_1(\rho) + W_2(\rho) \right] + O(a^2) \qquad \rho > 0,\ a \to 0 \tag{3.13}$$

with

$$r^2 = \rho^2 + (z - z')^2 \tag{3.14}$$

$$W_0(\rho) = S_0 \left[\widetilde{G}(k_\rho; z, z') \widetilde{\psi}_a(k_\rho) \right] \tag{3.15}$$

$$W_1(\rho) = S_1 \left[\widetilde{G}(k_\rho; z, z') \widetilde{\psi}^*_a(k_\rho)/k_\rho \right] \tag{3.16}$$

$$W_2(\rho) = S_0 \left[\widetilde{G}(k_\rho; z, z') \widetilde{\psi}^{**}_a(k_\rho) \right] \tag{3.17}$$

and

$$\widetilde{\psi}_a(k_\rho) = \int_0^a \psi_a(\rho) J_0(k_\rho \rho) \rho \, d\rho = o\left(|a k_\rho|^{-m} \right) \tag{3.18}$$

$$\widetilde{\psi}^*_a(k_\rho) = \int_0^a \psi_a(\rho) J_1(k_\rho \rho) \rho^2 \, d\rho = o\left(|a k_\rho|^{-m+1} \right) \tag{3.19}$$

$$\widetilde{\psi}^{**}_a(k_\rho) = \int_0^a \psi_a(\rho) J_0(k_\rho \rho) \rho^3 \, d\rho = o\left(|a k_\rho|^{-m} \right) \tag{3.20}$$

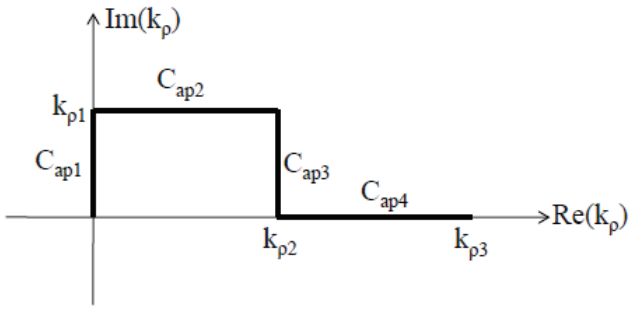

Figure 3.2: The Sommerfeld integral path of window function method.

In view of the above formulations, the fast decaying properties of $\widetilde{\psi}_a(k_\rho)$, $\widetilde{\psi}_a^*(k_\rho)$, and $\widetilde{\psi}_a^{**}(k_\rho)$ ensure that a short integration contour can be chosen without sacrificing much accuracy of the approximation algorithm through the formulations (3.12) and (3.13). The effect of this window function is to provide a steep descent path and accelerate the decaying rate of the integrand of SI's. Then, the spatial-domain Green's functions are recovered from the convolution through two approximation algorithms.

3.3.2 Selection of Integration Contour and Parameters

In order to avoid the SWP and branch-point singularities, the integration contour C_{ap} for the WFM is chosen to possess four straight segments $C_{ap1\sim4}$, as depicted in Fig. 3.2. The values of $k_{\rho1,2}$ on the contour $C_{ap1\sim3}$ are determined by the locations of singularities. As mentioned above, the singularities usually fall on the real axis $[0, k_{max}]$ or the fourth quadrant of the k_ρ plane. Hence, $k_{\rho2}$ is set to be $k_{max}\left(= k_0 \cdot \sqrt{\epsilon_{r\,max}}\right)$.

The value of $k_{\rho1}$ is quite flexible as long as the prior condition of the approximation algorithm that the magnitude of spectral-domain Green's function should be smooth along the integration path C_{ap2} is satisfied. Here, we choose the value of $k_{\rho1}$ to be

$0.01k_0$.

The window support a is a crucial parameter to the accuracy and efficiency of this method, which is determined by the second-order accuracy $O(a^2)$ of approximations algorithms (3.12)-(3.13). In [55], a is suggested to be 0.001 for the numerical examples. However, this selection renders the numerical results only accurate for a small horizontal distance range. Through a large amount of numerical experiments, the value of a is recommended to be 0.0001 and thus the valid range of horizontal distance can be up to tens of the wavelength.

In terms of (3.18)-(3.20), the order m of the window function should be large enough to make sure that $\widetilde{\psi}_a(k_\rho)$, $\widetilde{\psi}^*_a(k_\rho)$, and $\widetilde{\psi}^{**}_a(k_\rho)$ have a fast decaying behavior. But a larger value of m unexpectedly results in a longer length of the fourth segment of SIP, which may in turn affect the efficiency of calculation. m is selected to be 5.

The length of the fourth segment C_{ap4} is mainly determined by the decaying properties of (3.18)-(3.20). To maintain the second-order accuracy $O(a^2)$ in the formulations (3.12)-(3.13), $k_{\rho 3}$ in the contour C_{ap4} is set to be $\frac{20}{a}$.

It is worth noting that Cai et al. [55] employed Gauss quadratures and three identities to calculate of the spectral-domain window functions (3.18)-(3.20), which is complicated since different algorithms are used here. In this work, for the sake of simplicity and good efficiency, we employ the fast Hankel transform to evaluate them.

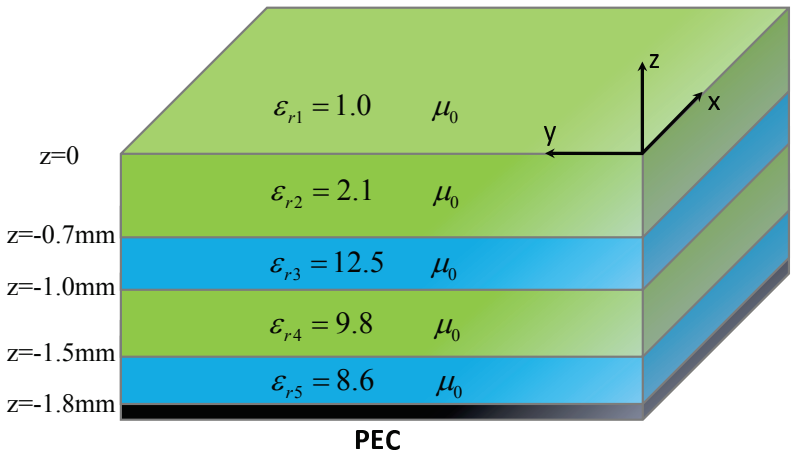

Figure 3.3: Geometry of a five-layer lossless medium above a PEC.

3.4 Numerical Results and Discussions

3.4.1 Numerical Examples

In order to provide a quantitative measurement of the valid distance ranges and application limitations, the following numerical studies involve the application of the three methods to the calculation of the spatial-domain Green's functions, in a lossless or lossy multilayered medium. It should be noted that the efficiency comparison of the numerical results would be meaningful only within a required accuracy criterion. Hence, the same accuracy criterion (the smaller value between a relative error 10^{-3} and an absolute error 10^{-10}) is set for the numerical examples. For notation purposes, m represents the layer number of the source point, n represents the layer number of the field point, z' represents the source position, z represents the observation position, and all height dimensions are given in millimeters.

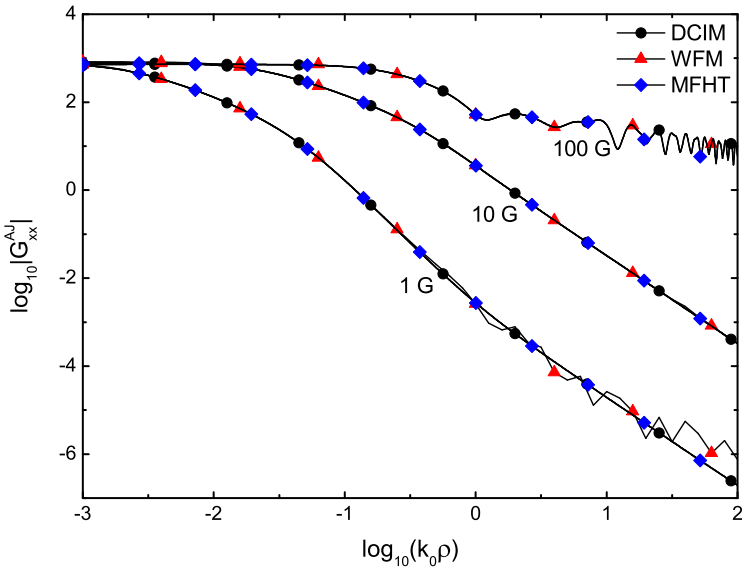

Figure 3.4: Magnitude Comparison of G_{xx}^{AJ} versus ρ for Fig. 3.3, where $m = n = 2$, $z' = -0.7$ mm, $z = -0.6$ mm and $f = 1,\ 10,\ 100$ GHz, respectively.

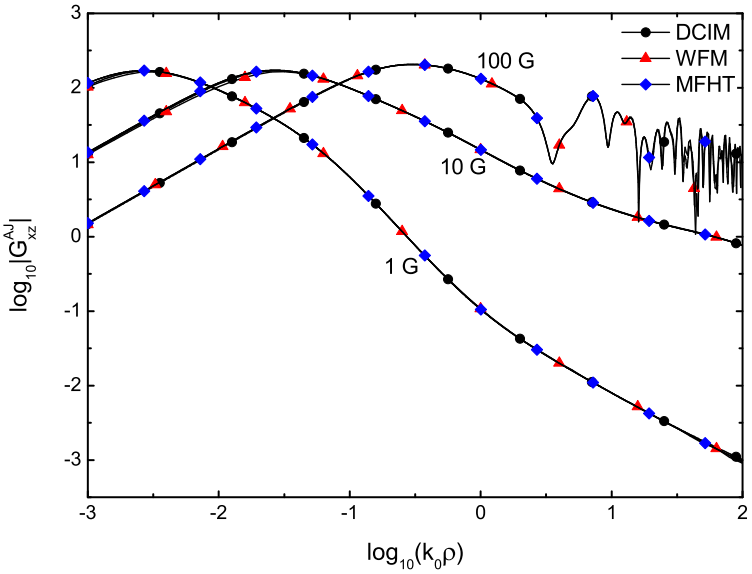

Figure 3.5: Magnitude Comparison of G_{xz}^{AJ} versus ρ for Fig. 3.3, where $m = n = 2$, $z' = -0.7$ mm, $z = -0.6$ mm and $f = 1,\ 10,\ 100$ GHz, respectively.

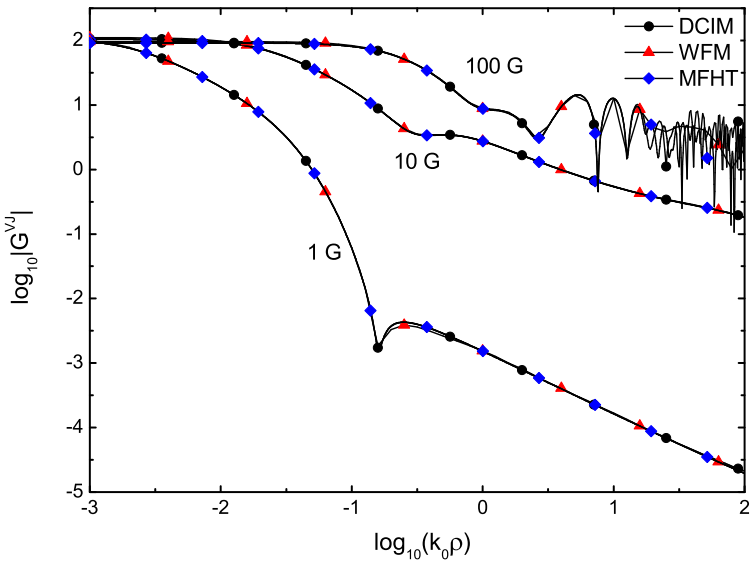

Figure 3.6: Magnitude Comparison of G^{VJ} versus ρ for Fig. 3.3, where $m = n = 2$, $z' = -0.7$ mm, $z = -0.6$ mm and $f = 1,\ 10,\ 100$ GHz, respectively.

The first study involves a five-layer lossless medium shown in Fig. 3.3. The relative permittivities of the dielectric media are $\epsilon_{r1} = 1.0$, $\epsilon_{r2} = 2.1$, $\epsilon_{r3} = 12.5$, $\epsilon_{r4} = 9.8$, and $\epsilon_{r5} = 8.6$. The thicknesses of layers are set to be $D_2 = 0.7$ mm, $D_3 = 0.3$ mm, $D_4 = 0.5$ mm, and $D_5 = 0.3$ mm. The source point and the observation point are both in the second layer, with $z' = -0.7$ mm and $z = -0.6$ mm. Based on the three fast methods, Figs. 3.4-3.6 depict the magnitudes of G_{xx}^{AJ}, G_{xz}^{AJ} and G^{VJ}, respectively. For the three figures, the operating frequency is selected to be 1 GHz, 10 GHz and 100 GHz, respectively. Generally, TE and TM surface waves are both supported in a multilayered structure. But certain components of the DGF's for the vector potential, e.g., G_{xx}^{AJ} and G_{zx}^{HJ}, may have the contribution of TE surface waves only, while the Green's function for the scalar potential G^{VJ} and certain components of the DGF's for the vector potential, e.g., G_{xz}^{AJ} and G_{xx}^{HJ}, may have the contributions of both TE and TM surface waves. In

this numerical example, there is only one TM-mode SWP at $k_{\rho p1}^{\mathrm{TM}} = 1.0004k_0$ when the operating frequency is 1 GHz; there is one TM-mode SWP at $k_{\rho p1}^{\mathrm{TM}} = 1.058k_0$ when the operating frequency is 10 GHz; there are three TE-mode SWP's at $k_{\rho p1}^{\mathrm{TE}} = 1.016k_0$, $k_{\rho p2}^{\mathrm{TE}} = 2.260k_0$, and $k_{\rho p3}^{\mathrm{TE}} = 3.038k_0$, and three TM-mode SWP's at $k_{\rho p1}^{\mathrm{TM}} = 1.319k_0$, $k_{\rho p2}^{\mathrm{TM}} = 2.491k_0$, and $k_{\rho p3}^{\mathrm{TM}} = 3.017k_0$, when the operating frequency is 100 GHz. In order to obtain the accurate numerical results based on the two-level DCIM in the far field, the contributions of SWP's should be extracted before the approximation procedure. Here are the implementation parameters of the DCIM, WFM, and MFHT, for this example: for the two-level DCIM, $T_{01} = 500$, $T_{02} = 5$, number of samples is 1024 for each path; for the WFM, a=0.0001, m=5, $k_{\rho 1} = 0.01$, $k_{\rho 2} = 5.0k_0$, and $k_{\rho 3} = 20/a$; for the MFHT, the filter coefficients and SIP are selected the same as them in Chapter 2. In view of the Figs. 3.4-3.6, the MFHT-based numerical results are represented by the symbol ■ and the accuracy of this method in the near and intermediate fields has been proven in the preceding chapter. It can be observed that the DCIM-based results represented by the symbol • and the WFM-based results represented by the symbol ▲ have good agreement with the results obtained by the MFHT method in the near and intermediate fields. However, when the magnitude of numerical results is smaller than 10^{-5}, the numerical error of WFM-based results starts to be unacceptable, which will be discussed in detail in the following section.

The second numerical example considers a two-layer lossy dispersive medium backed by a PEC plane, as shown in Fig. 3.7. The parameters of the multilayered materials have been described in the numerical examples of last chapter, which are not explicitly listed here. The two lossy layers are of 1.3 mm in thickness. The source point is located at

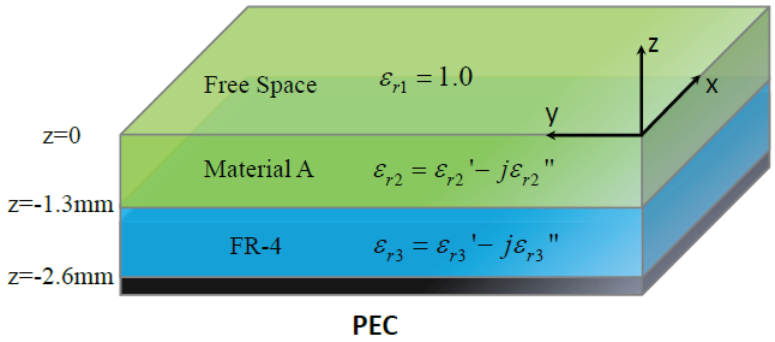

Figure 3.7: Geometry of two-layer lossy media above a PEC.

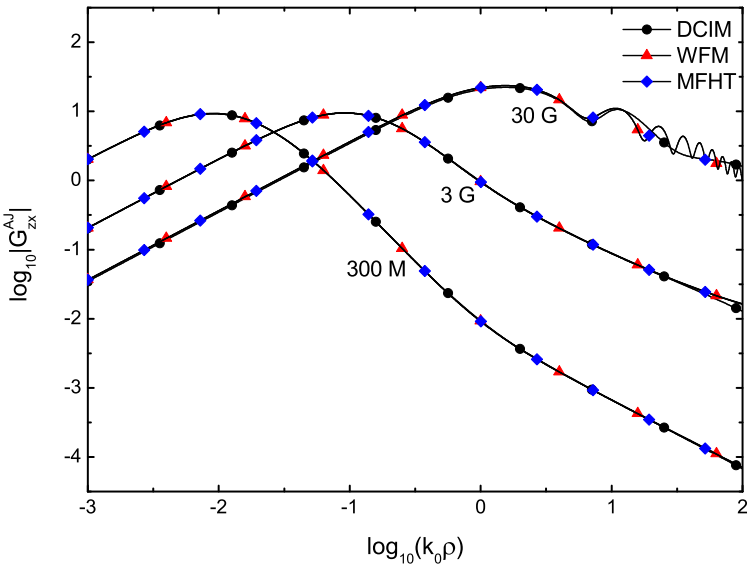

Figure 3.8: Magnitude Comparison of G_{zx}^{AJ} versus ρ for Fig. 3.7, where $m = 2$, $n = 1$, $z' = -1.3$ mm, $z = 0$ and $f = 0.3,\ 3,\ 30$ GHz, respectively.

the interface between the two lossy layers, while the observation point is at the interface between the free space and the first lossy layer. For the lossy multilayered medium, the SWP's singularities are located in the fourth quadrant of k_ρ plane and the possible branch-point singularity is also related with the outermost layer, which is the free space in this case. As stated earlier, to improve the accuracy of the approximation results of

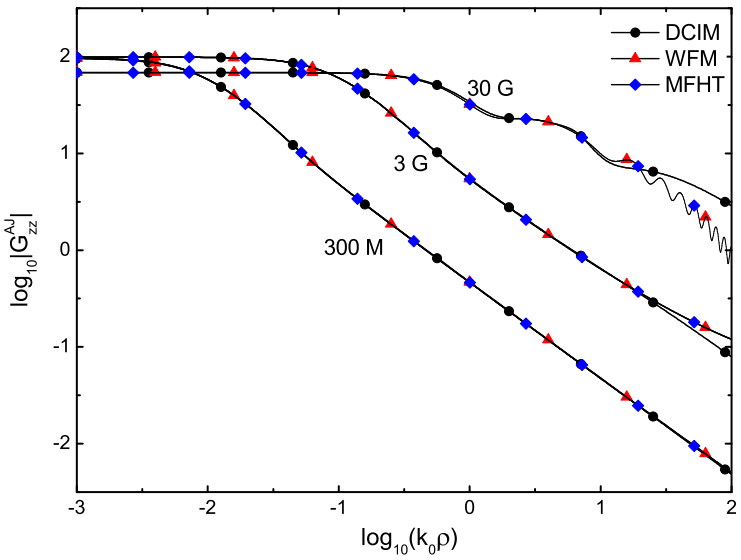

Figure 3.9: Magnitude Comparison of G_{zz}^{AJ} versus ρ for Fig. 3.7, where $m = 2$, $n = 1$, $z' = -1.3$ mm, $z = 0$ and $f = 0.3,\ 3,\ 30$ GHz, respectively.

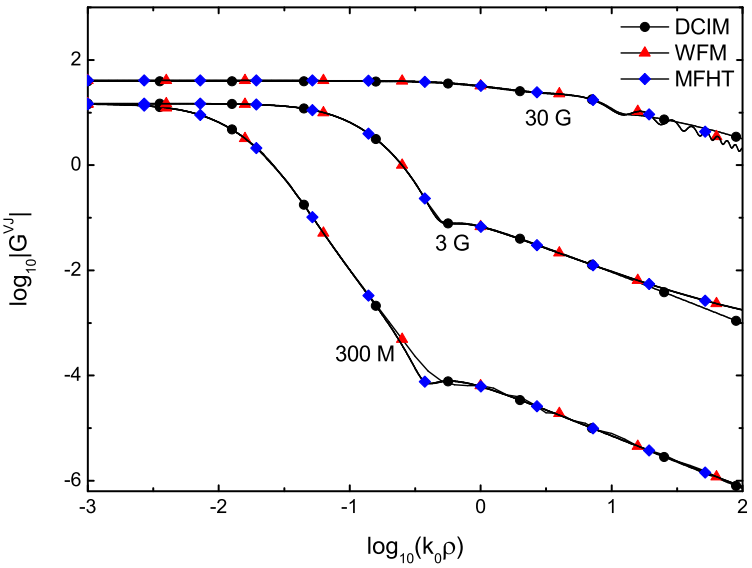

Figure 3.10: Magnitude Comparison of G^{VJ} versus ρ for Fig. 3.7, where $m = 2$, $n = 1$, $z' = -1.3$ mm, $z = 0$ and $f = 0.3,\ 3,\ 30$ GHz, respectively.

DCIM in the far field, the extraction of the contributions of singularities is a necessary pre-approximation process. However, the determination of tens of the singularities, including surface wave singularities, leaky wave singularities and improper singularities, are quite complicated and effort-consuming for the lossy multilayered problems [138]. Moreover, the energy of the surface waves decays exponentially with the horizontal distance ρ and the contribution of the surface waves will no longer dominate in the far field region. Therefore, when the DCIM is applied, the approximation results without the extraction of the contribution of SWP's may be acceptable in this case. Figure 3.8 plots the magnitudes of G_{zx}^{AJ} obtained by the three methods, at three different frequencies, i.e., 300 MHz, 3 GHz and 30 GHz, respectively. With the same operating frequencies, Fig. 3.9 and Fig. 3.10 plot the magnitudes of G_{zz}^{AJ} and G^{VJ} obtained by the three methods, respectively. For the two-level DCIM, $T_{01} = 500$, $T_{02} = 10$ and number of samples is 1024 for each path. For the WFM and MFHT method, the selection of parameters is the same as the first example. The magnitudes of the Green's functions in the three figures also show good agreement among the numerical results based on the three methods in the near fields. However, the deviation between the DCIM-based results and the reference results obtained by the MFHT method begins from the intermediate field, which can be alleviated by extracting the contribution of SWP's.

For the five-layer lossless problem and two-layer lossy problem, the computational times taken by the three methods are all listed in Table 3.1. Generally speaking, the computational time is mainly dependent on the required accuracy. We tabulate the computational time with the accuracy requirement for a large range of operating frequencies and distance. The 2.66 GHz PC was used to run all these numerical experiments, based on

Table 3.1: Comparison of the CPU Time With the same Accuracy Criterion for Computing Vector Potentials in Space Domain (based on Intel Duo Core2, 2.66 GHz PC running Fortran)

Example	**DCIM** sec.	**WFM** sec. (52 points)	**MFHT** sec.	**MFHT** sec./per point
G_{xx}^{AJ} in Fig.3.4 (1 GHz)	59.72	4349.51	10.21	0.52
G_{xx}^{AJ} in Fig.3.4 (10 GHz)	57.23	5236.47	10.71	0.49
G_{xx}^{AJ} in Fig.3.4 (100 GHz)	59.15	6272.96	11.09	0.49
G_{xz}^{AJ} in Fig.3.5 (1 GHz)	70.94	4365.92	19.27	0.50
G_{xz}^{AJ} in Fig.3.5 (10 GHz)	66.19	5115.17	19.27	0.52
G_{xz}^{AJ} in Fig.3.5 (100 GHz)	70.70	6174.26	21.55	0.50
G^{VJ} in Fig.3.6 (1 GHz)	65.82	4600.87	159.58	0.64
G^{VJ} in Fig.3.6 (10 GHz)	64.09	5466.53	603.37	1.16
G^{VJ} in Fig.3.6 (100 GHz)	65.57	6594.77	2366.33	3.22
G_{zx}^{AJ} in Fig.3.8 (0.3 GHz)	60.83	3764.85	11.03	0.53
G_{zx}^{AJ} in Fig.3.8 (3 GHz)	44.64	4663.09	13.07	0.58
G_{zx}^{AJ} in Fig.3.8 (30 GHz)	42.06	5833.83	11.60	0.55
G_{zz}^{AJ} in Fig.3.9 (0.3 GHz)	65.90	3717.43	41.22	0.61
G_{zz}^{AJ} in Fig.3.9 (3 GHz)	44.14	4696.11	165.30	0.83
G_{zz}^{AJ} in Fig.3.9 (30 GHz)	45.95	5903.62	446.81	1.03
G^{VJ} in Fig.3.10 (0.3 GHz)	57.09	4131.62	57.00	0.53
G^{VJ} in Fig.3.10 (3 GHz)	43.23	5014.97	151.41	0.64
G^{VJ} in Fig.3.10 (30 GHz)	44.71	6298.47	773.38	1.31
200 Different Cases*	$\approx 14,000$	$\approx 23,000$	-	≈ 200

* Without loss of the generality, 200 different numerical experiments are conducted. The vertical position of the observation point is changed for 200 times, while the position of the source point is fixed.

FORTRAN. Compared with the computational time taken by WFM, the time of MFHT method listed in the fifth line of Table 3.1 is very short for calculating the DGF at one observation point. The second and fourth lines in Table 3.1 show the computational

times for the eighteen cases, based on the two-level DCIM and MFHT method respectively. It is observed that the MFHT method requires less time than DCIM for some experiments. Here, in order to adequately sample the spectrum of Green's function, the number of sampling points on each level of DCIM is 1024. The window support parameter of WFM is set to be 0.0001 to extend the application range to the intermediate field. The maximum relative truncation error of the MFHT method is fixed to be 10^{-7}, in order to obtain accurate results in a large region. With the similar accuracy criterion, it can be observed that the average time taken for one numerical experiment is 60 s for the two-level DCIM and 5000 s for the WFM. In contrast, the time taken by the MFHT is significantly reduced, which is due to the fact that the time taken for the digital filter is mainly dependent on the number of singularities and oscillating behavior of the integrand. In view of the computational time used by the three methods, it can be seen that the MFHT method and the DCIM have better efficiency, compared to the WFM. In some cases, the MFHT method performs better than DCIM in terms of efficiency. Moreover, it is worth mentioning that the forms of the numerical results calculated by the DCIM, WFM and MFHT are totally different. The closed-form Green's function is obtained by the DCIM, while WFM and MFHT method are employed to compute the DGF's on discrete points. Table 3.1 also lists the computational time for two hundred different numerical experiments, based on the three fast methods. In the two hundred experiments, the position of source point is fixed and the vertical position of observation point is changed. It is clearly demonstrated that the DCIM offers no apparent superiority and the computational efficiency of MFHT is almost 69 times higher than that of DCIM and 114 times higher than that of WFM.

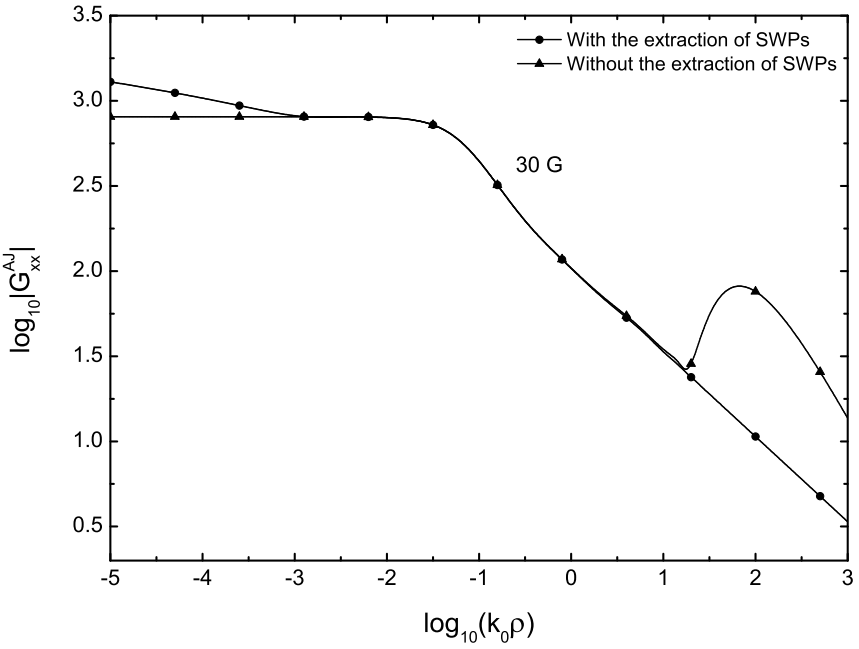

Figure 3.11: Magnitude Comparison of G_{xx}^{AJ} versus ρ for Fig. 3.3, where $m = n = 2$, $z' = -0.7$ mm, $z = -0.6$ mm and $f = 30$ GHz.

3.4.2 Discussion of DCIM

DCIM has been increasingly recognized as a very useful approach to tackle practical problems involved in multilayered structures. However, the crucial conflict in the DCIM is that the complex functions approximated by the GPOF represent spherical waves with complex distances, while the waves generated by a dipole in a multilayered medium usually include spherical, cylindrical and lateral waves. Hence, DCIM may provide an accurate and efficient approximation for most practical problems that are within the range of validity of the approach, which is usually on the order of a few wavelengths. Beyond this range, the accuracy of the closed-form representations of the Green's functions becomes very poor unless all other wave types except the spherical waves have been extracted and explicitly accounted for.

In general, the contribution of SWP's dominates in the far field, as SWP's have the

asymptotic behavior, $\frac{e^{-jk_{\rho p}\rho}}{\sqrt{\rho}}$, for large ρ. $k_{\rho p}$ is the SWP. For general multilayered media with strong SWP's contribution, the lack of the extraction often results in errors in the far-field region since the surface waves behave in the manner of cylindrical waves and it is physically inappropriate to approximate such waves by spherical waves. However, extracting the contribution of SWP's singularities is quite computationally intractable, since there is no analytical approach to finding the locations of SWP's except for simple geometries like single and double layers. On the other hand, due to the singularity of the Hankel function at the origin, the accuracy of the approximation with the extraction of SWP's may deteriorate in the near field region, as shown in Fig. 3.11. In order to guarantee the computational accuracy and efficiency, the extraction of contribution of the SWP's is only used beyond a switching distance from the source point. The switching distance is usually selected to be $\rho = 10.0/k_0$. The lateral wave is correlated with the branch point [139] at an interface of two materials. It behaves asymptotically like $\frac{e^{-jk_{br}\rho}}{\rho^2}$ [140, 30]. k_{br} refers to the branch point. The contribution of lateral waves can be picked up by the newly developed three-level DCIM [51]. The magnitudes of spectral-domain Green's functions are also significantly different for different choices of the sampling path, as the spectral-domain Green's functions are quite complex functions of k_ρ. Therefore, other major sources for the deterioration of the accuracy of DCIM are unsuitable sampling path and poor sampling frequency. The problem can be solved by changing the parameters of the approximation algorithm. Thus, the number of samples on each level of DCIM needs to be fixed to 1024 in order to adequately capture the spectral-domain Green's functions.

In summary, DCIM is an admittedly accurate and efficient method for calculating

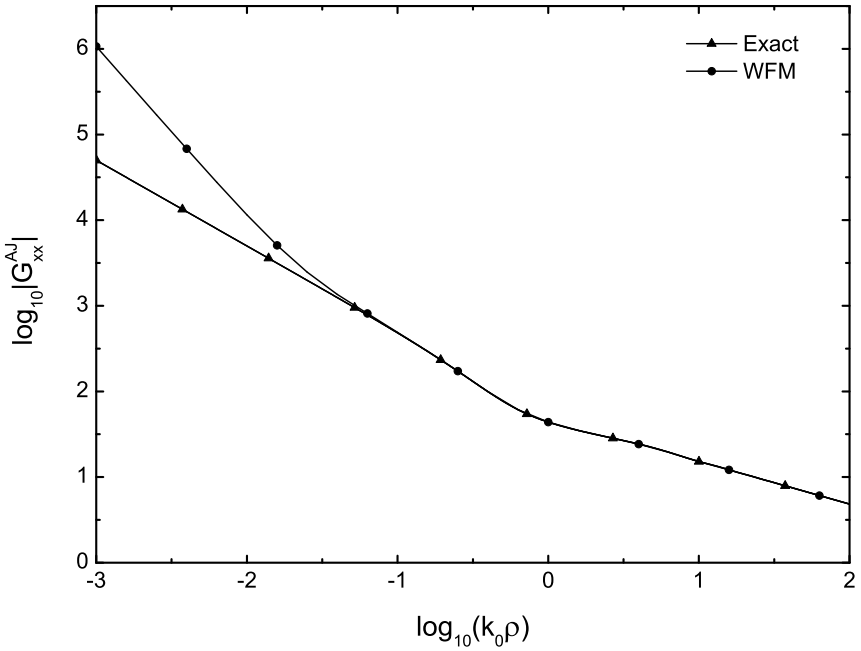

Figure 3.12: Magnitude Comparison of G_{xx}^{AJ} versus ρ for Fig. 3.3, where $m = n = 4$, $z' = z = -1.4$ mm and $f = 30$ GHz.

the DGF's in the multilayered medium for all the ranges of distance. Moreover, compared to WFM and MFHT method, DCIM is the only possible method to obtain accurate results in the far-field region.

3.4.3 Discussion of WFM

In view of the above numerical results, the accuracy of WFM is quite good for the general multilayered problems. Due to the inherent errors from the approximation algorithms, the deterioration of the accuracy of this method starts to be obvious when the numerical results are smaller than 10^{-5}, as seen in Fig. 3.4. Compared to the DCIM and MFHT method, the efficiency of WFM is the worst, which is due to two facts. Firstly, in view of (3.15)-(3.17), it can be seen that although the magnitudes of the spectral-domain window function in are fast decaying, the approximation function results in a complex

calculation process which requires six different integrals for each field point on the plots of numerical results. In addition, since the support size a of the window function is set as 10^{-4}, the precision requirement for calculating the six integrals in the approximation process is quite high. Therefore, the calculation of spatial-domain Green's function based on the approximation formulations is quite time-consuming. Moreover, due to the approximation algorithms, the accuracy of this method cannot be guaranteed when the source point is very close to the field point, as shown in Fig. 3.12.

Therefore, with a high precision requirement, the efficiency of the window function method may deteriorate significantly. Moreover, when the source and the observation points are very close to each other, this method is also not recommended. Compared to the DCIM and MFHT method, WFM may offer no obvious superiority on the accuracy and efficiency.

3.4.4 Discussion of MFHT method

Through the numerical experiments carried out above, it can be demonstrated that the MFHT method successfully extends the applicability of the traditional FHT method to general multilayered geometries and it is an attractive alternative to the rigorous, but computationally expensive numerical integration method. Nevertheless, the accuracy of this method deteriorates significantly when the horizontal distance between the source and observation points exceeds tens of wavelengths, as shown in Fig. 3.13. This deterioration is mainly attributed to the truncation error caused by the expansion algorithm and the inherent error from the filter coefficients. One remedy of improving the accuracy of

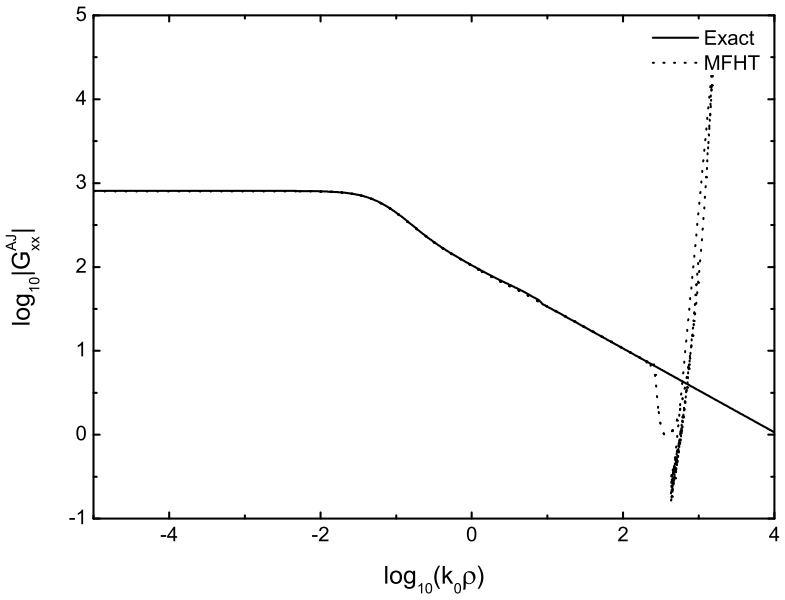

Figure 3.13: Magnitude Comparison of G_{xx}^{AJ} versus ρ for Fig. 3.3, where $m = n = 2$, $z' = -0.7$ mm, $z = -0.6$ mm and $f = 30$ GHz.

MFHT method in the far field is to apply the extrapolation method.

Compared to the DCIM and WFM, this method has the advantages of excellent accuracy and efficiency in the near and intermediate fields. More importantly, in the practical applications of multilayered medium, such as microstrip antennas requiring to change the vertical position of the feeding point or field point frequently, the MFHT method can be the most powerful tool for the calculation of the DGF's.

3.5 Conclusion

In this chapter, three popular methods for calculating multilayered Green's functions, i.e., the discrete complex image method, the window function method and the modified fast Hankel transform method, have been systematically studied to explain their compu-

tational theories and the selection criteria of crucial parameters. Then, for the first time, the robustness and efficiency of the three methods for the general multilayered problems have been carefully examined and compared through numerical examples. Finally, through making a comparison of the numerical results, we gave a critical discussion on the possible sources of errors and their remedies and comprehensive discussions on the advantages, restrictions and range of validity for the three fast methods. The DCIM has been shown to be powerful for calculating the DGF's in closed form for all the ranges of distance, but lack of reliable automated procedures for the complicated extraction of contribution of SWP's. WFM is also an alternative fast method for calculating the multilayered Green's functions. However, since the approximation process based on WFM requires six integral terms for calculating DGF's, the approximation is quite laborious and complicated. MFHT method has excellent performance in both accuracy and robustness, only for the near and intermediate fields. One major advantage of the studies in this chapter is that discussing the valid application range of DCIM, WFM and MFHT method both from mathematical and physical point of views has provided definite answers to the questions on their advantages and limitations. The comparison of accuracy and efficiency for the three fast methods may provide guidelines for the development of reliable computer-aided design tools.

Chapter 4

Fast Solution of Dyadic Green's Function for Multilayered Uniaxial Anisotropic Medium

4.1 Introduction

In previous chapters, attention has been restricted mainly to the multilayered isotropic media. Due to the emergence of practical applications of complex media in multilayered geometries [61, 62, 63, 64, 141, 142], of great practical interest is the case of accurate and expedient derivation of DGF's in the spectral domain and spatial domain for a multilayered anisotropic medium. Wait (1966) [143] studied the case of a horizontal dipole over a multilayered uniaxial anisotropic half-space. Then, Kong (1972) [144] solved the problem of dipoles over multilayered uniaxial anisotropic medium. In his formulae, the electromagnetic fields were resolved into transverse electric (TE) and transverse

magnetic (TM) waves. However, the location of the dipole sources was limited to the semi-infinite region above the multilayered medium. Using the same formulae, Tsang et al. (1975) [1] obtained the DGF's for sources over multilayered uniaxial anisotropic medium. The continued fraction expressions of global reflection and transmission coefficients rendered the derivation a cumbersome step for the case of many layers. Habashy et al. (1991) employed the *kDB* coordinate system and wave iterative technique to derive the spectral-domain Green's function in the planar multilayered gyrotropic medium [70]. However, one major disadvantage of the derivation process is that the vertical position of one interface related with the source layer has to be set to zero. This implies that, whenever the source position is changed, the whole coordinate system should be reset, which in turn will introduce particular complexity in the implementation of the numerical computation. Therefore, the theoretical formulations in [70] are not able to efficiently treat general multilayered problems with arbitrary positions of the source. This shortcoming motivated us to derive a complete and generalized set of the spectral-domain Green's function in the planar multilayered uniaxial anisotropic media, which was also the primary objective of this chapter. The key advantage of the present approach for deriving the DGF's for the multilayered uniaxial anisotropic medium over the previous work is that the systematic and holistic derivation could be stated in a language which may be handled by a computer in a straightforward way. This approach also may provide a promising tool to characterize the integrated microwave circuits and optical devices when uniaxial anisotropic materials are involved.

In this chapter, a fast solution for rigorously deriving and calculating DGF's for the planar multilayers of uniaxial media will be established based on MFHT method. The

kDB coordinate system is exploited and integrated with the wave iterative technique to obtain the spectral-domain Green's function. This algorithm relies on the accurate expressions of unbounded dyadic Green's function and scattered Green's function in uniaxial media, which can be classified into the ordinary and extraordinary waves. Then, the newly developed MFHT method is employed for the calculation of the DGF in the planar multilayered uniaxial anisotropic media. The validity of the algorithm thus developed and the efficiency of MFHT method will be verified through numerical examples. The spatial-domain Green's function will, for the first time, deal with the multilayered uniaxial anisotropic media, and more importantly, the influence of material's anisotropy upon the Green's function will be demonstrated.

4.2 Unbounded Dyadic Green's Function in Spectral Domain

In this section, we will derive the DGF for an unbounded uniaxial anisotropic medium. By using the *kDB* coordinate system and the Fourier transform method, the electric-field Green's function will be derived, and then, the electric and magnetic fields can be obtained for an arbitrarily distributed electric current source. A uniaxial anisotropic medium is characterized by scalar magnetic permeability μ and electric permittivity tensor $\overline{\overline{\epsilon}}$. When the optic axis of the uniaxial anisotropic medium is in the $\hat{z}$ direction,

the permittivity tensor is

$$\bar{\bar{\epsilon}} = \begin{bmatrix} \epsilon_t & 0 & 0 \\ 0 & \epsilon_t & 0 \\ 0 & 0 & \epsilon_z \end{bmatrix} \tag{4.1}$$

In the *xyz* coordinate system, the constitutive relations in the uniaxial anisotropic medium are

$$\mathbf{E} = \bar{\bar{\kappa}} \cdot \mathbf{D} \tag{4.2}$$

$$\mathbf{H} = \nu \mathbf{B} \tag{4.3}$$

where

$$\bar{\bar{\kappa}} = \bar{\bar{\epsilon}}^{-1} = \begin{bmatrix} \kappa & 0 & 0 \\ 0 & \kappa & 0 \\ 0 & 0 & \kappa_z \end{bmatrix} \tag{4.4}$$

$$\nu = \mu^{-1} \tag{4.5}$$

The term $\bar{\bar{\kappa}}$ is the impermittivity tensor and ν is the impermeability. It is known that there are two distinct characteristic waves, ordinary wave and extraordinary wave, for the uniaxial anisotropic medium [123]. Their dispersion relations are

$$\omega^2 = \nu\kappa k_z^2 + \nu\kappa k_s^2 \tag{4.6}$$

for the ordinary wave and

$$\omega^2 = \nu\kappa k_z^2 + \nu\kappa_z k_s^2 \tag{4.7}$$

for the extraordinary wave. The solutions to (4.6) and (4.7) include the roots $k_z = \pm k_{zo}$ and $k_z = \pm k_{ze}$, respectively. The subscripts o and e denote the ordinary wave and extraordinary wave respectively, and the subscripts u and d refer to the upward propagating wave and downward propagating wave respectively. By using the *kDB* system, the electric and magnetic fields in the *xyz* coordinate system can be represented as

$$\mathbf{E}(\mathbf{k}) = \overline{\overline{\kappa}} \cdot [D_1(\mathbf{k})\hat{h} - D_2(\mathbf{k})\hat{v}(k_z)] \tag{4.8}$$

$$\mathbf{H}(\mathbf{k}) = -\frac{\omega}{k}[D_2(\mathbf{k})\hat{h} + D_1(\mathbf{k})\hat{v}(k_z)] \tag{4.9}$$

where

$$\hat{h} = \frac{1}{k_s}(\hat{x}\,k_y - \hat{y}\,k_x) \tag{4.10}$$

$$\hat{v} = \frac{1}{k}(-k_z\,\hat{k}_s + k_s\,\hat{z}) \tag{4.11}$$

$$\hat{k}_s = \frac{1}{k_s}(\hat{x}\,k_x + \hat{y}\,k_y) \tag{4.12}$$

The notation $D_{1,2}$ represents the two components of $\mathbf{D}$ projected onto the *kDB* coordinator system. Considering the roots of the dispersion relations (4.6) and (4.7), we can write the characteristic field vectors as follows:

$$\mathbf{e}_{\alpha\beta}(\mathbf{k}_s) \equiv \mathbf{E}(\mathbf{k}_s, \pm k_{z\alpha}) = \overline{\overline{\kappa}} \cdot [D_{1\alpha}(\mathbf{k})\hat{h} - D_{2\alpha}(\mathbf{k})\hat{v}(\pm k_{z\alpha})] \tag{4.13}$$

$$\mathbf{h}_{\alpha\beta}(\mathbf{k}_s) \equiv \mathbf{H}(\mathbf{k}_s, \pm k_{z\alpha}) = -\frac{\omega}{k_\alpha}[D_{2\alpha}(\mathbf{k})\hat{h} + D_{1\alpha}(\mathbf{k})\hat{v}(\pm k_{z\alpha})] \tag{4.14}$$

where

$$k_\alpha^2 = k_s^2 + k_{z\alpha}^2 \tag{4.15}$$

and $\alpha = o, e$; $\beta = u, d$. In the Fourier spectral domain, the electric field $\mathbf{E}(\mathbf{k}_s; z\backslash z')$ $(z \neq z')$ can be expressed as a superposition of ordinary and extraordinary waves

$$\begin{aligned}\mathbf{E}(\mathbf{k}_s; z\backslash z') &= \frac{1}{(2\pi)^2}\int_{-\infty}^{\infty} e^{i\mathbf{k}_s\cdot(\mathbf{r}_s-\mathbf{r}_s')}\mathbf{E}(\mathbf{r},\mathbf{r}')d\mathbf{r}_s \\ &= A_{o\beta}(\mathbf{k}_s)\mathbf{e}_{o\beta}(\mathbf{k}_s)e^{\pm ik_{zo}(z-z')} + A_{e\beta}(\mathbf{k}_s)\mathbf{e}_{e\beta}(\mathbf{k}_s)e^{\pm ik_{ze}(z-z')}\end{aligned} \tag{4.16}$$

The primed and unprimed parameters correspond to the source and observation points, respectively. In this work, we assume that the electric current point source is arbitrarily oriented, which is expressed by

$$\mathbf{J}(\mathbf{r}) = \hat{a}\delta(\mathbf{r} - \mathbf{r}') \tag{4.17}$$

where $\hat{a}$ is an arbitrary unit vector. In order to obtain the unknown values of amplitudes $A_{\alpha\beta}(\mathbf{k}_s)$, we employ the spectral-domain wave equation to formulate the electric field.

$$\mathbf{L}(\mathbf{k}) \cdot \mathbf{E}(\mathbf{k}) = -i\omega\mu\mathbf{J}(\mathbf{k}_s, k_z) \tag{4.18}$$

where

$$\mathbf{J}(\mathbf{k}_s, k_z) = -\frac{1}{(2\pi)^3}\hat{a} \tag{4.19}$$

$\mathbf{L}(\mathbf{k})$ is the dyadic Helmholtz operator for the uniaxial anisotropic medium.

$$\mathbf{L}(\mathbf{k}) = k^2\mathbf{I} - \omega^2\mu\bar{\bar{\epsilon}} - \mathbf{kk} \tag{4.20}$$

After algebraic manipulations, (4.20) can be recast in the following form:

$$\begin{aligned}\mathbf{L}(\mathbf{k}) =& k_\alpha^2\mathbf{I} - \omega^2\mu\bar{\bar{\epsilon}} - \mathbf{k}_{\alpha\beta}\mathbf{k}_{\alpha\beta} + (k_z^2 - k_{z\alpha}^2)(\hat{h}\hat{h} + \hat{k}_s\hat{k}_s) - \\ & k_s[k_z - (\pm k_{z\alpha})](\hat{z}\hat{k}_s + \hat{k}_s\hat{z})\end{aligned} \tag{4.21}$$

By using the Fourier transform and (4.16), the expression of $\mathbf{E}(\mathbf{k})$ can be written as [70]

$$\begin{aligned}\mathbf{E}(\mathbf{k}) &= \frac{1}{2\pi}\int_{-\infty}^{\infty} e^{ik_z(z-z')}\mathbf{E}(\mathbf{k}_s; z\backslash z')dz \\ &= \frac{1}{2\pi i}\sum_{\alpha=o,e}\left[\frac{A_{\alpha u}}{k_z - k_{z\alpha}}\mathbf{e}_{\alpha u} - \frac{A_{\alpha d}}{k_z + k_{z\alpha}}\mathbf{e}_{\alpha d}\right]\end{aligned} \tag{4.22}$$

Substituting (4.21) and (4.22) into (4.18), we can obtain

$$\begin{aligned}&\frac{1}{2\pi i}\sum_{\alpha=o,e}\Big\{A_{\alpha u}\Big[(k_z + k_{z\alpha})(\hat{h}\hat{h} + \hat{k}_s\hat{k}_s) - k_s(\hat{z}\hat{k}_s + \hat{k}_s\hat{z})\Big]\cdot\mathbf{e}_{\alpha u} - \\ &\qquad A_{\alpha d}\Big[(k_z - k_{z\alpha})(\hat{h}\hat{h} + \hat{k}_s\hat{k}_s) - k_s(\hat{z}\hat{k}_s + \hat{k}_s\hat{z})\Big]\cdot\mathbf{e}_{\alpha d}\Big\} \\ &= -i\omega\mu\mathbf{J}(\mathbf{k}_s, k_z)\end{aligned} \tag{4.23}$$

The solutions to the four unknowns $A_{\alpha\beta}$ ($\alpha = o, e; \beta = u, d$) need four independent equations. Subsequently, we substitute $k_z = \pm k_{z\alpha}$ and premultiply (4.23) by the characteristic field vectors $\mathbf{e}_{\alpha'\beta'}$. Finally, we get four independent equations for the solutions of $A_{\alpha\beta}$. Considering the uncoupled relationship between the ordinary wave and

extraordinary wave, we write the four equations as

$$\mathbf{Q}_{uu} \cdot \mathbf{A}_u = -2\pi\omega\mu\, \mathbf{\Omega}_u \cdot \mathbf{S}_u \tag{4.24}$$

$$-\mathbf{Q}_{dd} \cdot \mathbf{A}_d = -2\pi\omega\mu\, \mathbf{\Omega}_d \cdot \mathbf{S}_d \tag{4.25}$$

where

$$\mathbf{Q}_{\beta\beta} = \begin{bmatrix} Q_{o\beta,o\beta} & 0 \\ 0 & Q_{e\beta,e\beta} \end{bmatrix} \tag{4.26}$$

$$\mathbf{A}_\beta = \begin{bmatrix} A_{o\beta} \\ A_{e\beta} \end{bmatrix} \tag{4.27}$$

$$\mathbf{\Omega}_\beta = \begin{bmatrix} \mathbf{e}_{o\beta} & 0 \\ 0 & \mathbf{e}_{e\beta} \end{bmatrix} \tag{4.28}$$

$$\mathbf{S}_\beta = \begin{bmatrix} -\mathbf{J}(\mathbf{k}_s, \pm k_{zo}) \\ -\mathbf{J}(\mathbf{k}_s, \pm k_{ze}) \end{bmatrix} \tag{4.29}$$

$$Q_{\alpha u,\alpha u} = -Q_{\alpha d,\alpha d} = 2k_{z\alpha}\mathbf{e}_{\alpha u} \cdot \mathbf{e}_{\alpha u} - \mathbf{e}_{\alpha u} \cdot (\hat{z}\mathbf{k}_{\alpha u} + \mathbf{k}_{\alpha u}\hat{z}) \cdot \mathbf{e}_{\alpha u} \tag{4.30}$$

Solving (4.24) and (4.25) yields

$$\mathbf{A}_\beta = -\pi\omega\mu\, \mathbf{M}_\beta \cdot \mathbf{\Omega}_\beta \cdot \mathbf{S}_\beta \tag{4.31}$$

with

$$\mathbf{M}_\beta = 2\mathbf{Q}_{\beta\beta}^{-1} = \begin{bmatrix} M_{o\beta,o\beta} & 0 \\ 0 & M_{e\beta,e\beta} \end{bmatrix} \tag{4.32}$$

Substituting (4.31) into (4.16) and casting it in a matrix form, we obtain

$$\mathbf{E}(\mathbf{k}_s; z\backslash z') = -\pi\omega\mu\mathbf{P}_\beta^t(z\backslash z') \cdot \mathbf{\Omega}_\beta \cdot \mathbf{M}_\beta \cdot \mathbf{\Omega}_\beta \cdot \mathbf{S}_\beta, \quad z \neq z' \tag{4.33}$$

where

$$\mathbf{P}_\beta(z\backslash z') = \begin{bmatrix} e^{\pm ik_{zo}(z-z')} \\ e^{\pm ik_{ze}(z-z')} \end{bmatrix} \tag{4.34}$$

Then, the electric field in the spatial domain is expressed by applying the inverse Fourier transform to $\mathbf{E}(\mathbf{k}_s; z\backslash z')$.

$$\mathbf{E}(\mathbf{r}, \mathbf{r}') = -\pi\omega\mu \int_{-\infty}^{\infty} e^{-i\mathbf{k}_s\cdot(\mathbf{r}_s-\mathbf{r}'_s)}\mathbf{P}_\beta^t(z\backslash z') \cdot \mathbf{\Omega}_\beta \cdot \mathbf{M}_\beta \cdot \mathbf{\Omega}_\beta \cdot \mathbf{S}_\beta \, d\mathbf{k}_s, \qquad \mathbf{r} \neq \mathbf{r}' \tag{4.35}$$

When $\mathbf{r} = \mathbf{r}'$, the above formulation for the electric field does not exhibit the proper singular behavior. This singular behavior can be captured from the asymptotic behavior of $\mathbf{E}(\mathbf{k})$ when $|k_z| \to \infty$, which is given by

$$\mathbf{E}(\mathbf{k}) \sim -\frac{1}{(2\pi)^3}\frac{1}{i\omega\hat{z} \cdot \overline{\overline{\epsilon}} \cdot \hat{z}}\hat{z}\hat{z} \cdot \hat{a}\delta(z - z'), \quad |k_z| \to \infty \tag{4.36}$$

Thus, the complete expression for the electric field in the unbounded uniaxial anisotropic

medium is represented by

$$\begin{aligned}\mathbf{E}(\mathbf{r},\mathbf{r}') = &-\frac{1}{i\omega\hat{z}\cdot\overline{\overline{\epsilon}}\cdot\hat{z}}\hat{z}\hat{z}\cdot\hat{a}\delta(\mathbf{r}-\mathbf{r}')- \\ &\pi\omega\mu\int_{-\infty}^{\infty} e^{-i\mathbf{k}_s\cdot(\mathbf{r}_s-\mathbf{r}'_s)}\mathbf{P}^t_\beta(z\backslash z')\cdot\mathbf{\Omega}_\beta\cdot\mathbf{M}_\beta\cdot\mathbf{\Omega}_\beta\cdot\mathbf{S}_\beta\, d\mathbf{k}_s\end{aligned} \tag{4.37}$$

Since the electric field in an unbounded medium relates the DGF to the current via

$$\mathbf{E}_n(\mathbf{r}) = \int_{V'} d\mathbf{r}'\overline{\mathbf{G}}_{nn}(\mathbf{r},\mathbf{r}')\cdot\mathbf{J}(\mathbf{r}') \tag{4.38}$$

the formulations of the DGF in the unbounded uniaxial anisotropic medium can be derived from (4.37) in the following explicit form.

for $z > z'$,

$$\begin{aligned}\overline{\mathbf{G}}(\mathbf{r},\mathbf{r}') = &-\frac{1}{i\omega\hat{z}\cdot\overline{\overline{\epsilon}}\cdot\hat{z}}\hat{z}\hat{z}\,\delta(\mathbf{r}-\mathbf{r}') - \frac{\omega\mu}{8\pi^2} \\ &\int_{-\infty}^{\infty} d\mathbf{k}_s e^{-i\mathbf{k}_s\cdot(\mathbf{r}_s-\mathbf{r}'_s)}\cdot\left[e^{-ik_{zo}(z-z')}\mathbf{e}_{ou}\mathbf{u}_{ou} + e^{-ik_{ze}(z-z')}\mathbf{e}_{eu}\mathbf{u}_{eu}\right]\end{aligned} \tag{4.39}$$

for $z < z'$,

$$\begin{aligned}\overline{\mathbf{G}}(\mathbf{r},\mathbf{r}') = &-\frac{1}{i\omega\hat{z}\cdot\overline{\overline{\epsilon}}\cdot\hat{z}}\hat{z}\hat{z}\,\delta(\mathbf{r}-\mathbf{r}') - \frac{\omega\mu}{8\pi^2} \\ &\int_{-\infty}^{\infty} d\mathbf{k}_s e^{-i\mathbf{k}_s\cdot(\mathbf{r}_s-\mathbf{r}'_s)}\cdot\left[e^{ik_{zo}(z-z')}\mathbf{e}_{od}\mathbf{u}_{od} + e^{ik_{ze}(z-z')}\mathbf{e}_{ed}\mathbf{u}_{ed}\right]\end{aligned} \tag{4.40}$$

where

$$\mathbf{u}_{o\beta} = M_{o\beta,o\beta}\,\mathbf{e}_{o\beta} \tag{4.41}$$

$$\mathbf{u}_{e\beta} = M_{e\beta,e\beta}\,\mathbf{e}_{e\beta} \tag{4.42}$$

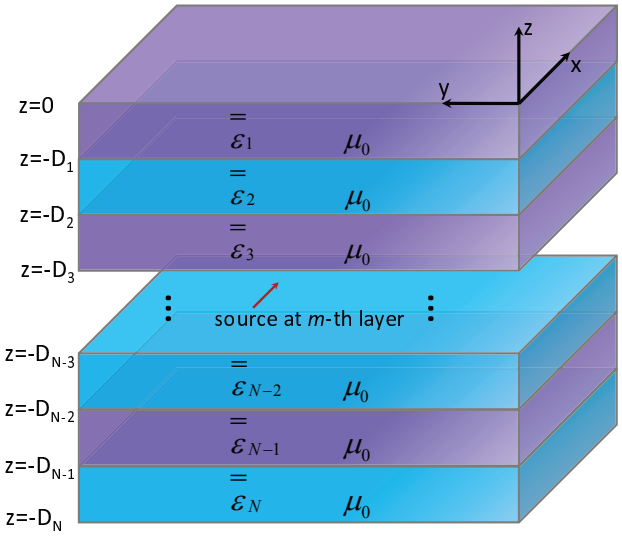

Figure 4.1: Geometry of the general planar multilayered uniaxial anisotropic medium.

4.3 Dyadic Green's Function for the Planar Multilayered Uniaxial Anisotropic Medium

In this section, based on the boundary condition and the WIT, the complete and generalized formulations of the spectral-domain Green's function in the planar multilayered uniaxial anisotropic media are explicitly expressed for three cases: viz., $m = n$, $m > n$ and $m < n$, where m and n denote the layers which the source point and observation point are located inside, respectively. The geometry of the general planar multilayered uniaxial anisotropic medium is depicted in Fig. 4.1.

4.3.1 Local Reflection and Transmission Matrices

To satisfy the boundary conditions of the continuity of the tangential electric and magnetic fields, the tangential components of $\mathbf{E}$ and $\mathbf{H}$ along the $\hat{h}$ and $\hat{k}_s$ directions are

matched at the interface of two layers.

$$\mathbf{X}_{\beta}^{(m)} + \mathbf{X}_{\overline{\beta}}^{(m)} \cdot \mathbf{R}_{m,n}^{(\beta)} = \mathbf{X}_{\beta}^{(n)} \cdot \mathbf{T}_{m,n}^{(\beta)} \tag{4.43}$$

$$\mathbf{Y}_{\beta}^{(m)} + \mathbf{Y}_{\overline{\beta}}^{(m)} \cdot \mathbf{R}_{m,n}^{(\beta)} = \mathbf{Y}_{\beta}^{(n)} \cdot \mathbf{T}_{m,n}^{(\beta)} \tag{4.44}$$

where $\mathbf{R}_{m,n}^{\beta}$ is the local reflection matrix and $\mathbf{T}_{m,n}^{\beta}$ is the local transmission matrix. The character $\beta = u$ ($\overline{\beta} = d$) for $m > n$ and $\beta = d$ ($\overline{\beta} = u$) for $m < n$.

$$\mathbf{R}_{m,n}^{\beta} = \begin{bmatrix} R_{mn}^{o} & 0 \\ 0 & R_{mn}^{e} \end{bmatrix} \tag{4.45}$$

$$\mathbf{T}_{m,n}^{\beta} = \begin{bmatrix} T_{mn}^{o} & 0 \\ 0 & T_{mn}^{e} \end{bmatrix} \tag{4.46}$$

$$\mathbf{X}_{\beta}^{(m)} = \begin{bmatrix} \hat{h} \cdot \mathbf{e}_{o\beta}^{(m)} & \hat{h} \cdot \mathbf{e}_{e\beta}^{(m)} \\ \hat{k}_s \cdot \mathbf{e}_{o\beta}^{(m)} & \hat{k}_s \cdot \mathbf{e}_{e\beta}^{(m)} \end{bmatrix} \tag{4.47}$$

$$\mathbf{Y}_{\beta}^{(m)} = \begin{bmatrix} \hat{h} \cdot \mathbf{h}_{o\beta}^{(m)} & \hat{h} \cdot \mathbf{h}_{e\beta}^{(m)} \\ \hat{k}_s \cdot \mathbf{h}_{o\beta}^{(m)} & \hat{k}_s \cdot \mathbf{h}_{e\beta}^{(m)} \end{bmatrix} \tag{4.48}$$

The term R_{mn}^{α} is the local reflection coefficient when the incident plane wave is in region m; T_{mn}^{α} is the local transmission coefficient from region m to region n.

Derived from the (4.43) and (4.44), the reflection and transmission matrices can be

expressed as

$$\mathbf{R}_{m,n}^{(\beta)} = \left[\mathbf{X}_{\overline{\beta}}^{(m)} - \mathbf{X}_{\beta}^{(n)} \cdot \{\mathbf{Y}_{\beta}^{(n)}\}^{-1} \cdot \mathbf{Y}_{\overline{\beta}}^{(m)}\right]^{-1} \cdot \left[-\mathbf{X}_{\beta}^{(m)} + \mathbf{X}_{\beta}^{(n)} \cdot \{\mathbf{Y}_{\beta}^{(n)}\}^{-1} \cdot \mathbf{Y}_{\beta}^{(m)}\right] \tag{4.49}$$

$$\mathbf{T}_{m,n}^{(\beta)} = \left[\mathbf{Y}_{\beta}^{(n)} - \mathbf{Y}_{\overline{\beta}}^{(m)} \cdot \{\mathbf{X}_{\overline{\beta}}^{(m)}\}^{-1} \cdot \mathbf{X}_{\beta}^{(n)}\right]^{-1} \cdot \left[\mathbf{Y}_{\beta}^{(m)} - \mathbf{Y}_{\overline{\beta}}^{(m)} \cdot \{\mathbf{X}_{\overline{\beta}}^{(m)}\}^{-1} \cdot \mathbf{X}_{\beta}^{(m)}\right] \tag{4.50}$$

4.3.2 Global Reflection and Transmission Matrices

Because of multiple reflections and cross-polarization effects, the electric field in an arbitrary layer n is represented in terms of upward propagating and downward propagating waves, as follows:

$$\begin{aligned}\mathbf{E}_n(z_n) \equiv \mathbf{E}(\mathbf{k}_s; z_n) =& f_n^o \mathbf{e}_{ou}^{(n)} e^{-ik_{zo}^{(n)} z_n} + f_n^e \mathbf{e}_{eu}^{(n)} e^{-ik_{ze}^{(n)} z_n} \\ &+ g_n^o \mathbf{e}_{od}^{(n)} e^{ik_{zo}^{(n)} z_n} + g_n^e \mathbf{e}_{ed}^{(n)} e^{ik_{ze}^{(n)} z_n}\end{aligned} \tag{4.51}$$

which can be cast in the following matrix form

$$\mathbf{E}_n(z_n) = \mathbf{G}_u^{(n)}(z_n) \cdot \mathbf{f}_n + \mathbf{G}_d^{(n)}(z_n) \cdot \mathbf{g}_n \tag{4.52}$$

where

$$\mathbf{G}_u^{(n)}(z_n) = \begin{bmatrix} e^{-ik_{zo}^{(n)} z_n} & 0 \\ 0 & e^{-ik_{ze}^{(n)} z_n} \end{bmatrix} \tag{4.53}$$

$$\mathbf{G}_d^{(n)}(z_n) = \begin{bmatrix} e^{ik_{zo}^{(n)} z_n} & 0 \\ 0 & e^{ik_{ze}^{(n)} z_n} \end{bmatrix} \tag{4.54}$$

$$\mathbf{f}_n = \begin{bmatrix} f_n^o \\ \\ f_n^e \end{bmatrix} \tag{4.55}$$

$$\mathbf{g}_n = \begin{bmatrix} g_n^o \\ \\ g_n^e \end{bmatrix} \tag{4.56}$$

The term $\mathbf{G}_u^{(n)}(z_n)$ represents the upward propagating wave expressed in the $[\mathbf{e}_{ou}^{(n)}, \mathbf{e}_{eu}^{(n)}]$ coordinate system. The first component on the diagonal of $\mathbf{G}_u^{(n)}(z_n)$ is along $\mathbf{e}_{ou}^{(n)}$ and the second component on the diagonal is along $\mathbf{e}_{eu}^{(n)}$. Similarly, $\mathbf{G}_d^{(n)}(z_n)$ represents the downward propagating wave expressed in the $[\mathbf{e}_{od}^{(n)}, \mathbf{e}_{ed}^{(n)}]$ coordinate system. In the layer $n-1$, the electric field vector is expressed by

$$\mathbf{E}_{n-1}(z_{n-1}) = \mathbf{G}_u^{(n-1)}(z_{n-1}) \cdot \mathbf{f}_{n-1} + \mathbf{G}_d^{(n-1)}(z_{n-1}) \cdot \mathbf{g}_{n-1} \tag{4.57}$$

At the interface of layer $n-1$ and layer n, the upward generalized reflection and transmission matrices are related with the fields by the following relationships:

$$\mathbf{G}_d^{(n)}(z_n = -D_{n-1}) \cdot \mathbf{g}_n = \mathbf{R}_{Un} \cdot \mathbf{G}_u^{(n)}(z_n = -D_{n-1}) \cdot \mathbf{f}_n \tag{4.58}$$

$$\mathbf{T}_{Un} \cdot \mathbf{G}_u^{(n)}(z_n = -D_{n-1}) \cdot \mathbf{f}_n = \mathbf{G}_u^{(n-1)}(z_{n-1} = -D_{n-1}) \cdot \mathbf{f}_{n-1} \tag{4.59}$$

where $\mathbf{R}_{Un}$ and $\mathbf{T}_{Un}$ are the generalized reflection matrix and generalized transmission matrix from layer n to layer $n-1$, respectively. It is noted that the downward propagating wave in the layer n is a consequence of the transmission of the downward propagating wave in the layer $n-1$ in combination with the reflection of the upward propagating

wave in the layer n. Thus, at the interface $z = -D_{n-1}$, the constraint condition is

$$\begin{aligned}\mathbf{R}_{Un}\cdot\mathbf{G}_u^{(n)}(z_n = -D_{n-1})\cdot\mathbf{f}_n &= \mathbf{R}_{n,n-1}^{(u)}\cdot\mathbf{G}_u^{(n)}(z_n = -D_{n-1})\cdot\mathbf{f}_n \\ &+\mathbf{T}_{n-1,n}^{d}\cdot\mathbf{G}_d^{(n-1)}(z_n = -D_{n-1})\cdot\mathbf{g}_{n-1}\end{aligned} \tag{4.60}$$

By using the expression of $\mathbf{g}_n$ from (4.58), we can write (4.60) as

$$\begin{aligned}\mathbf{R}_{Un}\cdot\mathbf{G}_u^{(n)}(z_n = -D_{n-1})\cdot\mathbf{f}_n &= \mathbf{R}_{n,n-1}^{(u)}\cdot\mathbf{G}_u^{(n)}(z_n = -D_{n-1})\cdot\mathbf{f}_n \\ &+\mathbf{T}_{n-1,n}^{d}\cdot\mathbf{G}_d^{(n-1)}(z_n = -D_{n-1})\cdot\mathbf{G}_d^{(n-1)}(z_{n-1} = -D_{n-2})^{-1} \\ &\cdot\mathbf{R}_{Un-1}\cdot\mathbf{G}_u^{(n-1)}(z_{n-1} = -D_{n-2})\cdot\mathbf{f}_{n-1}\end{aligned} \tag{4.61}$$

Next, we notice that the upward propagating wave in the layer $n-1$ is a superposition of the reflection of the downward propagating wave in the layer $n-1$ and the transmission of the upward propagating wave in the layer n. At the interface $z = -D_{n-1}$, we have the constraint condition

$$\begin{aligned}\mathbf{G}_u^{(n-1)}(z_{n-1} = -D_{n-1})\cdot\mathbf{f}_{n-1} &= \mathbf{T}_{n,n-1}^{(n)}\cdot\mathbf{G}_u^{(n)}(z_n = -D_{n-1})\cdot\mathbf{f}_n \\ &+\mathbf{R}_{n-1,n}^{(d)}\cdot\mathbf{G}_d^{(n-1)}(z_{n-1} = -D_{n-1})\cdot\mathbf{g}_{n-1}\end{aligned} \tag{4.62}$$

Substituting the expression of g_{n-1} from (4.58), we can write (4.62) as

$$\begin{aligned}\mathbf{G}_u^{(n-1)}(z_{n-1} = -D_{n-1})\cdot\mathbf{f}_{n-1} &= \mathbf{T}_{n,n-1}^{(n)}\cdot\mathbf{G}_u^{(n)}(z_n = -D_{n-1})\cdot\mathbf{f}_n \\ &+\mathbf{R}_{n-1,n}^{(d)}\cdot\mathbf{G}_d^{(n-1)}(z_{n-1} = -D_{n-1})\cdot\mathbf{G}_d^{(n-1)}(z_{n-1} = -D_{n-2})^{-1} \\ &\cdot\mathbf{R}_{Un-1}\cdot\mathbf{G}_u^{(n-1)}(z_{n-1} = -D_{n-2})\cdot\mathbf{f}_{n-1}\end{aligned} \tag{4.63}$$

From (4.61) and (4.63), we finally get the following recursive expression for the

upward generalized reflection matrix:

$$\begin{aligned}\mathbf{R}_{Un} =&\mathbf{R}^{(u)}_{n,n-1} + \mathbf{T}^{(d)}_{n-1,n} \cdot \mathbf{G}^{(n-1)}_{d}(z_{n-1} = -D_{n-1} + D_{n-2})\cdot \\ &\mathbf{R}_{Un-1} \cdot \mathbf{G}^{(n-1)}_{u}(z_{n-1} = -D_{n-2} + D_{n-1})\cdot \\ &\Big[\mathbf{I} - \mathbf{R}^{(d)}_{n-1,n} \cdot \mathbf{G}^{(n-1)}_{d}(z_{n-1} = -D_{n-1} + D_{n-2}) \cdot \mathbf{R}_{Un-1}\cdot \\ &\mathbf{G}^{(n-1)}_{u}(z_{n-1} = -D_{n-2} + D_{n-1})\Big]^{-1} \cdot \mathbf{T}^{(u)}_{n,n-1}\end{aligned} \tag{4.64}$$

Similarly, the recursive formulation of the downward generalized reflection matrix is derived as follows,

$$\begin{aligned}\mathbf{R}_{Dn} =&\mathbf{R}^{(d)}_{n,n+1} + \mathbf{T}^{(u)}_{n+1,n} \cdot \mathbf{G}^{(n+1)}_{u}(z_{n+1} = -D_{n} + D_{n+1})\cdot \\ &\mathbf{R}_{Dn+1} \cdot \mathbf{G}^{(n+1)}_{u}(z_{n+1} = -D_{n+1} + D_{n})\cdot \\ &\Big[\mathbf{I} - \mathbf{R}^{(u)}_{n+1,n} \cdot \mathbf{G}^{(n+1)}_{u}(z_{n+1} = -D_{n} + D_{n+1}) \cdot \mathbf{R}_{Dn+1}\cdot \\ &\mathbf{G}^{(n+1)}_{d}(z_{n+1} = -D_{n+1} + D_{n})\Big]^{-1} \cdot \mathbf{T}^{(d)}_{n,n+1}\end{aligned} \tag{4.65}$$

From (4.59) and (4.63), the recursive expression for the upward generalized transmission matrix is given by:

$$\begin{aligned}\mathbf{T}_{Un} = &\Big[\mathbf{I} - \mathbf{R}^{(d)}_{n-1,n} \cdot \mathbf{G}^{(n-1)}_{d}(z_{n-1} = -D_{n-1} + D_{n-2})\cdot \\ &\mathbf{R}_{Un-1} \cdot \mathbf{G}^{(n-1)}_{u}(z_{n-1} = -D_{n-2} + D_{n-1})\Big]^{-1} \cdot \mathbf{T}^{(u)}_{n,n-1}\end{aligned} \tag{4.66}$$

Similarly, the downward generalized transmission matrix can be expressed as:

$$\begin{aligned}\mathbf{T}_{Dn} = &\Big[\mathbf{I} - \mathbf{R}^{(u)}_{n+1,n} \cdot \mathbf{G}^{(n+1)}_{u}(z_{n+1} = -D_{n} + D_{n+1})\cdot \\ &\mathbf{R}_{Dn+1} \cdot \mathbf{G}^{(n+1)}_{d}(z_{n+1} = -D_{n+1} + D_{n})\Big]^{-1} \cdot \mathbf{T}^{(d)}_{n,n+1}\end{aligned} \tag{4.67}$$

4.3.3 Dyadic Green's Function for the Case $m = n$

For the case where the source and observation points are in the same layer n, based on the Fourier transform, the electric field can be expressed as

$$\mathbf{E}_n(\mathbf{r}) = \int_{-\infty}^{\infty} d\mathbf{k}_s e^{-i\mathbf{k}_s\cdot(\mathbf{r}_s-\mathbf{r}'_s)}\mathbf{E}_n(\mathbf{k}_s;z) \tag{4.68}$$

where

$$\mathbf{E}_n(\mathbf{k}_s;z) = e^{-ik_{zo}^{(n)}|z-z'|}\mathbf{e}_{o\beta}^{(n)}S_{o\beta}^{(n)} + e^{-ik_{ze}^{(n)}|z-z'|}\mathbf{e}_{e\beta}^{(n)}S_{e\beta}^{(n)} \tag{4.69}$$

$$S_{\alpha\beta}^{(n)} = \frac{\omega\mu_n}{8\pi^2}\,\mathbf{u}_{\alpha\beta}^{(n)}\cdot\hat{a} \tag{4.70}$$

Based on the equation (4.37), $\mathbf{E}_n(\mathbf{k}_s;z)$ can be cast as follows

$$\mathbf{E}_n(\mathbf{k}_s;z) = \mathbf{G}_\beta^{(n)}(z)\cdot\mathbf{G}_\beta^{(n)}(-z')\cdot\mathbf{S}_\beta^{(n)} \tag{4.71}$$

where

$$\mathbf{S}_\beta^{(n)} = \begin{bmatrix} S_o^{(n)} \\ \\ S_e^{(n)} \end{bmatrix} = \frac{\omega\mu_n}{8\pi^2}\begin{bmatrix} \mathbf{u}_{o\beta}^{(n)} \\ \\ \mathbf{u}_{e\beta}^{(n)} \end{bmatrix}\cdot\hat{a} \tag{4.72}$$

In an arbitrary layer n, the electric field is written as

$$\mathbf{E}_n(\mathbf{k}_s;z_n) = \mathbf{G}_\beta^{(n)}(z_n)\cdot\mathbf{G}_\beta^{(n)}(-z'_n)\cdot\mathbf{S}_\beta^{(n)} + \mathbf{G}_u^{(n)}(z_n)\cdot\mathbf{f}_n + \mathbf{G}_d^{(n)}(z_n)\cdot\mathbf{g}_n \tag{4.73}$$

where two unknown vectors, $\mathbf{f}_n$ and $\mathbf{g}_n$ need to be determined. For $z_n > z'_n$,

$$\mathbf{E}_n(\mathbf{k}_s;z_n) = \mathbf{G}_u^{(n)}(z_n)\cdot\left[\mathbf{G}_u^{(n)}(-z'_n)\cdot\mathbf{S}_u^{(n)} + \mathbf{f}_n\right] + \mathbf{G}_d^{(n)}(z_n)\cdot\mathbf{g}_n \tag{4.74}$$

where the first term represents waves propagating upward and the second term represents waves propagating downward. At the interface $z = -D_{n-1}$, the downward propagating waves are related to the upward propagating waves by the upward generalized reflection matrix.

$$\mathbf{g}_n = \mathbf{G}_d^{(n)^{-1}}(z_n = -D_{n-1}) \cdot \mathbf{R}_{Un} \cdot \mathbf{G}_u^{(n)}(z_n = -D_{n-1}) \cdot \left[\mathbf{G}_u^{(n)}(-z') \cdot \mathbf{S}_u^{(n)} + \mathbf{f}_n\right] \tag{4.75}$$

Similarly, for $z_n < z'_n$,

$$\mathbf{E}_n(\mathbf{k}_s; z_n) = \mathbf{G}_d^{(n)}(z_n) \cdot \left[\mathbf{G}_d^{(n)}(-z'_n) \cdot \mathbf{S}_d^{(n)} + \mathbf{g}_n\right] + \mathbf{G}_u^{(n)}(z_n) \cdot \mathbf{f}_n \tag{4.76}$$

$$\mathbf{f}_n = \mathbf{G}_u^{(n)^{-1}}(z_n = -D_n) \cdot \mathbf{R}_{Dn} \cdot \mathbf{G}_d^{(n)}(z_n = -D_n) \cdot \left[\mathbf{G}_d^{(n)}(-z') \cdot \mathbf{S}_d^{(n)} + \mathbf{g}_n\right] \tag{4.77}$$

Solving for $\mathbf{f}_n$ and $\mathbf{g}_n$ from (4.75) and (4.77), we obtain

$$\begin{aligned}\mathbf{g}_n = \mathbf{G}_d^{(n)^{-1}}&(z_n = -D_{n-1}) \cdot \mathbf{R}_{Un} \cdot \mathbf{M}_n \cdot \mathbf{G}_u^{(n)}(z_n = -D_{n-1}) \cdot \\ &\left[\mathbf{G}_u^{(n)}(-z') \cdot \mathbf{S}_u^{(n)} + \mathbf{G}_u^{(n)}(z_n = D_n) \cdot \mathbf{R}_{Dn} \cdot \right. \\ &\left. \mathbf{G}_d^{(n)}(z_n = -D_n) \cdot \mathbf{G}_d^{(n)}(-z') \cdot \mathbf{S}_d^{(n)}\right]\end{aligned} \tag{4.78}$$

$$\begin{aligned}\mathbf{f}_n = \mathbf{G}_u^{(n)^{-1}}&(z_n = -D_n) \cdot \mathbf{R}_{Dn} \cdot \mathbf{N}_n \cdot \mathbf{G}_d^{(n)}(z_n = -D_n) \cdot \\ &\left[\mathbf{G}_d^{(n)}(-z') \cdot \mathbf{S}_d^{(n)} + \mathbf{G}_d^{(n)}(z_n = D_{n-1}) \cdot \mathbf{R}_{Un} \cdot \right. \\ &\left. \mathbf{G}_u^{(n)}(z_n = -D_{n-1}) \cdot \mathbf{G}_u^{(n)}(-z') \cdot \mathbf{S}_u^{(n)}\right]\end{aligned} \tag{4.79}$$

where

$$\mathbf{M}_n = \left[\mathbf{I} - \mathbf{G}_u^{(n)}(z_n = -D_{n-1} + D_n) \cdot \mathbf{R}_{Dn} \cdot \mathbf{G}_d^{(n)}(z_n = -D_n + D_{n-1}) \cdot \mathbf{R}_{Un}\right]^{-1} \tag{4.80}$$

$$\mathbf{N}_n = \left[\mathbf{I} - \mathbf{G}_d^{(n)}(z_n = -D_n + D_{n-1}) \cdot \mathbf{R}_{Un} \cdot \mathbf{G}_u^{(n)}(z_n = -D_{n-1} + D_n) \cdot \mathbf{R}_{Dn}\right]^{-1} \tag{4.81}$$

Substituting (4.78) and (4.79) into (4.73), we get the following expression for the electric field.

$$\begin{aligned}
&\mathbf{E}_n(\mathbf{k}_s; z_n) = \mathbf{G}_\beta^{(n)}(z_n) \cdot \mathbf{G}_\beta^{(n)}(-z_n') \cdot \mathbf{S}_\beta^{(n)} + \\
&\mathbf{G}_u^{(n)}(z_n) \cdot \mathbf{G}_u^{(n)^{-1}}(z_n = -D_n) \cdot \mathbf{R}_{Dn} \cdot \mathbf{N}_n \cdot \mathbf{G}_d^{(n)}(z_n = -D_n) \cdot \\
&\Big[\mathbf{G}_d^{(n)}(-z') \cdot \mathbf{S}_d^{(n)} + \mathbf{G}_d^{(n)}(z_n = D_{n-1}) \cdot \mathbf{R}_{Un} \cdot \\
&\mathbf{G}_u^{(n)}(z_n = -D_{n-1}) \cdot \mathbf{G}_u^{(n)}(-z') \cdot \mathbf{S}_u^{(n)}\Big] + \\
&\mathbf{G}_d^{(n)}(z_n) \cdot \mathbf{G}_d^{(n)^{-1}}(z_n = -D_{n-1}) \cdot \mathbf{R}_{Un} \cdot \mathbf{M}_n \cdot \mathbf{G}_u^{(n)}(z_n = -D_{n-1}) \cdot \\
&\Big[\mathbf{G}_u^{(n)}(-z') \cdot \mathbf{S}_u^{(n)} + \mathbf{G}_u^{(n)}(z_n = D_n) \cdot \mathbf{R}_{Dn} \cdot \mathbf{G}_d^{(n)}(z_n = -D_n) \cdot \\
&\mathbf{G}_d^{(n)}(-z') \cdot \mathbf{S}_d^{(n)}\Big]
\end{aligned} \tag{4.82}$$

Here, $\beta = u$ for $z_n > z_n'$ and $\beta = d$ for $z_n < z_n'$. Based on (4.38) and (4.82), the DGF in the planar multilayered uniaxial anisotropic medium is given by the following expression

for the case of $m = n$

$$
\begin{aligned}
&\overline{\overline{G}}_{nn}(\mathbf{r},\mathbf{r}') = -\frac{1}{i\omega\hat{z}\cdot\overline{\overline{\epsilon}}_n\cdot\hat{z}}\hat{z}\hat{z}\delta(\mathbf{r}-\mathbf{r}') - \\
&\frac{\omega\mu_n}{4\pi}\int_0^\infty dk_\rho\, k_\rho\cdot J_0(k_\rho\rho)\cdot\Big[e^{-ik_{zo}^{(n)}|z_n-z_n'|}\mathbf{e}_{o\beta}^{(n)}\mathbf{u}_{o\beta}^{(n)} + \\
&e^{-ik_{ze}^{(n)}|z_n-z_n'|}\mathbf{e}_{e\beta}^{(n)}\mathbf{u}_{e\beta}^{(n)} + e^{-ik_{zo}^{(n)}(z_n-z_n')}A_1^{(1,1)}\mathbf{e}_{ou}^{(n)}\mathbf{u}_{ou}^{(n)} + \\
&e^{-ik_{zo}^{(n)}z_n-ik_{ze}^{(n)}z_n'}A_1^{(1,2)}\mathbf{e}_{ou}^{(n)}\mathbf{u}_{eu}^{(n)} + e^{-ik_{ze}^{(n)}z_n-ik_{zo}^{(n)}z_n'}A_1^{(2,1)}\mathbf{e}_{eu}^{(n)}\mathbf{u}_{ou}^{(n)} + \\
&e^{-ik_{ze}^{(n)}(z_n-z_n')}A_1^{(2,2)}\mathbf{e}_{eu}^{(n)}\mathbf{u}_{eu}^{(n)} + e^{-ik_{zo}^{(n)}(z_n+z_n')}A_2^{(1,1)}\mathbf{e}_{ou}^{(n)}\mathbf{u}_{od}^{(n)} + \\
&e^{-ik_{zo}^{(n)}z_n+ik_{ze}^{(n)}z_n'}A_2^{(1,2)}\mathbf{e}_{ou}^{(n)}\mathbf{u}_{ed}^{(n)} + e^{-ik_{ze}^{(n)}z_n+ik_{zo}^{(n)}z_n'}A_2^{(2,1)}\mathbf{e}_{eu}^{(n)}\mathbf{u}_{od}^{(n)} + \\
&e^{-ik_{ze}^{(n)}(z_n+z_n')}A_2^{(2,2)}\mathbf{e}_{eu}^{(n)}\mathbf{u}_{ed}^{(n)} + e^{ik_{zo}^{(n)}(z_n+z_n')}A_3^{(1,1)}\mathbf{e}_{od}^{(n)}\mathbf{u}_{ou}^{(n)} + \\
&e^{ik_{zo}^{(n)}z_n-ik_{ze}^{(n)}z_n'}A_3^{(1,2)}\mathbf{e}_{od}^{(n)}\mathbf{u}_{eu}^{(n)} + e^{ik_{ze}^{(n)}z_n-ik_{zo}^{(n)}z_n'}A_3^{(2,1)}\mathbf{e}_{ed}^{(n)}\mathbf{u}_{ou}^{(n)} + \\
&e^{ik_{ze}^{(n)}(z_n+z_n')}A_3^{(2,2)}\mathbf{e}_{ed}^{(n)}\mathbf{u}_{eu}^{(n)} + e^{ik_{zo}^{(n)}(z_n-z_n')}A_4^{(1,1)}\mathbf{e}_{od}^{(n)}\mathbf{u}_{od}^{(n)} + \\
&e^{ik_{zo}^{(n)}z_n+ik_{ze}^{(n)}z_n'}A_4^{(1,2)}\mathbf{e}_{od}^{(n)}\mathbf{u}_{ed}^{(n)} + e^{ik_{ze}^{(n)}z_n+ik_{zo}^{(n)}z_n'}A_4^{(2,1)}\mathbf{e}_{ed}^{(n)}\mathbf{u}_{od}^{(n)} + \\
&e^{ik_{ze}^{(n)}(z_n-z_n')}A_4^{(2,2)}\mathbf{e}_{ed}^{(n)}\mathbf{u}_{ed}^{(n)}\Big]
\end{aligned}
\tag{4.83}
$$

where

$$
\mathbf{A}_2 = [\mathbf{G}_u^{(n)}(z_n=-D_n)]^{-1}\cdot\mathbf{R}_{Dn}\cdot\mathbf{N}_n\cdot\mathbf{G}_d^{(n)}(z_n=-D_n) \tag{4.84}
$$

$$
\mathbf{A}_1 = \mathbf{A}_2\cdot\mathbf{G}_d^{(n)}(z_n=D_{n-1})\cdot\mathbf{R}_{Un}\cdot\mathbf{G}_u^{(n)}(z_n=-D_{n-1}) \tag{4.85}
$$

$$
\mathbf{A}_3 = [\mathbf{G}_d^{(n)}(z_n=-D_{n-1})]^{-1}\cdot\mathbf{R}_{Un}\cdot\mathbf{M}_n\cdot\mathbf{G}_u^{(n)}(z_n=-D_{n-1}) \tag{4.86}
$$

$$
\mathbf{A}_4 = \mathbf{A}_3\cdot\mathbf{G}_u^{(n)}(z_n=D_n)\cdot\mathbf{R}_{Dn}\cdot\mathbf{G}_d^{(n)}(z_n=-D_n) \tag{4.87}
$$

$$\mathbf{M}_n = [\mathbf{I} - \mathbf{G}_u^{(n)}(z_n = -D_{n-1} + D_n) \cdot \mathbf{R}_{Dn} \cdot \mathbf{G}_d^{(n)}(z_n = -D_n + D_{n-1}) \cdot \mathbf{R}_{Un}]^{-1} \tag{4.88}$$

$$\mathbf{N}_n = [\mathbf{I} - \mathbf{G}_d^{(n)}(z_n = -D_n + D_{n-1}) \cdot \mathbf{R}_{Un} \cdot \mathbf{G}_u^{(n)}(z_n = -D_{n-1} + D_n) \cdot \mathbf{R}_{Dn}]^{-1} \tag{4.89}$$

When the source point z' is located above the observation point z, β in (4.83) is equal to d. Otherwise, β is equal to u.

4.3.4 Dyadic Green's Function for the Case $m \neq n$

First, the case $m > n$ is considered. The source point is located inside the layer m and the observation point is located inside the layer n. The electric field in the layer m is expressed as

$$\begin{aligned}\mathbf{E}_m(\mathbf{k}_s; z_m) = \Big[&\mathbf{G}_u^m(z_m + D_{m-1}) + \mathbf{G}_d^{(m)}(z_m)\cdot \\ &\mathbf{G}_d^{(m)^{-1}}(z_m = -D_{m-1}) \cdot \mathbf{R}_{Um}\Big] \cdot \mathbf{e}^m(z'_m)\end{aligned} \tag{4.90}$$

where

$$\begin{aligned}\mathbf{e}^m(z'_m) = \mathbf{M}_m \cdot \mathbf{G}_u^{(m)}(z_m = -D_{m-1}) \cdot \Big[&\mathbf{G}_u^{(m)}(-z'_m) \cdot \mathbf{S}_u^{(m)} + \\ &\mathbf{G}_u^{(m)}(z_m = D_m) \cdot \mathbf{R}_{Dm} \cdot \mathbf{G}_d^{(m)}(z_m = -D_m - z'_m) \cdot \mathbf{S}_d^{(m)}\Big]\end{aligned} \tag{4.91}$$

In the layer $m-1$, the electric field can be represented as follows:

$$\mathbf{E}_{m-1}(\mathbf{k}_s; z_{m-1}) = \mathbf{G}_u^{m-1}(z_{m-1}) \cdot \mathbf{f}_{m-1} + \mathbf{G}_d^{(m-1)}(z_{m-1}) \cdot \mathbf{g}_{m-1} \tag{4.92}$$

At the interface $z = -D_{m-2}$, the downward propagating wave is related to the upward

propagating wave by the upward generalized reflection matrix $\mathbf{R}_{Um-1}$. This yields,

$$\mathbf{g}_{m-1} = \mathbf{G}_d^{(m-1)^{-1}}(z_{m-1} = -D_{m-2}) \cdot \mathbf{R}_{Um-1} \cdot \mathbf{G}_u^{(m-1)}(z_{m-1} = -D_{m-2}) \cdot \mathbf{f}_{m-1} \tag{4.93}$$

At the interface $z = -D_{m-1}$, the upward propagating wave in the layer $m-1$ is related to the upward propagating wave in the layer m by the upward generalized transmission matrix $\mathbf{T}_{Um}$. That is,

$$\mathbf{T}_{Um} \cdot \mathbf{G}_u^{(m)}(z_m = -D_{m-1}) \cdot \mathbf{e}^{(m)}(z'_m) = \mathbf{G}_u^{(m-1)}(z_{m-1} = -D_{m-1}) \cdot \mathbf{f}_{m-1} \tag{4.94}$$

which yields

$$\mathbf{f}_{m-1} = \mathbf{G}_u^{(m-1)^{-1}}(z_{m-1} = -D_{m-1}) \cdot \mathbf{T}_{Um} \cdot \mathbf{G}_u^{(m)}(z_m = -D_{m-1}) \cdot \mathbf{e}^{(m)}(z'_m) \tag{4.95}$$

Thus, the electric field in the layer $m-1$ is represented as

$$\begin{aligned} \mathbf{E}_{m-1}(\mathbf{k}_s; z_{m-1}) = \Big[& \mathbf{G}_u^{(m-1)}(z_{m-1}) + \mathbf{G}_d^{(m-1)}(z_{m-1}) \cdot \\ & \mathbf{G}_d^{(m-1)^{-1}}(z_{m-1} = -D_{m-2}) \cdot \mathbf{R}_{Um-1} \cdot \mathbf{G}_u^{(m-1)}(z_{m-1} = -D_{m-2}) \Big] \cdot \\ & \mathbf{G}_u^{(m-1)^{-1}}(z_{m-1} = -D_{m-1}) \cdot \mathbf{T}_{Um} \cdot \mathbf{G}_u^{(m)}(z_m = -D_{m-1}) \cdot \mathbf{e}^{m}(z'_m) \end{aligned} \tag{4.96}$$

Finally, the electric field in an arbitrary layer n above the source layer m is given by

$$\begin{aligned}\mathbf{E}_n(\mathbf{k}_s; z_n) = \Big[&\mathbf{G}_u^{(n)}(z_n) + \mathbf{G}_d^{(n)}(z_n) \cdot \mathbf{G}_d^{(n)^{-1}}(z_n = -D_{n-1}) \cdot \\ &\mathbf{R}_{Un} \cdot \mathbf{G}_u^{(n)}(z_n = -D_{n-1})\Big] \cdot \mathbf{G}_u^{(n)^{-1}}(z_n = -D_n) \cdot \mathbf{Y}_{m,n}^{(u)} \cdot \\ &\mathbf{G}_u^{(m)}(z_m = -D_{m-1}) \cdot \mathbf{e}^m(z'_m)\end{aligned} \tag{4.97}$$

where, $\mathbf{Y}_{m,n}^{(u)}$ is the generalized transmission matrix from the layer m to the layer n and its expression is given by

$$\begin{aligned}\mathbf{Y}_{m,n}^{(u)} = &\mathbf{T}_{Un+1} \cdot \mathbf{G}_u^{(n+1)}(z_{n+1} = -D_n + D_{n+1}) \cdot \mathbf{T}_{Un+2} \\ &\cdot \ldots \cdot \mathbf{G}_u^{(m-1)}(z_{m-1} = -D_{m-2} + D_{m-1}) \cdot \mathbf{T}_{Um}\end{aligned} \tag{4.98}$$

Hence, substituting the formulation of $\mathbf{e}^m(z'_m)$, we get the explicit expression of $\mathbf{E}_n(\mathbf{k}_s; z_n)$ for the case of $m > n$

$$\begin{aligned}\mathbf{E}_n(\mathbf{k}_s; z_n) = \Big[&\mathbf{G}_u^{(n)}(z_n + D_n) + \mathbf{G}_d^{(n)}(z_n + D_{n-1}) \cdot \mathbf{R}_{Un} \cdot \\ &\mathbf{G}_u^{(n)}(z_n = -D_{n-1} + D_n)\Big] \cdot \mathbf{Y}_{m,n}^{(u)} \cdot \mathbf{M}_m \cdot \\ \Big[&\mathbf{G}_u^{(m)}(z_m = -D_{m-1} - z'_m) \cdot \mathbf{S}_u^{(m)} + \mathbf{G}_u^{(m)}(z_m = -D_{m-1} + D_m) \cdot \\ &\mathbf{R}_{Dm} \cdot \mathbf{G}_d^{(m)}(z_m = -D_m - z'_m) \cdot \mathbf{S}_d^{(m)}\Big]\end{aligned} \tag{4.99}$$

From (4.99), it is easy to obtain an explicit expression for the DGF $\mathbf{G}_{nm}(\mathbf{r}, \mathbf{r}')$ for the case of $m > n$. This yields

$$\overline{\overline{G}}_{nm}(\mathbf{r},\mathbf{r}') = -\frac{\omega\mu_m}{4\pi}\int_0^\infty dk_\rho\, k_\rho \cdot J_0(k_\rho\rho)\cdot$$

$$\Big[e^{-ik_{zo}^{(n)}(z_n+D_n)-ik_{zo}^{(m)}(z'_m+D_{m-1})}B_1^{(1,1)}\mathbf{e}_{ou}^{(n)}\mathbf{u}_{ou}^{(m)} + e^{-ik_{zo}^{(n)}(z_n+D_n)-ik_{ze}^{(m)}(z'_m+D_{m-1})}B_1^{(1,2)}\mathbf{e}_{ou}^{(n)}\mathbf{u}_{eu}^{(m)}+$$

$$e^{-ik_{ze}^{(n)}(z_n+D_n)-ik_{zo}^{(m)}(z'_m+D_{m-1})}B_1^{(2,1)}\mathbf{e}_{eu}^{(n)}\mathbf{u}_{ou}^{(m)} + e^{-ik_{ze}^{(n)}(z_n+D_n)-ik_{ze}^{(m)}(z'_m+D_{m-1})}B_1^{(2,2)}\mathbf{e}_{eu}^{(n)}\mathbf{u}_{eu}^{(m)}+$$

$$e^{-ik_{zo}^{(n)}(z_n+D_n)+ik_{zo}^{(m)}(z'_m+D_m)}B_2^{(1,1)}\mathbf{e}_{ou}^{(n)}\mathbf{u}_{od}^{(m)} + e^{-ik_{zo}^{(n)}(z_n+D_n)+ik_{ze}^{(m)}(z'_m+D_m)}B_2^{(1,2)}\mathbf{e}_{ou}^{(n)}\mathbf{u}_{ed}^{(m)}+$$

$$e^{-ik_{ze}^{(n)}(z_n+D_n)+ik_{zo}^{(m)}(z'_m+D_m)}B_2^{(2,1)}\mathbf{e}_{eu}^{(n)}\mathbf{u}_{od}^{(m)} + e^{-ik_{ze}^{(n)}(z_n+D_n)+ik_{ze}^{(m)}(z'_m+D_m)}B_2^{(2,2)}\mathbf{e}_{eu}^{(n)}\mathbf{u}_{ed}^{(m)}+ \tag{4.100}$$

$$e^{ik_{zo}^{(n)}(z_n+D_{n+1})-ik_{zo}^{(m)}(z'_m+D_{m-1})}B_3^{(1,1)}\mathbf{e}_{od}^{(n)}\mathbf{u}_{ou}^{(m)} + e^{ik_{zo}^{(n)}(z_n+D_{n+1})-ik_{ze}^{(m)}(z'_m+D_{m-1})}B_3^{(1,2)}\mathbf{e}_{od}^{(n)}\mathbf{u}_{eu}^{(m)}+$$

$$e^{ik_{ze}^{(n)}(z_n+D_{n+1})-ik_{zo}^{(m)}(z'_m+D_{m-1})}B_3^{(2,1)}\mathbf{e}_{ed}^{(n)}\mathbf{u}_{ou}^{(m)} + e^{ik_{ze}^{(n)}(z_n+D_{n+1})-ik_{ze}^{(m)}(z'_m+D_{m-1})}B_3^{(2,2)}\mathbf{e}_{ed}^{(n)}\mathbf{u}_{eu}^{(m)}+$$

$$e^{ik_{zo}^{(n)}(z_n+D_{n+1})+ik_{zo}^{(m)}(z'_m+D_m)}B_4^{(1,1)}\mathbf{e}_{od}^{(n)}\mathbf{u}_{od}^{(m)} + e^{ik_{zo}^{(n)}(z_n+D_{n+1})+ik_{ze}^{(m)}(z'_m+D_m)}B_4^{(1,2)}\mathbf{e}_{od}^{(n)}\mathbf{u}_{ed}^{(m)}+$$

$$e^{ik_{ze}^{(n)}(z_n+D_{n+1})+ik_{zo}^{(m)}(z'_m+D_m)}B_4^{(2,1)}\mathbf{e}_{ed}^{(n)}\mathbf{u}_{od}^{(m)} + e^{ik_{ze}^{(n)}(z_n+D_{n+1})+ik_{ze}^{(m)}(z'_m+D_m)}B_4^{(2,2)}\mathbf{e}_{ed}^{(n)}\mathbf{u}_{ed}^{(m)}\Big]$$

where

$$\mathbf{B}_1 = \mathbf{Y}_{mn}^{(u)}\cdot\mathbf{M}_m \tag{4.101}$$

$$\mathbf{B}_2 = \mathbf{B}_1\cdot\mathbf{G}_u^{(m)}(z_m = -D_{m-1}+D_m)\cdot\mathbf{R}_{Dm} \tag{4.102}$$

$$\mathbf{B}_3 = \mathbf{R}_{Un}\cdot\mathbf{G}_u^{(n)}(z_n = -D_{n-1}+D_n)\cdot\mathbf{B}_1 \tag{4.103}$$

$$\mathbf{B}_4 = \mathbf{B}_3\cdot\mathbf{G}_u^{(m)}(z_m = -D_{m-1}+D_m)\cdot\mathbf{R}_{Dm} \tag{4.104}$$

For the case of $m < n$, following the same derivation process as employed earlier

for the case of $m > n$, we get the expression for the electric field in the layer n as follows

$$\begin{aligned}
&\mathbf{E}_n(\mathbf{k}_s; z_n) = \Big[\mathbf{G}_d^{(n)}(z_n + D_{n-1}) + \mathbf{G}_u^{(n)}(z_n + D_n) \cdot \mathbf{R}_{Dn} \cdot \\
&\mathbf{G}_d^{(n)}(z_n = -D_n + D_{n-1})\Big] \cdot \mathbf{Y}_{mn}^{(d)} \cdot \mathbf{N}_m \cdot \\
&\Big[\mathbf{G}_d^{(m)}(z_m = -D_m - z'_m) \cdot \mathbf{S}_d^{(m)} + \mathbf{G}_d^{(m)}(z_m = -D_m + D_{m-1}) \cdot \\
&\mathbf{R}_{Um} \cdot \mathbf{G}_u^{(m)}(z_m = -D_{m-1} - z'_m) \cdot \mathbf{S}_u^{(m)}\Big]
\end{aligned} \tag{4.105}$$

Thus, the explicit expression of the DGF for the case of $m < n$ is given by

$$\begin{aligned}
&\overline{\overline{G}}_{nm}(\mathbf{r}, \mathbf{r}') = -\frac{\omega\mu_m}{4\pi}\int_0^\infty dk_\rho\, k_\rho \cdot J_0(k_\rho\rho) \cdot \\
&\Big[e^{-ik_{zo}^{(n)}(z_n+D_n)-ik_{zo}^{(m)}(z'_m+D_{m-1})}C_1^{(1,1)}\mathbf{e}_{ou}^{(n)}\mathbf{u}_{ou}^{(m)} + e^{-ik_{zo}^{(n)}(z_n+D_n)-ik_{ze}^{(m)}(z'_m+D_{m-1})}C_1^{(1,2)}\mathbf{e}_{ou}^{(n)}\mathbf{u}_{eu}^{(m)} + \\
&e^{-ik_{ze}^{(n)}(z_n+D_n)-ik_{zo}^{(m)}(z'_m+D_{m-1})}C_1^{(2,1)}\mathbf{e}_{eu}^{(n)}\mathbf{u}_{ou}^{(m)} + e^{-ik_{ze}^{(n)}(z_n+D_n)-ik_{ze}^{(m)}(z'_m+D_{m-1})}C_1^{(2,2)}\mathbf{e}_{eu}^{(n)}\mathbf{u}_{eu}^{(m)} + \\
&e^{-ik_{zo}^{(n)}(z_n+D_n)+ik_{zo}^{(m)}(z'_m+D_m)}C_2^{(1,1)}\mathbf{e}_{ou}^{(n)}\mathbf{u}_{od}^{(m)} + e^{-ik_{zo}^{(n)}(z_n+D_n)+ik_{ze}^{(m)}(z'_m+D_m)}C_2^{(1,2)}\mathbf{e}_{ou}^{(n)}\mathbf{u}_{ed}^{(m)} + \\
&e^{-ik_{ze}^{(n)}(z_n+D_n)+ik_{zo}^{(m)}(z'_m+D_m)}C_2^{(2,1)}\mathbf{e}_{eu}^{(n)}\mathbf{u}_{od}^{(m)} + e^{-ik_{ze}^{(n)}(z_n+D_n)+ik_{ze}^{(m)}(z'_m+D_m)}C_2^{(2,2)}\mathbf{e}_{eu}^{(n)}\mathbf{u}_{ed}^{(m)} + \\
&e^{ik_{zo}^{(n)}(z_n+D_{n-1})-ik_{zo}^{(m)}(z'_m+D_{m-1})}C_3^{(1,1)}\mathbf{e}_{od}^{(n)}\mathbf{u}_{ou}^{(m)} + e^{ik_{zo}^{(n)}(z_n+D_{n-1})-ik_{ze}^{(m)}(z'_m+D_{m-1})}C_3^{(1,2)}\mathbf{e}_{od}^{(n)}\mathbf{u}_{eu}^{(m)} + \\
&e^{ik_{ze}^{(n)}(z_n+D_{n-1})-ik_{zo}^{(m)}(z'_m+D_{m-1})}C_3^{(2,1)}\mathbf{e}_{ed}^{(n)}\mathbf{u}_{ou}^{(m)} + e^{ik_{ze}^{(n)}(z_n+D_{n-1})-ik_{ze}^{(m)}(z'_m+D_{m-1})}C_3^{(2,2)}\mathbf{e}_{ed}^{(n)}\mathbf{u}_{eu}^{(m)} + \\
&e^{ik_{zo}^{(n)}(z_n+D_{n-1})+ik_{zo}^{(m)}(z'_m+D_m)}C_4^{(1,1)}\mathbf{e}_{od}^{(n)}\mathbf{u}_{od}^{(m)} + e^{ik_{zo}^{(n)}(z_n+D_{n-1})+ik_{ze}^{(m)}(z'_m+D_m)}C_4^{(1,2)}\mathbf{e}_{od}^{(n)}\mathbf{u}_{ed}^{(m)} + \\
&e^{ik_{ze}^{(n)}(z_n+D_{n-1})+ik_{zo}^{(m)}(z'_m+D_m)}C_4^{(2,1)}\mathbf{e}_{ed}^{(n)}\mathbf{u}_{od}^{(m)} + e^{ik_{ze}^{(n)}(z_n+D_{n-1})+ik_{ze}^{(m)}(z'_m+D_m)}C_4^{(2,2)}\mathbf{e}_{ed}^{(n)}\mathbf{u}_{ed}^{(m)}\Big]
\end{aligned} \tag{4.106}$$

where

$$\mathbf{C}_4 = \mathbf{Y}_{mn}^{(d)} \cdot \mathbf{N}_m \tag{4.107}$$

$$\mathbf{C}_3 = \mathbf{C}_4 \cdot \mathbf{G}_d^{(m)}(z_m = -D_m + D_{m-1}) \cdot \mathbf{R}_{Dm} \tag{4.108}$$

$$\mathbf{C}_2 = \mathbf{R}_{Dn} \cdot \mathbf{G}_d^{(n)}(z_n = -D_n + D_{n-1}) \cdot \mathbf{C}_4 \tag{4.109}$$

$$\mathbf{C}_1 = \mathbf{C}_2 \cdot \mathbf{G}_d^{(m)}(z_m = -D_m + D_{m-1}) \cdot \mathbf{R}_{Um} \tag{4.110}$$

A complete and generalized set of the DGF in the planar multilayered uniaxial anisotropic media has been derived in the spectral domain. The important point to note is that the formulations of Green's function are independent of the choice of the coordinate system. Hence, they are applicable to general multilayered structures without any accompanying requirement for coordinate change, which is the primary shortcoming in [70]. Similar expressions can be easily obtained for the DGF for the magnetic field $\mathbf{\Gamma}(\mathbf{r}, \mathbf{r}')$ due to an arbitrary oriented electric current point source and the DGF's for the electric field $\mathbf{G}_m(\mathbf{r}, \mathbf{r}')$ and the magnetic field $\mathbf{\Gamma}_\mathbf{m}(\mathbf{r}, \mathbf{r}')$ due to an arbitrary oriented magnetic current point source. From the three formulations (4.83)(4.100)(4.106), it is clearly shown that the DGF's in the spatial domain are expressed in terms of the cumbersome Sommerfeld integrals. To expedite the calculation of the Sommerfeld integrals, the newly developed MFHT method is employed to calculate the DGF's.

4.4 Numerical Results and Discussions

Various examples will be considered in this section in order to investigate the accuracy and efficiency of the proposed algorithm through the calculation of the DGF for the planar multilayered structure depicted in Fig. 4.2. The uppermost layer of the structure is taken to be free space while the lowermost layer is PEC. The operating frequency is

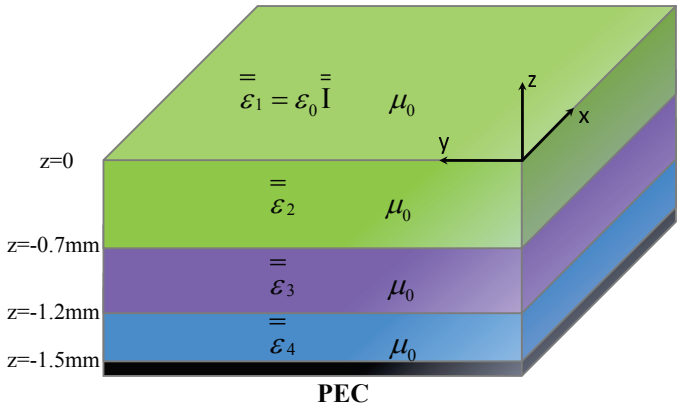

Figure 4.2: Geometry of a four-layer medium.

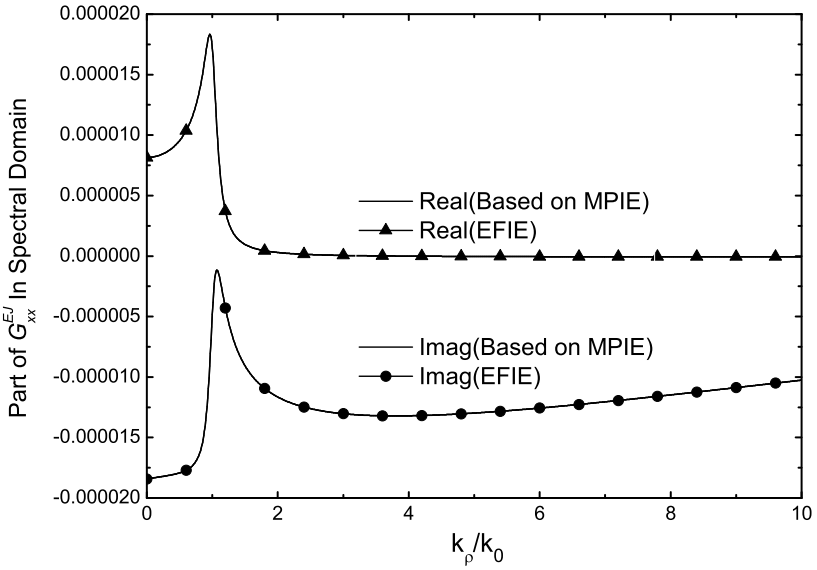

Figure 4.3: Magnitude of $\widetilde{G}_{xx}^{EJ}$ versus k_ρ for the four-layer isotropic medium with the following parameters: $z' = 0$ mm; $z = -1.2$ mm; layer 2: $\epsilon_2 = 2.1\epsilon_0$; layer 3: $\epsilon_3 = 9.8\epsilon_0$; layer 4: $\epsilon_4 = 8.6\epsilon_0$. The solid lines correspond to results obtained by the present algorithm while the dots correspond to results from MPIE.

3 GHz for all examples.

4.4.1 Comparison of Numerical Results in Spectral Domain

In the case of isotropic medium, it is known that the formulation of the correlation between the Green's function in the EFIE and that in the MPIE is given by

$$\overline{\overline{G}}^{EJ} = i\omega\mu_0\overline{\overline{G}}^{AJ} + \frac{1}{i\omega\epsilon_0}\nabla\nabla' G^{VJ} \tag{4.111}$$

It should be noted that the formulations of the DGF used in the MPIE have been well-documented [126]. Here, one element of the DGF obtained by the present algorithm is compared to the corresponding result from the Green's function used in the MPIE for a four-layer planar isotropic medium, as shown in Fig. 4.2. Fig. 4.3 depicts the spectrum of G_{xx}^{EJ} corresponding to Bessel function J_2. It is evident from the resultant plots that the spectral-domain Green's functions obtained by the proposed algorithm agree very well with the existing results from the MPIE when reduced to the isotropic case. The accuracy of the DGF in the spectral domain has been validated.

4.4.2 Comparison of Numerical Results in Spatial Domain

The MFHT method is employed for the approximation of the spatial-domain Green's functions for a four-layer planar uniaxial anisotropic medium, as shown in Fig. 4.2. Fig. 4.4 depicts the magnitude of the element G_{xx}^{EJ} of the DGF. In the three cases of Fig. 4.4, the following parameters are kept unchanged, $\epsilon_t^{(2)} = 2.1\epsilon_0$, $\epsilon_t^{(3)} = 9.8\epsilon_0$ and $\epsilon_t^{(4)} = 8.6\epsilon_0$. The parameters that are changed for the three cases are as follows. In the first case, $m = n = 2$, $z' = -0.7\,mm$, $z = -0.1\,mm$, and $\epsilon_z^{(2,3,4)}/\epsilon_t^{(2,3,4)} = 1.1$. In the second case,

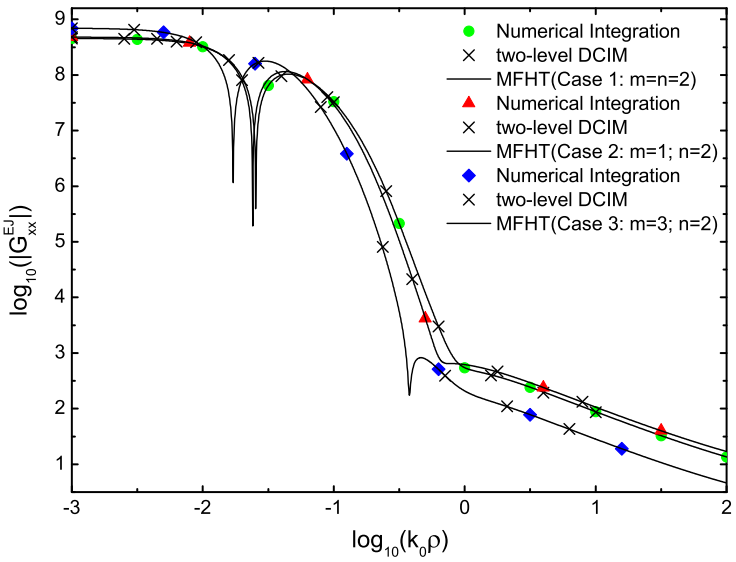

Figure 4.4: Magnitudes of G_{xx}^{EJ} versus ρ for the four-layer structure with the following parameters: Case 1: $z' = -0.7$ mm, $z = -0.1$ mm, $\epsilon_z^{(2,3,4)}/\epsilon_t^{(2,3,4)} = 1.1$; Case 2: $z' = 0$ mm, $z = -0.7$ mm, $\epsilon_z^{(2,3,4)}/\epsilon_t^{(2,3,4)} = 1.5$; Case 3: $z' = -1.2$ mm, $z = -0.6$ mm, $\epsilon_z^{(2,3,4)}/\epsilon_t^{(2,3,4)} = 2.0$. The solid lines correspond to results obtained by the MFHT method while the dots correspond to results obtained by the numerical integration and DCIM.

Table 4.1: Comparison of the CPU Time for Computing Dyadic Green's Function in Space Domain (based on Intel Duo Core2, 2.8GHz PC running Fortran)

Example	**DNI** sec./per point	**DCIM** sec.	**MFHT** sec.	**MFHT** sec./per point
Case 1 in Fig.4.4	179.02	116.14	46.72	0.875
Case 2 in Fig.4.4	413.68	122.30	106.89	1.312
Case 3 in Fig.4.4	413.20	137.13	106.70	1.407
200 Different Cases*	$\approx 80,000$	$\approx 20,000$	-	≈ 300

* Without loss of the generality, 200 different numerical experiments are conducted. The vertical position of the observation point is changed for 200 times, while the position of the source point is fixed.

$m = 1$, $n = 2$, $z' = 0$ mm, $z = -0.7$ mm, and $\epsilon_z^{(2,3,4)}/\epsilon_t^{(2,3,4)} = 1.5$. In the third case, $m = 3$, $n = 2$, $z' = -1.2$ mm, $z = -0.6$ mm, and $\epsilon_z^{(2,3,4)}/\epsilon_t^{(2,3,4)} = 2.0$. The solid lines represent the results obtained by the MFHT method, while the reference results obtained by numerical integration are represented by the discrete points in the plots. The DCIM-based numerical results are represented by the symbol $\times$. Clearly, the MFHT-based results are in excellent agreement with the numerical integration results and DCIM-based results. The results appear to confirm that based on the MFHT method, the DGF for the planar multilayered uniaxial anisotropic medium can be calculated accurately .

Table 4.1 shows the computational time for calculating the DGF based on the direct numerical integration (DNI), two-level DCIM and MFHT technique, respectively. We have used the same 2.8GHz PC to run all these numerical experiments (based on FORTRAN). Compared with the computational time taken by DNI, the time of MFHT method listed in the fifth line of Table 4.1 is very short for calculating the Green's function at one observation point. Fig. 4.4 shows there is excellent agreement between the results of DNI and that of MFHT method. From the comparison of accuracy and efficiency between the two methods, it can be deduced that MFHT method could be an attractive alternative to the rigorous, but computationally expensive DNI technique. The third and fourth lines in Table 4.1 show the computational times for the three cases in Fig. 4.4, based on the two-level DCIM and MFHT method respectively. It is observed that the MFHT method requires less time than DCIM for the three experiments. Here, in order to adequately sample the spectrum of Green's function, the number of sampling points on each level of DCIM is 1024. 1024 is one of the best choices for the accuracy of GPOF technique, which is used in the DCIM method. The maximum relative trun-

cation error of the MFHT method is set to be 10^{-7}, in order to obtain accurate results in a wide field area. With similar accuracy criteria, it seems that the MFHT method performs better than DCIM in terms of efficiency. Moreover, it is worth mentioning that the forms of the numerical results calculated by the DCIM and MFHT are totally different. The closed-form Green's function is obtained by the DCIM, while MFHT method is employed to compute the Green's function on discrete points. Table 4.1 also lists the computational time for two hundred different numerical experiments, based on the two-level DCIM and MFHT method. In two hundred experiments, the position of source point is fixed and the vertical position of observation point changes. It is clearly demonstrated that the closed-form Green's function obtained by DCIM offers no apparent superiority and the computational efficiency of MFHT method is almost 65 times higher than that of DCIM. In the practical applications of multilayered medium, such as microstrip antenna, when the vertical position of the feeding point or field point needs to be changed frequently, the MFHT method can be a powerful tool for the calculation of the multilayered Green's functions.

4.4.3 Influence of Material Anisotropy

For the final example considered in this chapter, we seek to examine another aspect of the proposed algorithm's accuracy as well as to investigate the influence of material anisotropy on the DGF. The accuracy of this algorithm has not been sufficiently validated since the closed-form Green's functions used in the EFIE in the planar multilayered uniaxial anisotropic media have not been derived so far. However, we can validate

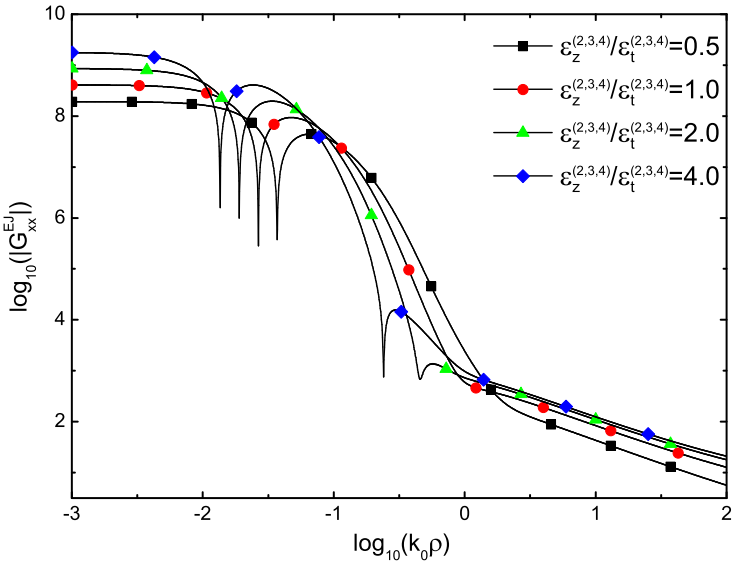

Figure 4.5: Magnitudes of G_{xx}^{EJ} versus ρ for the four-layer structure with the following parameters: m=n=2; $z' = -0.7$ mm; $z = -0.1$ mm; layer 2: $\epsilon_t^{(2)} = 2.1\epsilon_0$; layer 3: $\epsilon_t^{(3)} = 9.8\epsilon_0$; layer 4: $\epsilon_t^{(4)} = 8.6\epsilon_0$; $\epsilon_z^{(2,3,4)}/\epsilon_t^{(2,3,4)} = 0.5/1.0/2.0/4.0$.

the accuracy implicitly through numerical examples. Fig. 4.5 shows the magnitude of G_{xx}^{EJ} with $z' = -0.7\,mm$ and $z = -0.1\,mm$. Fig. 4.6 shows the magnitude of G_{zz}^{EJ} with $z' = 0\,mm$ and $z = -1.2\,mm$ and Fig. 4.7 shows the magnitude of G_{xz}^{EJ} with $z' = -1.2\,mm$ and $z = -0.1\,mm$. For the three figures, $\epsilon_t^{(2)} = 2.1\epsilon_0$, $\epsilon_t^{(3)} = 9.8\epsilon_0$, $\epsilon_t^{(4)} = 8.6\epsilon_0$ and $\epsilon_z^{(2,3,4)}/\epsilon_t^{(2,3,4)} = 0.5/1.0/2.0/4.0$. Clearly, the closer the value of ϵ_z/ϵ_t is progressively decreased to 1.0, the closer the magnitudes of the DGF are to the results for the case where $\epsilon_z/\epsilon_t = 1.0$. Note that the results of the field Green's functions corresponding to $\epsilon_z/\epsilon_t = 1.0$ are accurate since the accuracy of the spectral-domain Green's functions reduced to the isotropic case have been validated earlier. This serves as an indication that the presented algorithm for deriving the DGF is correct. Fig. 4.8 and Fig. 4.9 depict the three-dimensional magnitudes of G_{xx}^{EJ} and G_{xz}^{EJ} respectively, with $\epsilon_t^{(2)} = 2.1\epsilon_0$,

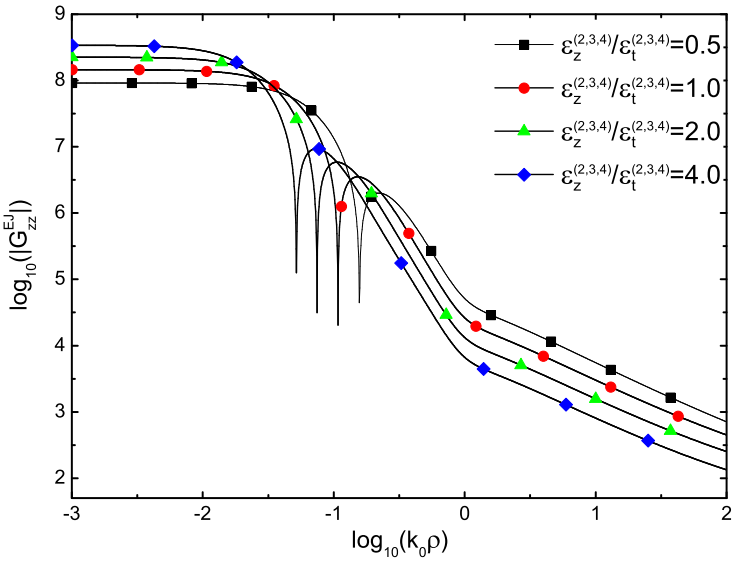

Figure 4.6: Magnitudes of G_{zz}^{EJ} versus ρ for the four-layer structure with the following parameters: m=1; n=3; $z' = 0$ mm; $z = -1.2$ mm; layer 2: $\epsilon_t^{(2)} = 2.1\epsilon_0$; layer 3: $\epsilon_t^{(3)} = 9.8\epsilon_0$; layer 4: $\epsilon_t^{(4)} = 8.6\epsilon_0$; $\epsilon_z^{(2,3,4)}/\epsilon_t^{(2,3,4)} = 0.5/1.0/2.0/4.0$.

$\epsilon_z^{(2)} = 2\epsilon_t^{(2)}$, $\epsilon_t^{(3)} = 9.8\epsilon_0$, $(\epsilon_z^{(3)} - \epsilon_t^{(3)})/\epsilon_0 = -9.0 \sim 9.0$, $\epsilon_t^{(4)} = 8.6\epsilon_0$ and $\epsilon_z^{(4)} = 2\epsilon_t^{(4)}$. The two plots clearly show the influence of material anisotropy on the Green's functions. It is noted that, as the value of $(\epsilon_z^{(3)} - \epsilon_t^{(3)})$ increases, the values of the DGF increase in the near field, and decrease in the intermediate field and far field. This implies that in the multilayered medium, the value of electric field increases in the near field and decreases in the intermediate field and far field as the material anisotropy increases. The investigation of the material anisotropy's characteristic can pave the way for the practical application of multilayered uniaxial anisotropic media.

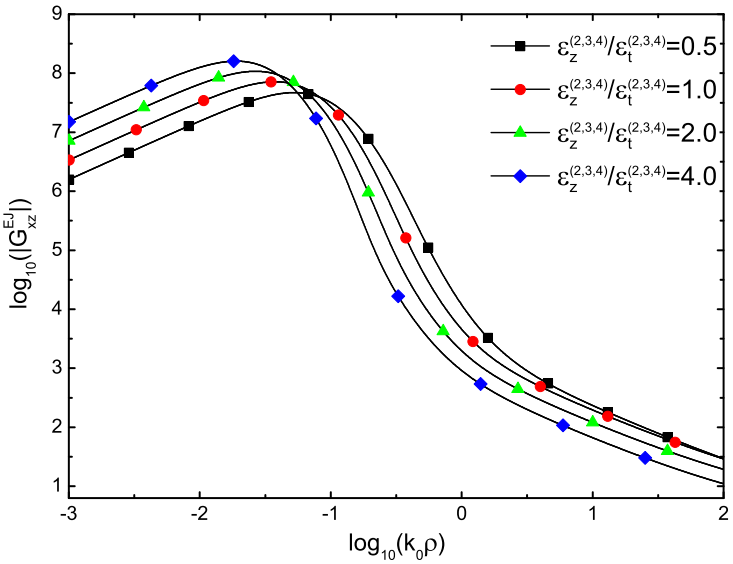

Figure 4.7: Magnitudes of G_{xz}^{EJ} versus ρ for the four-layer structure with the following parameters: m=3; n=2; $z' = -1.2$ mm; $z = -0.1$ mm; layer 2: $\epsilon_t^{(2)} = 2.1\epsilon_0$; layer 3: $\epsilon_t^{(3)} = 9.8\epsilon_0$; layer 4: $\epsilon_t^{(4)} = 8.6\epsilon_0$; $\epsilon_z^{(2,3,4)}/\epsilon_t^{(2,3,4)} = 0.5/1.0/2.0/4.0$.

4.5 Conclusion

In this chapter, a systematic and fast algorithm has been presented for the rigorous determination of the DGF's in the planar multilayered uniaxial anisotropic media. This algorithm employs the *kDB* coordinate system to obtain the characteristic field vectors and uses Fourier transform to derive the unbounded Green's function. One important contribution of the proposed algorithm is that a complete and generalized set of the spectral-domain Green's function in the planar multilayered uniaxial anisotropic media has been derived. Based on the MFHT method, the fast solutions of spatial-domain Green's function are obtained for the multilayered uniaxial anisotropic media. The MFHT technique has been introduced and its excellent efficiency has been numerically demonstrated. To validate the proposed algorithm and the accuracy of the DGF, the numerical examples

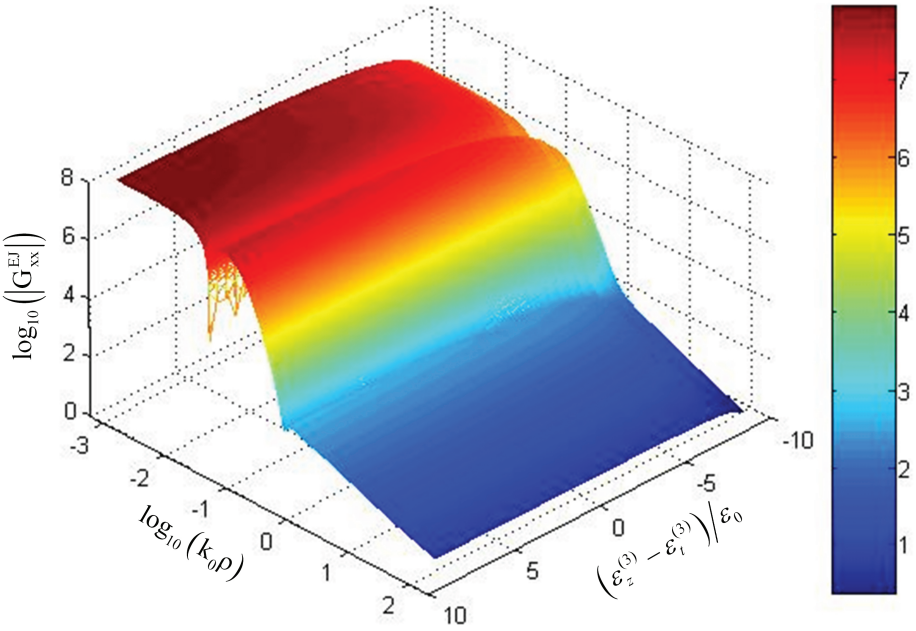

Figure 4.8: Three-dimensional magnitudes of G_{xx}^{EJ} versus ρ and permittivity tensor for the four-layer structure with the following parameters: m=1; n=3; $z' = 0$ mm; $z = -1.2$ mm; layer 2: $\epsilon_t^{(2)} = 2.1\epsilon_0$, $\epsilon_z^{(2)} = 2\epsilon_t^{(2)}$; layer 3: $\epsilon_t^{(3)} = 9.8\epsilon_0$, $(\epsilon_z^{(3)} - \epsilon_t^{(3)})/\epsilon_0 = -9.0 \sim 9.0$; layer 4: $\epsilon_t^{(4)} = 8.6\epsilon_0$, $\epsilon_z^{(4)} = 2\epsilon_t^{(4)}$.

are implemented in both the spectral domain and spatial domain. The numerical results have been shown to be very accurate and computationally efficient. It paves the path for modeling emerging microwave and optical devices involving composite birefringent materials.

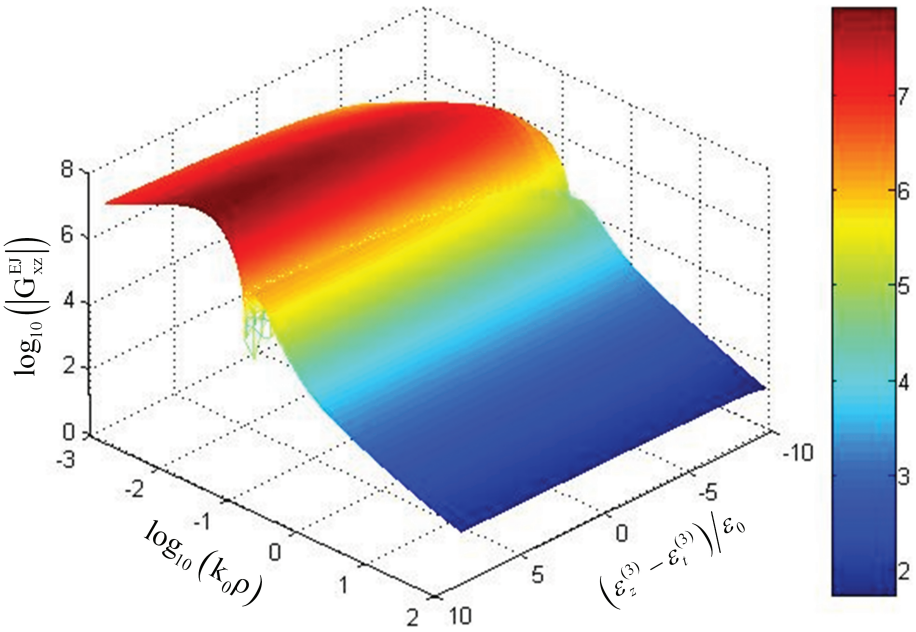

Figure 4.9: Three-dimensional magnitudes of G_{xz}^{EJ} versus ρ and permittivity tensor for the four-layer structure with the following parameters: m=1; n=3; $z' = 0$ mm; $z = -1.2$ mm; layer 2: $\epsilon_t^{(2)} = 2.1\epsilon_0$, $\epsilon_z^{(2)} = 2\epsilon_t^{(2)}$; layer 3: $\epsilon_t^{(3)} = 9.8\epsilon_0$, $(\epsilon_z^{(3)} - \epsilon_t^{(3)})/\epsilon_0 = -9.0 \sim 9.0$; layer 4: $\epsilon_t^{(4)} = 8.6\epsilon_0$, $\epsilon_z^{(4)} = 2\epsilon_t^{(4)}$.

Chapter 5

Fast Solution of Dyadic Green's Function for Multilayered Gyrotropic Medium

5.1 Introduction

Besides the application range of MMIC and microwave antennas, anisotropic materials have been found to have important applications in optical devices and radar absorbing materials [18, 56, 57, 58, 59, 60]. Due to the practical applications of anisotropic materials in multilayered geometries [61, 62, 63, 64, 65], the accurate and expedient calculation of the multilayered Green's function in both the spectral and spatial domains is highly necessary and important as a characterization tool. In this chapter, we will consider the material with a permittivity tensor and a permeability scalar, which refers to the gyrotropic medium.

In a homogeneous, gyrotropic medium, there exist two types of waves, type I and type II, which are generally decoupled in a homogeneous medium. However, in the presence of a planar interface, the two types of waves are coupled to each other at the interface. A type I wave or a type II wave may generate transmitted and reflected waves of type I and type II. Thus, the reflection and transmission coefficients needs to be represented by matrices in the gyrotropic medium. This characteristic is totally different from that of a homogeneous and isotropic medium where the two types of waves, TE and TM, are still decoupled at the interface. Hence, the problem of waves in multilayered gyrotropic media has to be regarded as a vector field problem, instead of a scalar problem. Although the derivation of the spectral-domain Green's functions for a multilayered gyrotropic medium can be traced back to an early time, the existing studies are still subject to considerable simplification which makes its application uncertain. Therefore, there is still room for the development and improvement of the deriving algorithm to develop a holistic and customizable formulations of spectral-domain Green's functions.

Besides, previous work only deals with the formulations of spectral-domain Green's functions for multilayered anisotropic media. The accuracy of the DGF's in the spectral domain has not been validated through numerical examples. Moreover, previous work has not presented a comprehensive discussion on the numerical results of the spatial-domain Green's function for a multilayered gyrotropic medium so far. Thus, another major aim of this research work is to systematically derive the spectral-domain Green's functions for the multilayered gyrotropic media, prove the effectiveness of spectral-domain Green's functions, calculate the spatial-domain Green's functions for

the multilayered gyrotropic medium, and more importantly, to investigate the influence of material's anisotropy upon the DGF's. This study may be valuable to enhance the understanding of electromagnetic properties in the gyrotropic media.

The final study reported in the thesis is aimed at rigorously deriving and calculating DGF's for the planar multilayered gyrotropic media based on the fast method. The *kDB* coordinate system associated with the wave iterative technique is employed to derive the spectral-domain Green's function. This algorithm is mainly dependent on the accurate derivation of unbounded DGF and scattered Green's function in the gyrotropic media, which can be classified into the type I wave and type II wave. Then, the newly developed MFHT method is used for the calculation of the DGF in the planar multilayered gyrotropic media. Although the main idea of the derivation procedure is similar to the case of uniaxial anisotropic medium, the coupling behavior of characteristic waves results in the totally different formulation of unbounded Green's function and the introduction of off-diagonal elements for reflection and transmission coefficients makes the derivation process more complicated. To gain insight into the DGF's in the multilayered gyrotropic medium, numerical experiments are carried out to determine the accuracy of spectral-domain Green's functions derived by the newly developed deriving algorithm. Then, the spatial-domain Green's functions are, for the first time, calculated by the fast method. More importantly, we explore the influence of material's anisotropy on the Green's functions.

5.2 Spectral-domain Green's Function for Gyrotropic Medium

In this chapter, similarly to what we did in the previous chapter, with the use of the *kDB* coordinate system and WIT, we will focus on the derivation of spectral-domain Green's function for the multilayered gyrotropic medium, gaining in simplicity without losing the property in generality.

5.3 Unbounded Dyadic Green's Function for Gyrotropic Medium

The gyrotropic medium is characterized by scalar magnetic permeability μ and electric permittivity tensor $\overline{\overline{\epsilon}}$. When the optic axis of the gyrotropic medium is in the $\hat{z}$ direction, the permittivity tensor is

$$\overline{\overline{\epsilon}} = \begin{bmatrix} \epsilon_t & -i\epsilon_g & 0 \\ i\epsilon_g & \epsilon_t & 0 \\ 0 & 0 & \epsilon_z \end{bmatrix} \tag{5.1}$$

In the *xyz* coordinate system, the constitutive relations in the gyrotropic medium are

$$\mathbf{E} = \overline{\overline{\kappa}} \cdot \mathbf{D} \tag{5.2}$$

$$\mathbf{H} = \nu\mathbf{B} \tag{5.3}$$

where

$$\bar{\bar{\kappa}} = \bar{\bar{\epsilon}}^{-1} = \begin{bmatrix} \kappa & -i\kappa_g & 0 \\ i\kappa_g & \kappa & 0 \\ 0 & 0 & \kappa_z \end{bmatrix} \tag{5.4}$$

$$\nu = \mu^{-1} \tag{5.5}$$

The notation $\bar{\bar{\kappa}}$ is the impermittivity tensor. It is known that there are two distinct characteristic waves, type I wave and type II wave, for the gyrotropic medium [123]. Their dispersion relation relating the frequency ω and the components of the wave vector $\mathbf{k}$ is

$$\omega^2 = \frac{\nu}{2}\left[\kappa(k^2 + k_z^2) + \kappa_z k_s^2 \pm \sqrt{(\kappa - \kappa_z)^2 k_s^4 + 4\kappa_g^2 k_z^2 k^2}\right] \tag{5.6}$$

Usually, the positive sign corresponds to type I wave and the negative sign corresponds to type II wave [123]. After mathematical manipulation of (5.6), we obtain a quartic equation of k_z associated with the two types of waves

$$a\, k_z^4 + b\, k_z^2 + c = 0 \tag{5.7}$$

where

$$a = (\kappa^2 - \kappa_z^2)\nu^2 \tag{5.8}$$

$$b = -2\kappa\,\omega^2\,\nu + (\kappa^2 - \kappa_g^2 + \kappa\,\kappa_z)k_s^2\,\nu^2 \tag{5.9}$$

$$c = \omega^4 - \omega^2(\kappa + \kappa_z)\,k_s^2\,\nu + \kappa\,\kappa_z\,k_s^4 \tag{5.10}$$

The solutions to (5.7) include four roots $k_z = \pm k_{z\alpha}\,(\alpha = \mathrm{I}, \mathrm{II})$. The subscripts I and II denote the type I wave and type II wave respectively, and $-k_{z\alpha}$ and $+k_{z\alpha}$ refer to the upward propagating wave and downward propagating wave respectively. By using the *kDB* system, the electric and magnetic fields in the *xyz* coordinate system can be represented as

$$\mathbf{E}(\mathbf{k}) = \overline{\overline{\kappa}} \cdot [D_1(\mathbf{k})\hat{h} - D_2(\mathbf{k})\hat{v}(k_z)] \tag{5.11}$$

$$\mathbf{H}(\mathbf{k}) = -\frac{\omega}{k}[D_2(\mathbf{k})\hat{h} + D_1(\mathbf{k})\hat{v}(k_z)] \tag{5.12}$$

where

$$\hat{h} = \frac{1}{k_s}(\hat{x}\,k_y - \hat{y}\,k_x) \tag{5.13}$$

$$\hat{v} = \frac{1}{k}(-k_z\,\hat{k}_s + k_s\,\hat{z}) \tag{5.14}$$

$$\hat{k}_s = \frac{1}{k_s}(\hat{x}\,k_x + \hat{y}\,k_y) \tag{5.15}$$

The term $D_{1,2}$ represents the two components of $\mathbf{D}$ projected onto the *kDB* coordinator system. The two components of the field vector are related by

$$\frac{D_2}{D_1} = \frac{-2i\,\kappa_g\,k\,k_z}{(\kappa - \kappa_z)\,k_s^2 \pm \sqrt{(\kappa - \kappa_z)^2 k_s^4 + 4\kappa_g^2\,k_z^2\,k^2}} \tag{5.16}$$

Here, one important point to note is that the determination of type I wave and type II wave. Since there are two square roots for the radical sign itself, adding the plus/minus sign would result in the discontinuity of k_z and k. Thus, it is difficult to determine type I or II wave just through the sign $\pm$ in (5.6) and (5.16). In order to avoid this discontinuity, we set the criterion of determining type I wave as that the imaginary part of k_{I} should be

a positive number.

Considering the roots of (5.7), we can write the characteristic field vectors as follows:

$$\mathbf{e}_{\alpha\beta}(\mathbf{k}_s) \equiv \mathbf{E}(\mathbf{k}_s, \pm k_{z\alpha}) = \bar{\bar{\kappa}} \cdot [D_{1\alpha}(\mathbf{k})\hat{h} - D_{2\alpha}(\mathbf{k})\hat{v}(\pm k_{z\alpha})] \tag{5.17}$$

$$\mathbf{h}_{\alpha\beta}(\mathbf{k}_s) \equiv \mathbf{H}(\mathbf{k}_s, \pm k_{z\alpha}) = -\frac{\omega}{k_\alpha}[D_{2\alpha}(\mathbf{k})\hat{h} + D_{1\alpha}(\mathbf{k})\hat{v}(\pm k_{z\alpha})] \tag{5.18}$$

where

$$k_\alpha^2 = k_s^2 + k_{z\alpha}^2 \tag{5.19}$$

and $\alpha = \mathrm{I}, \mathrm{II}$; $\beta = u, d$. In the Fourier spectral domain, the electric field $\mathbf{E}(\mathbf{k}_s; z\backslash z')$ $(z \neq z')$ can be expressed as a superposition of type I and type II waves

$$\begin{aligned} \mathbf{E}(\mathbf{k}_s; z\backslash z') &= \frac{1}{(2\pi)^2} \int_{-\infty}^{\infty} e^{-i\mathbf{k}_s \cdot (\mathbf{r}_s - \mathbf{r}_s')} \mathbf{E}(\mathbf{r}, \mathbf{r}') d\mathbf{r}_s \\ &= A_{\mathrm{I}\beta}(\mathbf{k}_s)\mathbf{e}_{\mathrm{I}\beta}(\mathbf{k}_s)e^{\pm ik_{z\mathrm{I}}(z-z')} + A_{\mathrm{II}\beta}(\mathbf{k}_s)\mathbf{e}_{\mathrm{II}\beta}(\mathbf{k}_s)e^{\pm ik_{z\mathrm{II}}(z-z')} \end{aligned} \tag{5.20}$$

In this work, we assume that the electric current point source is arbitrarily oriented, which is expressed by

$$\mathbf{J}(\mathbf{r}) = \hat{a}\delta(\mathbf{r} - \mathbf{r}') \tag{5.21}$$

where $\hat{a}$ is an arbitrary unit vector. In order to obtain the unknown values of amplitudes $A_{\alpha\beta}(\mathbf{k}_s)$, we employ the spectral-domain wave equation to formulate the electric field

$$\mathbf{L}(\mathbf{k}) \cdot \mathbf{E}(\mathbf{k}) = -i\omega\mu\mathbf{J}(\mathbf{k}_s, k_z) \tag{5.22}$$

where

$$\mathbf{J}(\mathbf{k}_s, k_z) = -\frac{1}{(2\pi)^3}\hat{a} \tag{5.23}$$

$\mathbf{L}(\mathbf{k})$ is the dyadic Helmholtz operator for the gyrotropic medium.

$$\mathbf{L}(\mathbf{k}) = k^2\mathbf{I} - \omega^2\mu\bar{\bar{\epsilon}} - \mathbf{kk} \tag{5.24}$$

After algebraic manipulations, (5.24) can be recast in the following form:

$$\begin{aligned}\mathbf{L}(\mathbf{k}) =& k_\alpha^2\mathbf{I} - \omega^2\mu\bar{\bar{\epsilon}} - \mathbf{k}_{\alpha\beta}\mathbf{k}_{\alpha\beta} + (k_z^2 - k_{z\alpha}^2)(\hat{h}\hat{h} + \hat{k}_s\hat{k}_s) - \\ & k_s[k_z - (\pm k_{z\alpha})](\hat{z}\hat{k}_s + \hat{k}_s\hat{z})\end{aligned} \tag{5.25}$$

By using the Fourier transform and (5.20), the expression of $\mathbf{E}(\mathbf{k})$ can be written as [70]

$$\begin{aligned}\mathbf{E}(\mathbf{k}) &= \frac{1}{2\pi}\int_{-\infty}^{\infty} e^{ik_z(z-z')}\mathbf{E}(\mathbf{k}_s; z\backslash z')dz \\ &= \frac{1}{2\pi i}\sum_{\alpha=\mathrm{I,II}}\left[\frac{A_{\alpha u}}{k_z - k_{z\alpha}}\mathbf{e}_{\alpha u} - \frac{A_{\alpha d}}{k_z + k_{z\alpha}}\mathbf{e}_{\alpha d}\right]\end{aligned} \tag{5.26}$$

Substituting (5.25) and (5.26) into (5.22), we can obtain

$$\begin{aligned}&\frac{1}{2\pi i}\sum_{\alpha=\mathrm{I,II}}\{A_{\alpha u}[(k_z + k_{z\alpha})(\hat{h}\hat{h} + \hat{k}_s\hat{k}_s) - k_s(\hat{z}\hat{k}_s + \hat{k}_s\hat{z})] \cdot \mathbf{e}_{\alpha u} - \\ &\qquad A_{\alpha d}[(k_z - k_{z\alpha})(\hat{h}\hat{h} + \hat{k}_s\hat{k}_s) - k_s(\hat{z}\hat{k}_s + \hat{k}_s\hat{z})] \cdot \mathbf{e}_{\alpha d}\} \\ &= -i\omega\mu\mathbf{J}(\mathbf{k}_s, k_z)\end{aligned} \tag{5.27}$$

The solutions to the four unknowns $A_{\alpha\beta}$ ($\alpha = \mathrm{I, II}; \beta = u, d$) need four independent

equations. Subsequently, we substitute $k_z = \pm k_{z\alpha}$ and premultiply (5.27) by the characteristic field vectors $\mathbf{e}_{\alpha'\beta'}$. Finally, we get four independent equations for the solutions of $A_{\alpha\beta}$. Considering the coupled relationship between the type I wave and type II wave, we write the four equations as

$$\mathbf{Q}_{uu} \cdot \mathbf{A}_u - \mathbf{Q}_{ud} \cdot \mathbf{A}_d = -2\pi\omega\mu\, \mathbf{\Omega}_u \cdot \mathbf{S}_u \tag{5.28}$$

$$\mathbf{Q}_{du} \cdot \mathbf{A}_u - \mathbf{Q}_{dd} \cdot \mathbf{A}_d = -2\pi\omega\mu\, \mathbf{\Omega}_d \cdot \mathbf{S}_d \tag{5.29}$$

where

$$\mathbf{Q}_{\beta\beta} = \begin{bmatrix} Q_{\mathrm{I}\beta,\mathrm{I}\beta} & Q_{\mathrm{I}\beta,\mathrm{II}\beta} \\ Q_{\mathrm{II}\beta,\mathrm{I}\beta} & Q_{\mathrm{II}\beta,\mathrm{II}\beta} \end{bmatrix} \tag{5.30}$$

$$\mathbf{A}_\beta = \begin{bmatrix} A_{\mathrm{I}\beta} \\ A_{\mathrm{II}\beta} \end{bmatrix} \tag{5.31}$$

$$\mathbf{\Omega}_\beta = \begin{bmatrix} \mathbf{e}_{\mathrm{I}\beta} & 0 \\ 0 & \mathbf{e}_{\mathrm{II}\beta} \end{bmatrix} \tag{5.32}$$

$$\mathbf{S}_\beta = \begin{bmatrix} -\mathbf{J}(\mathbf{k}_s, \pm k_{z\mathrm{I}}) \\ -\mathbf{J}(\mathbf{k}_s, \pm k_{z\mathrm{II}}) \end{bmatrix} \tag{5.33}$$

$$Q_{\alpha\beta,\alpha'\beta'} = (k_{z\alpha\beta} + k_{z\alpha'\beta'})\mathbf{e}_{\alpha\beta} \cdot \mathbf{e}_{\alpha'\beta'} - \mathbf{e}_{\alpha\beta} \cdot (\hat{z}\mathbf{k}_{\alpha\beta} + \mathbf{k}_{\alpha'\beta'}\hat{z}) \cdot \mathbf{e}_{\alpha'\beta'} \tag{5.34}$$

Solving (5.28) and (5.29) yields

$$\mathbf{A}_u = -\pi\omega\mu\, (\mathbf{M}_{uu} \cdot \mathbf{\Omega}_u \cdot \mathbf{S}_u + \mathbf{M}_{du} \cdot \mathbf{\Omega}_d \cdot \mathbf{S}_d) \tag{5.35}$$

$$\mathbf{A}_d = -\pi\omega\mu\ (\mathbf{M}_{ud}\cdot\mathbf{\Omega}_u\cdot\mathbf{S}_u + \mathbf{M}_{dd}\cdot\mathbf{\Omega}_d\cdot\mathbf{S}_d) \tag{5.36}$$

with

$$\mathbf{M}_{\beta\beta'} = 2\left(\mathbf{Q}_{\beta\beta'} - \mathbf{Q}_{\beta\overline{\beta'}}\cdot\mathbf{Q}^{-1}_{\overline{\beta}\overline{\beta'}}\cdot\mathbf{Q}_{\overline{\beta}\beta'}\right)^{-1}, \quad \beta' = u \tag{5.37}$$

$$\mathbf{M}_{\beta\beta'} = -2\left(\mathbf{Q}_{\beta\beta'} - \mathbf{Q}_{\beta\overline{\beta'}}\cdot\mathbf{Q}^{-1}_{\overline{\beta}\overline{\beta'}}\cdot\mathbf{Q}_{\overline{\beta}\beta'}\right)^{-1}, \quad \beta' = d \tag{5.38}$$

with $\overline{\beta} = u$ if $\beta = d$ and $\overline{\beta} = d$ if $\beta = u$. Substituting (5.35)(5.36) into (5.20) and casting it in a matrix form, we obtain

$$\begin{aligned}\mathbf{E}(\mathbf{k}_s; z\backslash z') = &-\pi\omega\mu\mathbf{P}^t_\beta(z\backslash z')\cdot\mathbf{\Omega}_\beta\cdot\\ &\left(\mathbf{M}_{\beta\beta}\cdot\mathbf{\Omega}_\beta\cdot\mathbf{S}_\beta + \mathbf{M}_{\overline{\beta}\beta}\cdot\mathbf{\Omega}_{\overline{\beta}}\cdot\mathbf{S}_{\overline{\beta}}\right), \qquad z \neq z'\end{aligned} \tag{5.39}$$

where

$$\mathbf{P}_\beta(z\backslash z') = \begin{bmatrix} e^{\pm ik_{z\mathrm{I}}(z-z')} \\ \\ e^{\pm ik_{z\mathrm{II}}(z-z')} \end{bmatrix} \tag{5.40}$$

Then, the electric field in the spatial domain is expressed by applying the inverse Fourier transform to $\mathbf{E}(\mathbf{k}_s; z\backslash z')$

$$\begin{aligned}\mathbf{E}(\mathbf{r}, \mathbf{r}') = &-\pi\omega\mu\int_{-\infty}^{\infty} e^{-i\mathbf{k}_s\cdot(\mathbf{r}_s-\mathbf{r}'_s)}\mathbf{P}^t_\beta(z\backslash z')\cdot\mathbf{\Omega}_\beta\cdot\\ &\left(\mathbf{M}_{\beta\beta}\cdot\mathbf{\Omega}_\beta\cdot\mathbf{S}_\beta + \mathbf{M}_{\overline{\beta}\beta}\cdot\mathbf{\Omega}_{\overline{\beta}}\cdot\mathbf{S}_{\overline{\beta}}\right) d\mathbf{k}_s, \qquad \mathbf{r} \neq \mathbf{r}'\end{aligned} \tag{5.41}$$

When $\mathbf{r} = \mathbf{r}'$, the above formulation for the electric field does not exhibit the proper singular behavior. This singular behavior can be captured from the asymptotic behavior

of $\mathbf{E}(\mathbf{k})$ when $|k_z| \to \infty$, which is given by

$$\mathbf{E}(\mathbf{k}) \sim -\frac{1}{(2\pi)^3}\frac{1}{i\omega\hat{z}\cdot\overline{\overline{\epsilon}}\cdot\hat{z}}\hat{z}\hat{z}\cdot\hat{a}\delta(z-z'), \quad |k_z| \to \infty \tag{5.42}$$

Thus, the complete expression for the electric field in the unbounded gyrotropic medium is represented by

$$\begin{aligned}\mathbf{E}(\mathbf{r},\mathbf{r}') = &-\frac{1}{i\omega\hat{z}\cdot\overline{\overline{\epsilon}}\cdot\hat{z}}\hat{z}\hat{z}\cdot\hat{a}\delta(\mathbf{r}-\mathbf{r}')- \\ &\pi\omega\mu\int_{-\infty}^{\infty} e^{-i\mathbf{k}_s\cdot(\mathbf{r}_s-\mathbf{r}_s')}\mathbf{P}_\beta^t(z\backslash z')\cdot\mathbf{\Omega}_\beta\cdot \\ &\left(\mathbf{M}_{\beta\beta}\cdot\mathbf{\Omega}_\beta\cdot\mathbf{S}_\beta + \mathbf{M}_{\overline{\beta}\beta}\cdot\mathbf{\Omega}_{\overline{\beta}}\cdot\mathbf{S}_{\overline{\beta}}\right) d\mathbf{k}_s\end{aligned} \tag{5.43}$$

Since the electric field in an unbounded medium relates the DGF to the current via

$$\mathbf{E}_n(\mathbf{r}) = \int_{V'} d\mathbf{r}'\mathbf{G}_{nn}(\mathbf{r},\mathbf{r}')\cdot\mathbf{J}(\mathbf{r}') \tag{5.44}$$

the formulations of the DGF in the unbounded gyrotropic medium can be derived from (5.43) in the following explicit form.

for $z > z'$

$$\begin{aligned}\mathbf{G}(\mathbf{r},\mathbf{r}') = &-\frac{1}{i\omega\hat{z}\cdot\overline{\overline{\epsilon}}\cdot\hat{z}}\hat{z}\hat{z}\,\delta(\mathbf{r}-\mathbf{r}') - \frac{\omega\mu}{8\pi^2} \\ &\int_{-\infty}^{\infty} d\mathbf{k}_s e^{-i\mathbf{k}_s\cdot(\mathbf{r}_s-\mathbf{r}_s')}\cdot\left[e^{-ik_{z\mathrm{I}}(z-z')}\mathbf{e}_{\mathrm{I}u}\mathbf{u}_{\mathrm{I}u} + e^{-ik_{z\mathrm{II}}(z-z')}\mathbf{e}_{\mathrm{II}u}\mathbf{u}_{\mathrm{II}u}\right]\end{aligned} \tag{5.45}$$

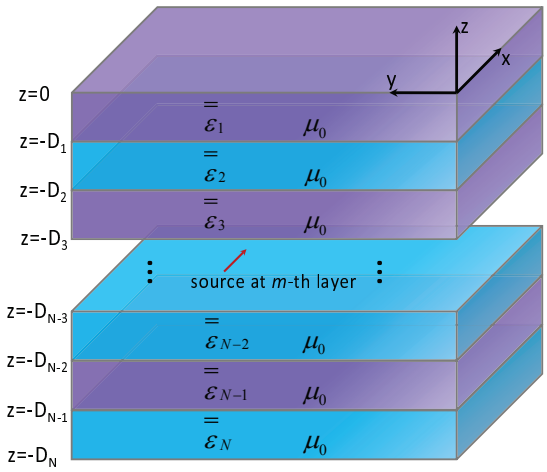

Figure 5.1: Geometry of the general planar multilayered gyrotropic medium.

for $z < z'$

$$\mathbf{G}(\mathbf{r},\mathbf{r}') = -\frac{1}{i\omega\hat{z}\cdot\bar{\bar{\epsilon}}\cdot\hat{z}}\hat{z}\hat{z}\,\delta(\mathbf{r}-\mathbf{r}') - \frac{\omega\mu}{8\pi^2} \int_{-\infty}^{\infty} d\mathbf{k}_s e^{-i\mathbf{k}_s\cdot(\mathbf{r}_s-\mathbf{r}'_s)} \cdot \left[e^{ik_{z\mathrm{I}}(z-z')}\mathbf{e}_{\mathrm{I}d}\mathbf{u}_{\mathrm{I}d} + e^{ik_{z\mathrm{II}}(z-z')}\mathbf{e}_{\mathrm{II}d}\mathbf{u}_{\mathrm{II}d}\right] \tag{5.46}$$

where

$$\begin{aligned}\mathbf{u}_{\mathrm{I}\beta} =& \mathbf{M}_{\beta\beta}(1,1)\,\mathbf{e}_{\mathrm{I}\beta} + \mathbf{M}_{\beta\beta}(1,2)\,\mathbf{e}_{\mathrm{II}\beta} \\ & \mathbf{M}_{\bar{\beta}\beta}(1,1)\,\mathbf{e}_{\mathrm{I}\bar{\beta}} + \mathbf{M}_{\bar{\beta}\beta}(1,2)\,\mathbf{e}_{\mathrm{II}\bar{\beta}}\end{aligned} \tag{5.47}$$

$$\begin{aligned}\mathbf{u}_{\mathrm{II}\beta} =& \mathbf{M}_{\beta\beta}(2,1)\,\mathbf{e}_{\mathrm{I}\beta} + \mathbf{M}_{\beta\beta}(2,2)\,\mathbf{e}_{\mathrm{II}\beta} \\ & \mathbf{M}_{\bar{\beta}\beta}(2,1)\,\mathbf{e}_{\mathrm{I}\bar{\beta}} + \mathbf{M}_{\bar{\beta}\beta}(2,2)\,\mathbf{e}_{\mathrm{II}\bar{\beta}}\end{aligned} \tag{5.48}$$

5.4 Dyadic Green's Function for the Planar Multilayered Gyrotropic Medium

In this section, based on the boundary condition and the WIT, the holistic formulations of reflection and transmission coefficients are systematically derived. Then, similar to the preceding chapter, the complete and generalized formulations of the spectral-domain Green's function in the planar multilayered gyrotropic media can be obtained for three cases: $m = n$, $m > n$ and $m < n$. The formulations are omitted in this chapter.

5.4.1 Local Reflection and Transmission Matrices

To satisfy the boundary conditions of the continuity of the tangential electric and magnetic fields, the tangential components of $\mathbf{E}$ and $\mathbf{H}$ along the the $\hat{h}$ and $\hat{k}_s$ directions are matched at the interface of two layers.

$$\mathbf{X}_{\beta}^{(m)} + \mathbf{X}_{\overline{\beta}}^{(m)} \cdot \mathbf{R}_{m,n}^{(\beta)} = \mathbf{X}_{\beta}^{(n)} \cdot \mathbf{T}_{m,n}^{(\beta)} \tag{5.49}$$

$$\mathbf{Y}_{\beta}^{(m)} + \mathbf{Y}_{\overline{\beta}}^{(m)} \cdot \mathbf{R}_{m,n}^{(\beta)} = \mathbf{Y}_{\beta}^{(n)} \cdot \mathbf{T}_{m,n}^{(\beta)} \tag{5.50}$$

where $\mathbf{R}_{m,n}^{\beta}$ is the local reflection matrix and $\mathbf{T}_{m,n}^{\beta}$ is the local transmission matrix. The character $\beta = u$ ($\overline{\beta} = d$) for $m > n$ and $\beta = d$ ($\overline{\beta} = u$) for $m < n$.

$$\mathbf{R}_{m,n}^{\beta} = \begin{bmatrix} R_{mn}^{\mathrm{I,I}} & R_{mn}^{\mathrm{I,II}} \\ R_{mn}^{\mathrm{II,I}} & R_{mn}^{\mathrm{II,II}} \end{bmatrix} \tag{5.51}$$

$$\mathbf{T}_{m,n}^{\beta} = \begin{bmatrix} T_{mn}^{\mathrm{I,I}} & T_{mn}^{\mathrm{I,II}} \\ T_{mn}^{\mathrm{II,I}} & T_{mn}^{\mathrm{II,II}} \end{bmatrix} \tag{5.52}$$

$$\mathbf{X}_{\beta}^{(m)} = \begin{bmatrix} \hat{h} \cdot \mathbf{e}_{\mathrm{I}\beta}^{(m)} & \hat{h} \cdot \mathbf{e}_{\mathrm{II}\beta}^{(m)} \\ \hat{k}_s \cdot \mathbf{e}_{\mathrm{I}\beta}^{(m)} & \hat{k}_s \cdot \mathbf{e}_{\mathrm{II}\beta}^{(m)} \end{bmatrix} \tag{5.53}$$

$$\mathbf{Y}_{\beta}^{(m)} = \begin{bmatrix} \hat{h} \cdot \mathbf{h}_{\mathrm{I}\beta}^{(m)} & \hat{h} \cdot \mathbf{h}_{\mathrm{II}\beta}^{(m)} \\ \hat{k}_s \cdot \mathbf{h}_{\mathrm{I}\beta}^{(m)} & \hat{k}_s \cdot \mathbf{h}_{\mathrm{II}\beta}^{(m)} \end{bmatrix} \tag{5.54}$$

R_{mn}^{α} is the local reflection coefficient when the incident plane wave is in region m; T_{mn}^{α} is the local transmission coefficient from region m to region n.

Derived from the (5.49) and (5.50), the reflection and transmission matrices can be expressed as

$$\mathbf{R}_{m,n}^{(\beta)} = \left[\mathbf{X}_{\bar{\beta}}^{(m)} - \mathbf{X}_{\beta}^{(n)} \cdot \{\mathbf{Y}_{\beta}^{(n)}\}^{-1} \cdot \mathbf{Y}_{\bar{\beta}}^{(m)}\right]^{-1} \cdot \left[-\mathbf{X}_{\beta}^{(m)} + \mathbf{X}_{\beta}^{(n)} \cdot \{\mathbf{Y}_{\beta}^{(n)}\}^{-1} \cdot \mathbf{Y}_{\beta}^{(m)}\right] \tag{5.55}$$

$$\mathbf{T}_{m,n}^{(\beta)} = \left[\mathbf{Y}_{\beta}^{(n)} - \mathbf{Y}_{\bar{\beta}}^{(m)} \cdot \{\mathbf{X}_{\bar{\beta}}^{(m)}\}^{-1} \cdot \mathbf{X}_{\beta}^{(n)}\right]^{-1} \cdot \left[\mathbf{Y}_{\beta}^{(m)} - \mathbf{Y}_{\bar{\beta}}^{(m)} \cdot \{\mathbf{X}_{\bar{\beta}}^{(m)}\}^{-1} \cdot \mathbf{X}_{\beta}^{(m)}\right] \tag{5.56}$$

5.4.2 Global Reflection and Transmission Matrices

Because of multiple reflections and cross-polarization effects, the electric field in an arbitrary layer n is represented in terms of upward propagating and downward propagating

waves, as follows:

$$\begin{aligned}\mathbf{E}_n(z_n) \equiv \mathbf{E}(\mathbf{k}_s; z_n) =& f_n^{\mathrm{I}}\mathbf{e}_{\mathrm{I}u}^{(n)} e^{-ik_{z\mathrm{I}}^{(n)} z_n} + f_n^{\mathrm{II}}\mathbf{e}_{\mathrm{II}u}^{(n)} e^{-ik_{z\mathrm{II}}^{(n)} z_n} \\ &+ g_n^{\mathrm{I}}\mathbf{e}_{\mathrm{I}d}^{(n)} e^{ik_{z\mathrm{I}}^{(n)} z_n} + g_n^{\mathrm{II}}\mathbf{e}_{\mathrm{II}d}^{(n)} e^{ik_{z\mathrm{II}}^{(n)} z_n}\end{aligned} \tag{5.57}$$

which can be cast in the following matrix form

$$\mathbf{E}_n(z_n) = \mathbf{G}_u^{(n)}(z_n) \cdot \mathbf{f}_n + \mathbf{G}_d^{(n)}(z_n) \cdot \mathbf{g}_n \tag{5.58}$$

where

$$\mathbf{G}_u^{(n)}(z_n) = \begin{bmatrix} e^{-ik_{z\mathrm{I}}^{(n)} z_n} & 0 \\ 0 & e^{-ik_{z\mathrm{II}}^{(n)} z_n} \end{bmatrix} \tag{5.59}$$

$$\mathbf{G}_d^{(n)}(z_n) = \begin{bmatrix} e^{ik_{z\mathrm{I}}^{(n)} z_n} & 0 \\ 0 & e^{ik_{z\mathrm{II}}^{(n)} z_n} \end{bmatrix} \tag{5.60}$$

$$\mathbf{f}_n = \begin{bmatrix} f_n^{\mathrm{I}} \\ f_n^{\mathrm{II}} \end{bmatrix} \tag{5.61}$$

$$\mathbf{g}_n = \begin{bmatrix} g_n^{\mathrm{I}} \\ g_n^{\mathrm{II}} \end{bmatrix} \tag{5.62}$$

$\mathbf{G}_u^{(n)}(z_n)$ represents the upward propagating wave expressed in the $[\mathbf{e}_{\mathrm{I}u}^{(n)}, \mathbf{e}_{\mathrm{II}u}^{(n)}]$ coordinate system. The first component on the diagonal of $\mathbf{G}_u^{(n)}(z_n)$ is along $\mathbf{e}_{\mathrm{I}u}^{(n)}$ and the second component along $\mathbf{e}_{\mathrm{II}u}^{(n)}$. Similarly, $\mathbf{G}_d^{(n)}(z_n)$ represents the downward propagating wave expressed in the $[\mathbf{e}_{\mathrm{I}d}^{(n)}, \mathbf{e}_{\mathrm{II}d}^{(n)}]$ coordinate system. In the layer $n-1$, the electric field vector

is expressed by

$$\mathbf{E}_{n-1}(z_{n-1}) = \mathbf{G}_u^{(n-1)}(z_{n-1}) \cdot \mathbf{f}_{n-1} + \mathbf{G}_d^{(n-1)}(z_{n-1}) \cdot \mathbf{g}_{n-1} \tag{5.63}$$

At the interface of layer $n-1$ and layer n, the upward global reflection and transmission matrices are related with the fields by the following relationships:

$$\mathbf{G}_d^{(n)}(z_n = -D_{n-1}) \cdot \mathbf{g}_n = \mathbf{R}_{Un} \cdot \mathbf{G}_u^{(n)}(z_n = -D_{n-1}) \cdot \mathbf{f}_n \tag{5.64}$$

$$\mathbf{T}_{Un} \cdot \mathbf{G}_u^{(n)}(z_n = -D_{n-1}) \cdot \mathbf{f}_n = \mathbf{G}_u^{(n-1)}(z_{n-1} = -D_{n-1}) \cdot \mathbf{f}_{n-1} \tag{5.65}$$

where $\mathbf{R}_{Un}$ and $\mathbf{T}_{Un}$ are the global reflection matrix and global transmission matrix from layer n to layer $n-1$, respectively. It is noted that the downward propagating wave in the layer n is a consequence of the transmission of the downward propagating wave in the layer $n-1$ in combination with the reflection of the upward propagating wave in the layer n. Thus, at the interface $z = -D_{n-1}$, the constraint condition is

$$\begin{aligned} \mathbf{R}_{Un} \cdot \mathbf{G}_u^{(n)}(z_n = -D_{n-1}) \cdot \mathbf{f}_n &= \mathbf{R}_{n,n-1}^{(u)} \cdot \mathbf{G}_u^{(n)}(z_n = -D_{n-1}) \cdot \mathbf{f}_n \\ &+ \mathbf{T}_{n-1,n}^{d} \cdot \mathbf{G}_d^{(n-1)}(z_n = -D_{n-1}) \cdot \mathbf{g}_{n-1} \end{aligned} \tag{5.66}$$

By using the expression of $\mathbf{g}_n$ from (5.64), we can write (5.66) as

$$\begin{aligned} \mathbf{R}_{Un} \cdot \mathbf{G}_u^{(n)}(z_n = -D_{n-1}) \cdot \mathbf{f}_n &= \mathbf{R}_{n,n-1}^{(u)} \cdot \mathbf{G}_u^{(n)}(z_n = -D_{n-1}) \cdot \mathbf{f}_n \\ &+ \mathbf{T}_{n-1,n}^{d} \cdot \mathbf{G}_d^{(n-1)}(z_n = -D_{n-1}) \cdot \mathbf{G}_d^{(n-1)}(z_{n-1} = -D_{n-2})^{-1} \\ &\cdot \mathbf{R}_{Un-1} \cdot \mathbf{G}_u^{(n-1)}(z_{n-1} = -D_{n-2}) \cdot \mathbf{f}_{n-1} \end{aligned} \tag{5.67}$$

Next, we notice that the upward propagating wave in the layer $n-1$ is a superposition of the reflection of the downward propagating wave in the layer $n-1$ and the transmission of the upward propagating wave in the layer n. At the interface $z = -D_{n-1}$, we have the constraint condition

$$\begin{aligned}\mathbf{G}_u^{(n-1)}(z_{n-1} = -D_{n-1}) \cdot \mathbf{f}_{n-1} &= \mathbf{T}_{n,n-1}^{(n)} \cdot \mathbf{G}_u^{(n)}(z_n = -D_{n-1}) \cdot \mathbf{f}_n \\ &+ \mathbf{R}_{n-1,n}^{(d)} \cdot \mathbf{G}_d^{(n-1)}(z_{n-1} = -D_{n-1}) \cdot \mathbf{g}_{n-1}\end{aligned} \tag{5.68}$$

Substituting the expression of g_{n-1} from (5.64), we can write (5.68) as

$$\begin{aligned}\mathbf{G}_u^{(n-1)}(z_{n-1} = -D_{n-1}) \cdot \mathbf{f}_{n-1} &= \mathbf{T}_{n,n-1}^{(n)} \cdot \mathbf{G}_u^{(n)}(z_n = -D_{n-1}) \cdot \mathbf{f}_n \\ &+ \mathbf{R}_{n-1,n}^{(d)} \cdot \mathbf{G}_d^{(n-1)}(z_{n-1} = -D_{n-1}) \cdot \mathbf{G}_d^{(n-1)}(z_{n-1} = -D_{n-2})^{-1} \\ &\cdot \mathbf{R}_{Un-1} \cdot \mathbf{G}_u^{(n-1)}(z_{n-1} = -D_{n-2}) \cdot \mathbf{f}_{n-1}\end{aligned} \tag{5.69}$$

From (5.67) and (5.69), we finally get the following recursive expression for the upward global reflection matrix:

$$\begin{aligned}\mathbf{R}_{Un} =& \mathbf{R}_{n,n-1}^{(u)} + \mathbf{T}_{n-1,n}^{(d)} \cdot \mathbf{G}_d^{(n-1)}(z_{n-1} = -D_{n-1} + D_{n-2}) \cdot \\ & \mathbf{R}_{Un-1} \cdot \mathbf{G}_u^{(n-1)}(z_{n-1} = -D_{n-2} + D_{n-1}) \cdot \\ & \left[\mathbf{I} - \mathbf{R}_{n-1,n}^{(d)} \cdot \mathbf{G}_d^{(n-1)}(z_{n-1} = -D_{n-1} + D_{n-2}) \cdot \mathbf{R}_{Un-1} \cdot \right. \\ & \left. \mathbf{G}_u^{(n-1)}(z_{n-1} = -D_{n-2} + D_{n-1})\right]^{-1} \cdot \mathbf{T}_{n,n-1}^{(u)}\end{aligned} \tag{5.70}$$

Similarly, the recursive formulation of the downward global reflection matrix is

derived as follows,

$$\begin{aligned}\mathbf{R}_{Dn} =&\mathbf{R}^{(d)}_{n,n+1} + \mathbf{T}^{(u)}_{n+1,n} \cdot \mathbf{G}^{(n+1)}_{u}(z_{n+1} = -D_n + D_{n+1})\cdot \\ &\mathbf{R}_{Dn+1} \cdot \mathbf{G}^{(n+1)}_{u}(z_{n+1} = -D_{n+1} + D_n)\cdot \\ &\left[\mathbf{I} - \mathbf{R}^{(u)}_{n+1,n} \cdot \mathbf{G}^{(n+1)}_{u}(z_{n+1} = -D_n + D_{n+1}) \cdot \mathbf{R}_{Dn+1}\cdot \right. \\ &\left.\mathbf{G}^{(n+1)}_{d}(z_{n+1} = -D_{n+1} + D_n)\right]^{-1} \cdot \mathbf{T}^{(d)}_{n,n+1}\end{aligned} \tag{5.71}$$

From (5.65) and (5.69), the recursive expression for the upward global transmission matrix is given by:

$$\begin{aligned}\mathbf{T}_{Un} = &\left[\mathbf{I} - \mathbf{R}^{(d)}_{n-1,n} \cdot \mathbf{G}^{(n-1)}_{d}(z_{n-1} = -D_{n-1} + D_{n-2})\cdot \right. \\ &\left.\mathbf{R}_{Un-1} \cdot \mathbf{G}^{(n-1)}_{u}(z_{n-1} = -D_{n-2} + D_{n-1})\right]^{-1} \cdot \mathbf{T}^{(u)}_{n,n-1}\end{aligned} \tag{5.72}$$

Similarly, the downward global transmission matrix can be expressed as:

$$\begin{aligned}\mathbf{T}_{Dn} = &\left[\mathbf{I} - \mathbf{R}^{(u)}_{n+1,n} \cdot \mathbf{G}^{(n+1)}_{u}(z_{n+1} = -D_n + D_{n+1})\cdot \right. \\ &\left.\mathbf{R}_{Dn+1} \cdot \mathbf{G}^{(n+1)}_{d}(z_{n+1} = -D_{n+1} + D_n)\right]^{-1} \cdot \mathbf{T}^{(d)}_{n,n+1}\end{aligned} \tag{5.73}$$

Most of what we have done in this section on dielectric gyrotropic media applies in a straight-froward way to other complex media as well.

5.5 Numerical Results and Discussions

Various examples will be considered in this section in order to investigate the accuracy and efficiency of the proposed algorithm through the calculation of the DGF for the

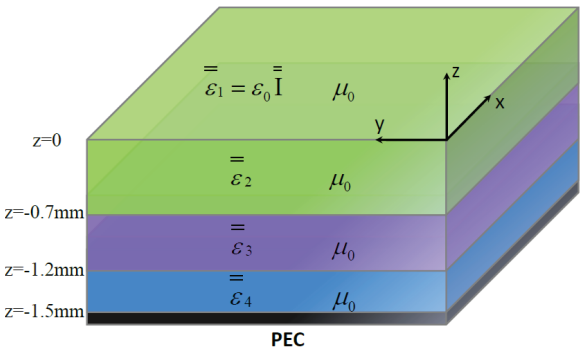

Figure 5.2: Geometry of a four-layer medium.

planar multilayered structure depicted in Fig. 5.2. The uppermost layer is taken to be free space, while the lowermost layer is PEC. The operating frequency is 3 GHz for all examples. To expedite the calculation of the Sommerfeld integrals, the newly developed MFHT method is employed to calculate the DGF's.

5.5.1 Comparison of Numerical Results in Spectral Domain

In the case of isotropic medium, the formulation of the correlation between the Green's function in the EFIE and that in the MPIE is given by

$$\overline{\overline{G}}^{EJ} = i\omega\mu_0 \overline{\overline{G}}^{AJ} + \frac{1}{i\omega\epsilon_0} \nabla\nabla' G^{VJ} \tag{5.74}$$

Here, one element of the DGF obtained by the present algorithm is compared to the corresponding result from the Green's function used in the MPIE for a four-layer planar isotropic medium, as shown in Fig. 5.2. Fig. 5.3 depicts the spectrum of G_{zz}^{EJ}. It is evident from the resultant plots that the spectral-domain Green's functions obtained by the proposed algorithm agree very well with the existing results from the MPIE when

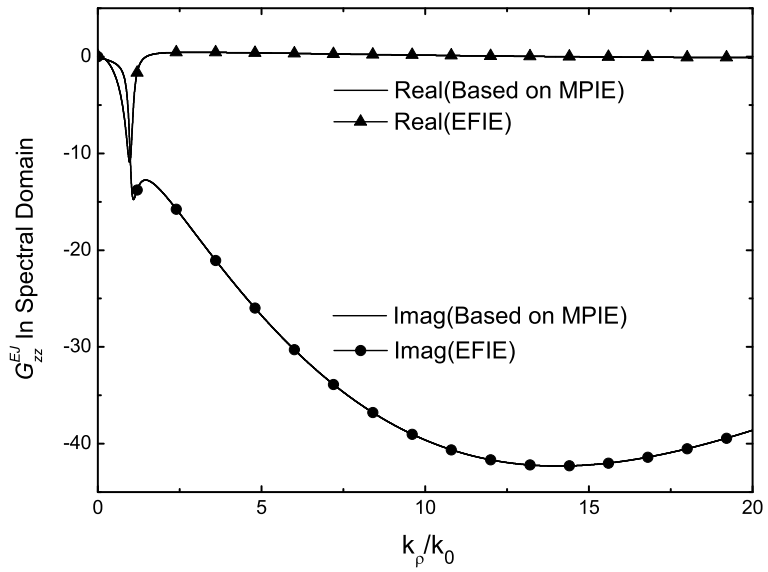

Figure 5.3: Magnitude of $\widetilde{G}_{zz}^{EJ}$ versus k_ρ for the four-layer isotropic medium with the following parameters: $z' = 0$ mm; $z = -1.2$ mm; layer 2: $\epsilon_2 = 2.1\epsilon_0$; layer 3: $\epsilon_3 = 9.8\epsilon_0$; layer 4: $\epsilon_4 = 8.6\epsilon_0$. The solid lines correspond to results obtained by the present algorithm while the dots correspond to results from MPIE.

reduced to the isotropic case. The accuracy of the DGF in the spectral domain has been validated.

5.5.2 Comparison of Numerical Results in Spatial Domain

The MFHT method is employed for the approximation of the spatial-domain Green's functions for a four-layer planar gyrotropic medium, as shown in Fig. 5.2. Fig. 5.4 depicts the magnitude of the element G_{zz}^{EJ} of the DGF. In the three cases of Fig. 5.4, the following parameters are kept unchanged, $\epsilon_t^{(2)} = 2.1\epsilon_0$, $\epsilon_z^{(2)}/\epsilon_t^{(2)} = 1.5$, $\epsilon_g^{(2)} = 2\epsilon_0$, $\epsilon_t^{(3)} = 9.8\epsilon_0$ and $\epsilon_t^{(4)} = 8.6\epsilon_0$. The parameters that are changed for the three cases are as follows. In the first case, $m = n = 2$, $z' = -0.7$ mm, $z = -0.1$ mm. In the second case, $m = 1$, $n = 3$, $z' = 0$ mm, $z = -1.2$ mm. In the third case, $m = 3$, $n = 2$,

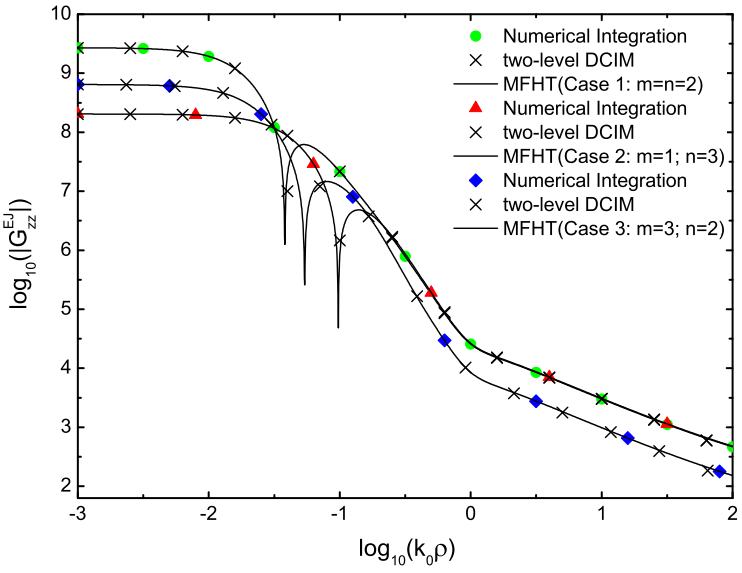

Figure 5.4: Magnitudes of G_{zz}^{EJ} versus ρ for the four-layer structure with the following parameters: Case 1: $z' = -0.7$ mm, $z = -0.1$ mm, $\epsilon_z^{(2)}/\epsilon_t^{(2)} = 1.5$, $\epsilon_g^{(2)}/\epsilon_0 = 2$; Case 2: $z' = 0$ mm, $z = -1.2$ mm, $\epsilon_z^{(2)}/\epsilon_t^{(2)} = 1.5$, $\epsilon_g^{(2)}/\epsilon_0 = 2$; Case 3: $z' = -1.2$ mm, $z = -0.6$ mm, $\epsilon_z^{(2)}/\epsilon_t^{(2)} = 1.5$, $\epsilon_g^{(2)}/\epsilon_0 = 2$. The solid lines correspond to results obtained by the MFHT method while the dots correspond to results obtained by the numerical integration and DCIM.

$z' = -1.2$ mm, $z = -0.6$ mm. The reference results, represented by the discrete points in the plots, are obtained through the numerical integration of the spectrum on deformed paths parallel to the real axis. The MFHT-based numerical results are represented by the solid lines, while the DCIM-based numerical results are represented by the symbol $\times$. Clearly, the MFHT-based results are in excellent agreement with the numerical integration results and DCIM-based results. The results offer a strong confirmation that based on the MFHT method, the DGF's for the planar multilayered gyrotropic medium can be calculated accurately.

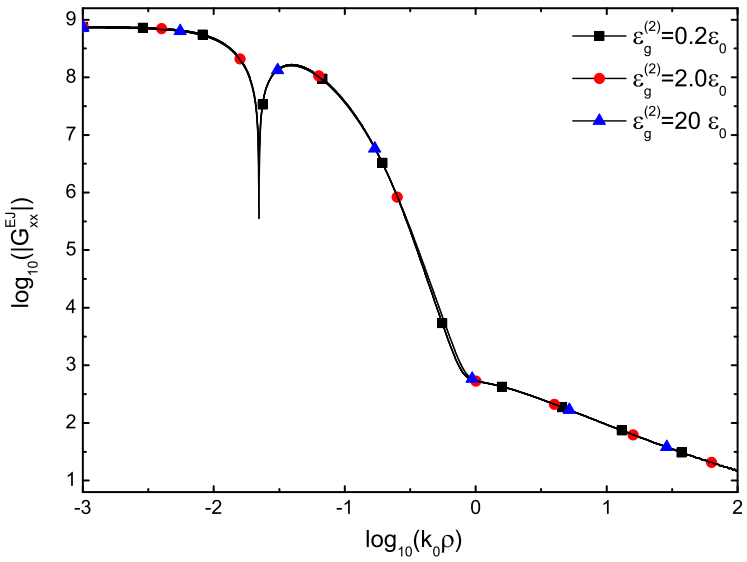

Figure 5.5: Magnitudes of G_{xx}^{EJ} versus ρ for the four-layer structure with the following parameters: m=n=2; $z' = -0.7$ mm; $z = -0.1$ mm; layer 2: $\epsilon_t^{(2)} = 2.1\epsilon_0$, $\epsilon_z^{(2)}/\epsilon_t^{(2)} = 1.5$, $\epsilon_g^{(2)}/\epsilon_0 = 0.2/2.0/20$; layer 3: $\bar{\bar{\epsilon}}^{(3)} = 9.8\epsilon_0\bar{\bar{I}}$; layer 4: $\bar{\bar{\epsilon}}^{(4)} = 8.6\epsilon_0\bar{\bar{I}}$.

5.5.3 Influence of Material Anisotropy

For the final example considered in this chapter, we seek to investigate the influence of material's anisotropy on the DGF's. Figs. 5.5-5.13 show the magnitudes of all the nine elements of DGF's, G_{xx}^{EJ}, G_{xy}^{EJ}, G_{xz}^{EJ}, G_{yx}^{EJ}, G_{yy}^{EJ}, G_{yz}^{EJ}, G_{zx}^{EJ}, G_{zy}^{EJ}, and G_{zz}^{EJ}, respectively. For the nine figures, $z' = -0.7$ mm, $z = -0.1$ mm, $\epsilon_t^{(2)} = 2.1\epsilon_0$, $\epsilon_z^{(2)}/\epsilon_t^{(2)} = 1.5$, $\epsilon_g^{(2)}/\epsilon_0 = 0.2/2.0/20$, $\bar{\bar{\epsilon}}^{(3)} = 9.8\epsilon_0\bar{\bar{I}}$, and $\bar{\bar{\epsilon}}^{(4)} = 8.6\epsilon_0\bar{\bar{I}}$. The nine figures clearly show the influence of material's anisotropy on the Green's functions. It can be clearly seen that the off-diagonal elements of the permittivity of gyrotropic medium has insignificant influence on the Green's functions G_{xx}^{EJ}, G_{xz}^{EJ}, G_{yy}^{EJ}, G_{zx}^{EJ}, and G_{zz}^{EJ}. It is also noticed that, as the value of ϵ_g/ϵ_0 increases, the magnitudes of the Green's functions (G_{xy}^{EJ}, G_{yx}^{EJ}, G_{yz}^{EJ} and G_{zy}^{EJ}) also increase in the intermediate and far fields. This implies that in the

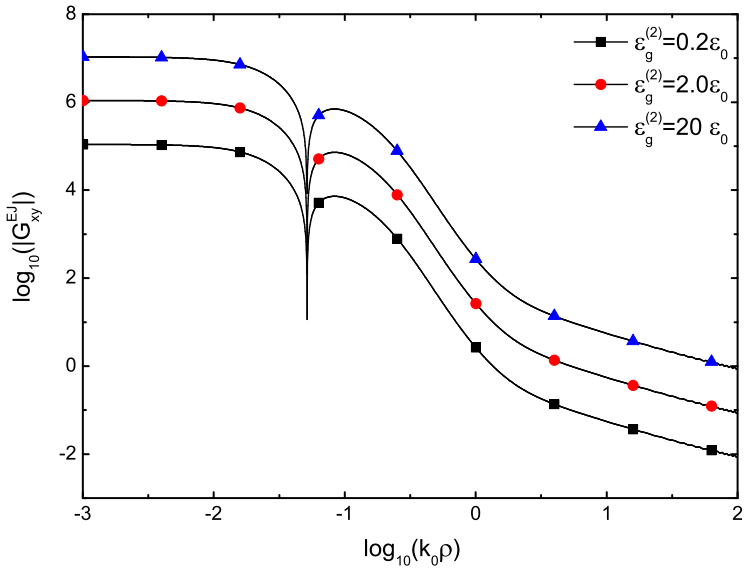

Figure 5.6: Magnitudes of G_{xy}^{EJ} versus ρ for the four-layer structure with the following parameters: m=n=2; $z' = -0.7$ mm; $z = -0.1$ mm; layer 2: $\epsilon_t^{(2)} = 2.1\epsilon_0$, $\epsilon_z^{(2)}/\epsilon_t^{(2)} = 1.5$, $\epsilon_g^{(2)}/\epsilon_0 = 0.2/2.0/20$; layer 3: $\bar{\bar{\epsilon}}^{(3)} = 9.8\epsilon_0\bar{\bar{I}}$; layer 4: $\bar{\bar{\epsilon}}^{(4)} = 8.6\epsilon_0\bar{\bar{I}}$.

multilayered medium, the value of electric field increases in the near and intermediate fields as the material's anisotropy increases. It is worth mentioning that the DGF in a gyrotropic medium is not an Hermitian matrix as in the case of isotropic and uniaxial anisotropic media, which is due to the reason that the duality formalism is not applicable to an anisotropic medium. The investigation of the material's anisotropy may provide guidelines for the development of computer-aided design tools for the electromagnetic performance prediction of optical devices and radar absorbing materials.

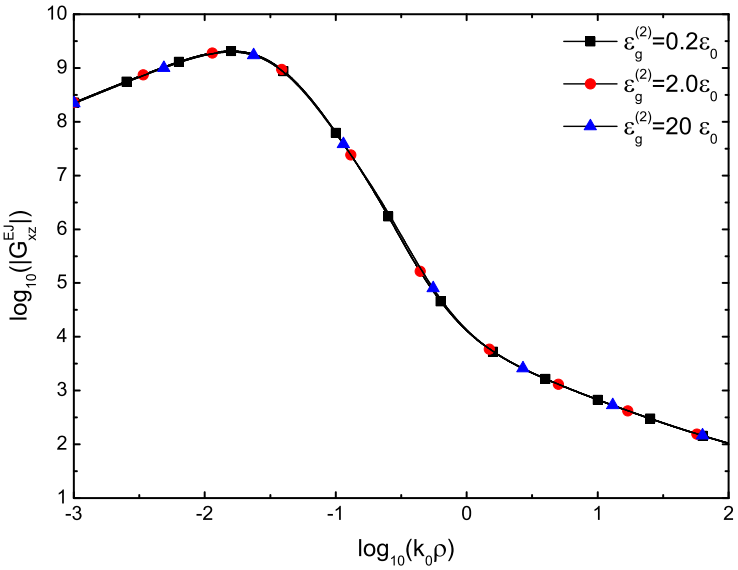

Figure 5.7: Magnitudes of G_{xz}^{EJ} versus ρ for the four-layer structure with the following parameters: m=n=2; $z' = -0.7$ mm; $z = -0.1$ mm; layer 2: $\epsilon_t^{(2)} = 2.1\epsilon_0$, $\epsilon_z^{(2)}/\epsilon_t^{(2)} = 1.5$, $\epsilon_g^{(2)}/\epsilon_0 = 0.2/2.0/20$; layer 3: $\bar{\bar{\epsilon}}^{(3)} = 9.8\epsilon_0\bar{\bar{I}}$; layer 4: $\bar{\bar{\epsilon}}^{(4)} = 8.6\epsilon_0\bar{\bar{I}}$.

5.6 Conclusion

In this chapter, a holistic and efficient algorithm has been introduced for the rigorous derivation of the DGF's in the planar multilayered gyrotropic media. The *kDB* coordinate system is employed to obtain the characteristic field vectors and the Fourier transform is exploited to derive the unbounded Green's function. One key contribution of the proposed algorithm is that a generalized set of the spectral-domain Green's function in the planar multilayered gyrotropic media has been derived. Based on the MFHT method, the fast solutions of spatial-domain Green's function are, for the first time, obtained for the multilayered gyrotropic media. To verify the accuracy of the proposed algorithm and the spatial-domain Green's function, the numerical examples are implemented in both the spectral domain and spatial domain. The numerical results have been demonstrated

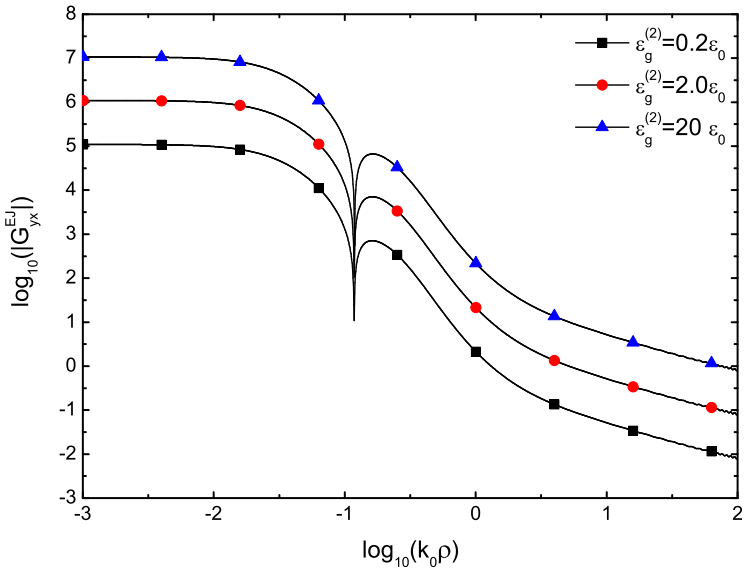

Figure 5.8: Magnitudes of G_{yx}^{EJ} versus ρ for the four-layer structure with the following parameters: m=n=2; $z' = -0.7$ mm; $z = -0.1$ mm; layer 2: $\epsilon_t^{(2)} = 2.1\epsilon_0$, $\epsilon_z^{(2)}/\epsilon_t^{(2)} = 1.5$, $\epsilon_g^{(2)}/\epsilon_0 = 0.2/2.0/20$; layer 3: $\bar{\bar{\epsilon}}^{(3)} = 9.8\epsilon_0\bar{\bar{I}}$; layer 4: $\bar{\bar{\epsilon}}^{(4)} = 8.6\epsilon_0\bar{\bar{I}}$.

to have excellent performance in both the accuracy and efficiency. The exploration of the material anisotropy's characteristic may provide guidelines for the development of computer-aided design tools for the electromagnetic performance prediction of optical devices and radar absorbing materials.

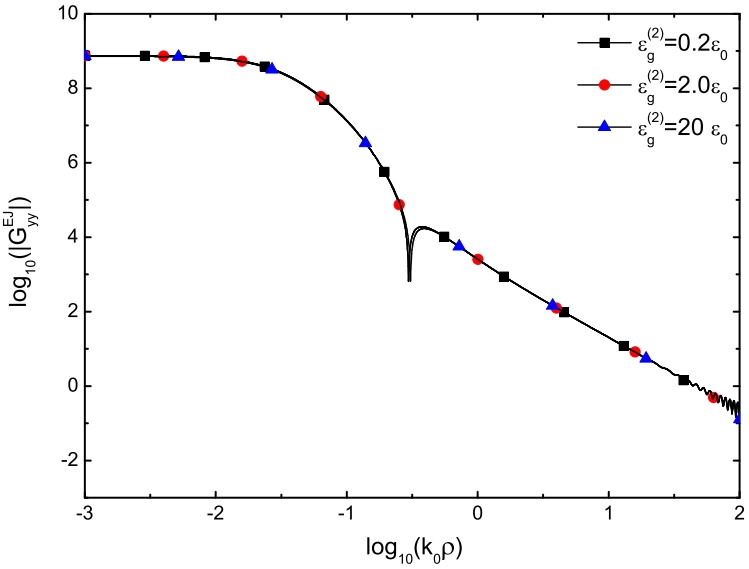

Figure 5.9: Magnitudes of G_{yy}^{EJ} versus ρ for the four-layer structure with the following parameters: m=n=2; $z' = -0.7$ mm; $z = -0.1$ mm; layer 2: $\epsilon_t^{(2)} = 2.1\epsilon_0$, $\epsilon_z^{(2)}/\epsilon_t^{(2)} = 1.5$, $\epsilon_g^{(2)}/\epsilon_0 = 0.2/2.0/20$; layer 3: $\bar{\bar{\epsilon}}^{(3)} = 9.8\epsilon_0\bar{\bar{I}}$; layer 4: $\bar{\bar{\epsilon}}^{(4)} = 8.6\epsilon_0\bar{\bar{I}}$.

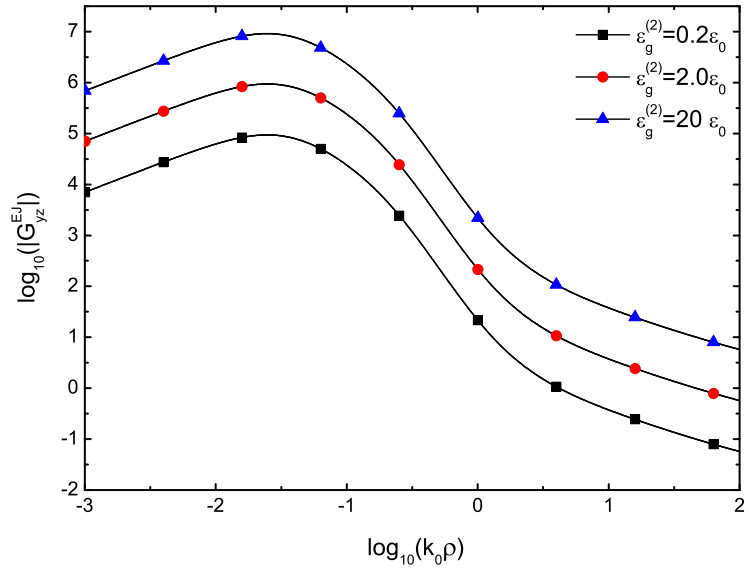

Figure 5.10: Magnitudes of G_{yz}^{EJ} versus ρ for the four-layer structure with the following parameters: m=n=2; $z' = -0.7$ mm; $z = -0.1$ mm; layer 2: $\epsilon_t^{(2)} = 2.1\epsilon_0$, $\epsilon_z^{(2)}/\epsilon_t^{(2)} = 1.5$, $\epsilon_g^{(2)}/\epsilon_0 = 0.2/2.0/20$; layer 3: $\bar{\bar{\epsilon}}^{(3)} = 9.8\epsilon_0\bar{\bar{I}}$; layer 4: $\bar{\bar{\epsilon}}^{(4)} = 8.6\epsilon_0\bar{\bar{I}}$.

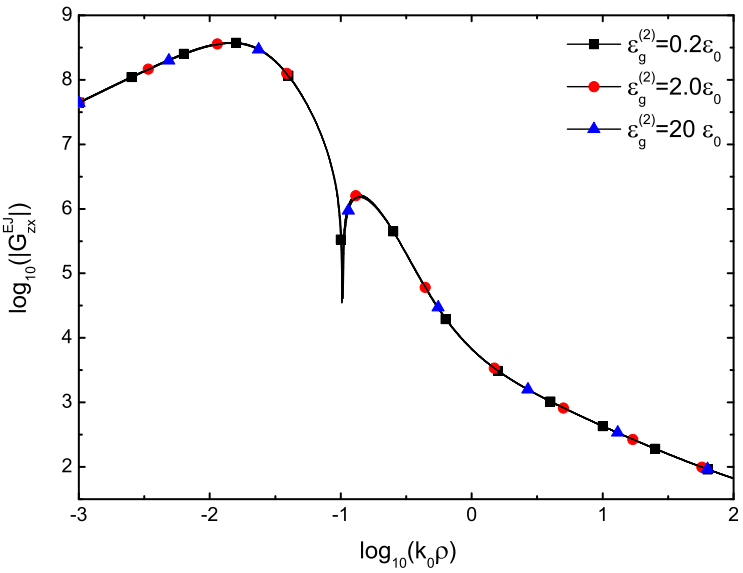

Figure 5.11: Magnitudes of G_{zx}^{EJ} versus ρ for the four-layer structure with the following parameters: m=n=2; $z' = -0.7$ mm; $z = -0.1$ mm; layer 2: $\epsilon_t^{(2)} = 2.1\epsilon_0$, $\epsilon_z^{(2)}/\epsilon_t^{(2)} = 1.5$, $\epsilon_g^{(2)}/\epsilon_0 = 0.2/2.0/20$; layer 3: $\bar{\bar{\epsilon}}^{(3)} = 9.8\epsilon_0\bar{\bar{I}}$; layer 4: $\bar{\bar{\epsilon}}^{(4)} = 8.6\epsilon_0\bar{\bar{I}}$.

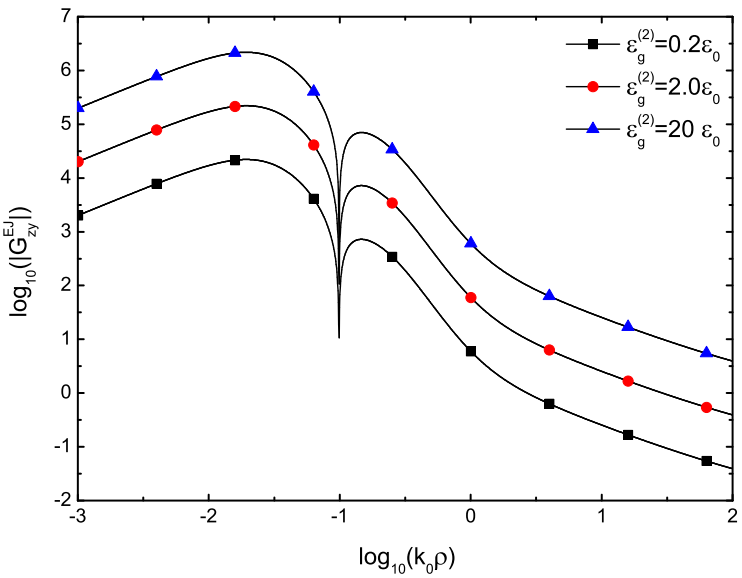

Figure 5.12: Magnitudes of G_{zy}^{EJ} versus ρ for the four-layer structure with the following parameters: m=n=2; $z' = -0.7$ mm; $z = -0.1$ mm; layer 2: $\epsilon_t^{(2)} = 2.1\epsilon_0$, $\epsilon_z^{(2)}/\epsilon_t^{(2)} = 1.5$, $\epsilon_g^{(2)}/\epsilon_0 = 0.2/2.0/20$; layer 3: $\bar{\bar{\epsilon}}^{(3)} = 9.8\epsilon_0\bar{\bar{I}}$; layer 4: $\bar{\bar{\epsilon}}^{(4)} = 8.6\epsilon_0\bar{\bar{I}}$.

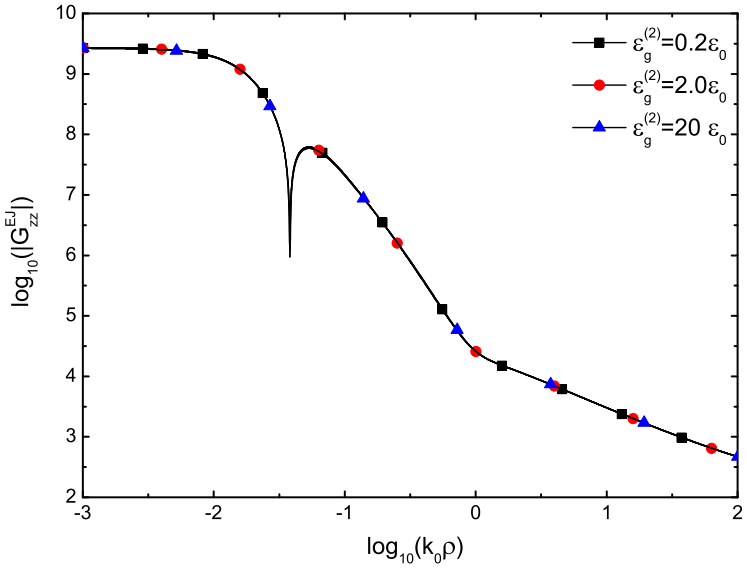

Figure 5.13: Magnitudes of G_{zz}^{EJ} versus ρ for the four-layer structure with the following parameters: m=n=2; $z' = -0.7$ mm; $z = -0.1$ mm; layer 2: $\epsilon_t^{(2)} = 2.1\epsilon_0$, $\epsilon_z^{(2)}/\epsilon_t^{(2)} = 1.5$, $\epsilon_g^{(2)}/\epsilon_0 = 0.2/2.0/20$; layer 3: $\bar{\bar{\epsilon}}^{(3)} = 9.8\epsilon_0\bar{\bar{I}}$; layer 4: $\bar{\bar{\epsilon}}^{(4)} = 8.6\epsilon_0\bar{\bar{I}}$.

Chapter 6

Conclusions

In this thesis, the traditional FHT method was improved to extend its application range to the general multilayered structure problems. It was found that the fast Hankel transform filter developed until now only permits the input function to be smooth and the FHT method is only applicable for shielded multilayered geometries. To overcome this limitation, the primary objective of the present study was to develop the MFHT method by deforming the integration path of SI from the real axis to the quadrant and expand the Bessel function with a complex argument as a sum of terms. The MFHT method has been proven to be a valuable and robust improvement of the traditional FHT method to calculate the DGF's for a general multilayered structure and successfully extend the application range of FHT method to a general multilayered structure. In view of its excellent performance in both accuracy and robustness, MFHT method can provide a powerful tool for the calculation of DGF's for a general multilayered problem. One limitation of MFHT method is that the valid distance range of MFHT method is confined to the near and intermediate fields, which can be further alleviated by applying the

extrapolation method to the extension of the valid range.

Three popular methods for calculating multilayered Green's functions, i.e., the discrete complex image method, the window function method and the modified fast Hankel transform method, were systematically studied to explain their computational theories and the selection criteria of crucial parameters. Then, for the first time, the robustness and efficiency of the three methods for the general multilayered problems were carefully examined and compared through numerical examples. Finally, through making comparisons of numerical results, we gave a critical discussion on the possible sources of errors and their remedies, as well as the advantages, restrictions and range of validity for the three fast methods. The DCIM has been shown to be powerful for calculating the DGF's in closed form for all the ranges of distance, but lack of reliable automated procedures for the complicated extraction of contribution of SWP's. WFM is also an alternative fast method for calculating the multilayered Green's functions. However, since the approximation process based on WFM requires six integral terms for calculating DGF's, the approximation is quite laborious and complicated. MFHT method has excellent performance in both accuracy and robustness. One major contribution of the studies is that discussing the valid application range of DCIM, WFM and MFHT method has provided definite answers to the questions on their disadvantages and limitations. The comparison of accuracy and efficiency for the three fast methods provides guidelines for the development of computer-aided design tools for the electromagnetic performance prediction of practical problems.

Since the practical applications of complex media in multilayered geometries have attracted considerable attention, we have successfully carried out the accurate and ex-

pedient calculation of the dyadic Green's functions in both spectral domain and spatial domain for the multilayered uniaxial anisotropic medium and gyrotropic medium. However, until now, the derivation of spectral-domain Green's function for the multilayered anisotropic media is still lack of a systematic and robust methodology. Moreover, the spatial-domain Green's function and the influence of material's anisotropy upon the DGF's for the multilayered anisotropic media has not been investigated or discussed yet. Thus, the spectral-domain Green's function was systematically derived used in the EFIE for the multilayered uniaxial anisotropic medium and gyrotropic medium, and then, the spatial-domain Green's functions in the two kinds of media were calculated based on the fast methods. More importantly, the influence of material's anisotropy upon the DGF's was investigated. The *kDB* coordinate system is exploited and integrated with the WIT to derive the spectral-domain Green's function. The study of the DGF's for the multilayered anisotropic media may be valuable to enhance the understanding of electromagnetic properties in the anisotropic media and pave the path for modeling emerging microwave and optical devices involving composite anisotropic materials.

Based on the numerical results obtained, discussion presented and conclusion drawn from this research work, some potential areas for further investigation related to the multilayered Green's function are highlighted below.

One interesting avenue for future work is the extension of calculation of DGF's to other complex media for broader application. This is progressively necessary as complex media have attracted a great deal of interest due to their salient anisotropy features and their future practical application to microwave circuits and antennas. Since the systematical and robust deriving algorithm for the multilayered anisotropic medium has

been developed, it should be feasible and straightforward to calculate the DGF's for other complex media based on the fast methods.

Another recommendable area for future work is to employ the DGF's associated with the MoM to analyze the properties of the integrated circuits and microstrip antennas involved to the multilayered problems. Since the DGF's corresponding to the multilayered environment can be calculated accurately and efficiently, it would be tempting to carry out the full wave analysis of microwave circuits and provide a powerful tool to the development of computer-aided design tools.

Another interesting area for future work is to exploit the DGF's to design and analyze the radar absorbing materials. Radar absorbing materials could be realized via multilayered anisotropic media and they are widely used in many applications, such as anechoic chambers, improving microwave systems' electromagnetic compatibility, and camouflaging military targets. Since the influence of multilayered anisotropic media on the electromagnetic fields and radar cross section can be quantitatively obtained based on the DGF's, it would be robust and effective to employ the DGF's to design a multilayered coating with minimal reflection coefficients at a specified range of frequencies.

Bibliography

[1] L. Tsang, E. Njoku, and J. A. Kong, "Microwave thermal emission from a stratified medium with nonuniform temperature distribution," *J. Appl. Phys.*, vol. 46, no. 12, pp. 5127–5133, Dec. 1975.

[2] A. Karlsson and G. Kristensson, "Electromagnetic scattering from subterranean obstacles in a stratified ground," *Radio Sci.*, vol. 18, no. 3, pp. 345–356, 1983.

[3] P. E. Wannamaker, G. W. Hohmann, and W. A. SanFilipo, "Electromagnetic modeling of three-dimensional bodies in layered earths using integral equations," *Geophys.*, vol. 49, pp. 60–74, Jan. 1984.

[4] R. H. Hardman and L. C. Shen, "Theory of undcution sonde in depping beds," *Geophys.*, vol. 51, no. 3, pp. 800–809, Mar. 1986.

[5] J. S. Bagby, D. P. Nyquist, and B. C. Drachman, "Integral formulation for analysis of integrated dielectric waveguides," *IEEE Trans. Microwave Theory Tech.*, vol. 33, no. 10, pp. 906–915, Oct. 1985.

[6] P. S. Hall, "Probe compensation in thick microstrip patches," *Electron. Lett.*, vol. 23, no. 11, pp. 606–607, May 1987.

[7] S. M. A. A. N. Tulintseff and J. A. Kong, "Input impedance of a probe-fed stacked circular microstrip antenna," *IEEE Trans. Antennas Propagat.*, vol. 39, no. 3, pp. 381–390, Mar. 1991.

[8] S. D. Targonski, R. B. Waterhouse, and D. M. Pozar, "Design of wide-band aperture-stacked patch microstrip antennas," *IEEE Trans. Antennas Propagat.*, vol. 46, no. 9, pp. 1245–1251, Sep. 1998.

[9] A. K. Bhattacharyya, *Electromagnetic Fields in Multilayered Structures: Theory and Applications*. Boston: Artech House, 1993.

[10] J. R. Mosig, "Arbitrarily shaped microstrip structures and their analysis with a mixed potential integral equation," *IEEE Trans. Microwave Theory Tech.*, vol. 36, no. 2, pp. 314–323, Feb. 1988.

[11] S. Barkeshli, P. H. Pathak, and M. Marin, "An asymptotic closed-form microstrip surface Green's function for the efficient moment method analysis of mutual coupling in microstrip antennas," *IEEE Trans. Antennas Propagat.*, vol. 38, no. 9, pp. 1374–1383, Sep. 1990.

[12] L. Barlately, J. R. Mosig, and T. Sphicopoulos, "Analysis of stacked microstrip patches with a mixed potential integral equation," *IEEE Trans. Antennas Propagat.*, vol. 38, no. 5, pp. 608–615, May 1990.

[13] I. R. M. I. Park and M. I. Aksun, "Numerical efficient analysis of planar microstrip configurations using closed-form green's functions," *IEEE Trans. Microwave Theory Tech.*, vol. 43, no. 2, pp. 390–400, Feb. 1995.

[14] L.-W. Li, P.-S. Kooi, M.-S. Leong, T.-S. Yeo, and S.-L. Ho, "Input impedance of a probe-excited semi-infinite rectangular waveguide with arbitrary multilayered loads: part I-dyadic Green's functions," *IEEE Trans. Microwave Theory Tech.*, vol. 45, no. 7, pp. 1559–1566, July 1995.

[15] M. J. Tsai, F. D. Flavis, O. Fordharn, and N. G. Alexopoulos, "Modeling planar arbitrarily shaped microstrip elements in multilayered media," *IEEE Trans. Microwave Theory Tech.*, vol. 45, no. 3, pp. 330–337, Mar. 1997.

[16] R. C. Hsieh and J. T. Ku, "Fast full-wave analysis of planar microstrip circuit elements in stratified media," *IEEE Trans. Microwave Theory Tech.*, vol. 46, no. 9, pp. 1291–1297, Sep. 1998.

[17] J. Yeo and R. Mittra, "An algorithm for interpolating the frequency variations of method-of-moments matrics arising in the analysis of planar microstrip structures," *IEEE Trans. Microwave Theory Tech.*, vol. 51, no. 3, pp. 1018–1025, Mar. 2003.

[18] T. F. Elshafiey and J. T. Aberle, "Green's function for multilayer arbitrarily biased anisotropic structures-application to phase shifters, transducers, and magnetization angle effect," *IEEE Trans. Microwave Theory Tech.*, vol. 54, no. 2, pp. 513–521, Feb. 2006.

[19] R. F. Harrington, *Field Computations by Moment Methods*. New York: Macmillan, 1968.

[20] K. A. Michalski and D. Zheng, "Electromagnetic scattering and radiation by surface of arbitrary shape in layered mediadpart i: Theory," *IEEE Trans. Antennas Propagat.*, vol. 38, no. 3, pp. 335–344, Mar. 1990.

[21] K. A. Michalski, "Formulation of mixed-potential integral equations for arbitrarily shaped microstrip structures with uniaxial substrates," *Journal of Electromagnetic Waves and Applications*, vol. 7, no. 7, pp. 899–917, 1993.

[22] R. W. Jackson, "The use of side wall images to compute package effects in MoM analysis of MMIC circuits," *IEEE Trans. Microwave Theory Tech.*, vol. 41, no. 3, pp. 406–414, Mar. 1993.

[23] M.-H. Ho, K. A. Michalski, and K. Chang, "Waveguide excited microstrip patch antenna-theory and experiment," *IEEE Trans. Antennas Propagat.*, vol. 42, no. 8, pp. 1114–1125, Aug. 1994.

[24] K. A. Michalski and J. R. Mosig, "Multilayered media Green's functions in integral equation formulations," *IEEE Trans. Antennas Propagat.*, vol. 45, no. 3, pp. 508–519, Mar. 1997.

[25] L.-W. Li, P.-S. Kooi, M.-S. Leong, T.-S. Yeo, and S.-L. Ho, "Input impedance of a probe-excited semi-infinite rectangular waveguide with arbitrary multilayered loads: part II-a full-wave analysis," *IEEE Trans. Microwave Theory Tech.*, vol. 45, no. 3, pp. 321–329, Mar. 1997.

[26] T. Itoh and R. Mittra, "Spectral-domain approach for calculating the dispersion characteristics of microstrip lines," *IEEE Trans. Microwave Theory Tech.*, vol. 21, no. 7, pp. 496–499, July 1973.

[27] T. Itoh, "Spectral domain immitance approach for dispersion characteristics of generalized printed transmission lines," *IEEE Trans. Microwave Theory Tech.*, vol. 28, no. 7, pp. 733–736, July 1980.

[28] P. B. Katehi and N. G. Alexópoulos, "On the modeling of electromagnetically coupled microstrip antennas-the printed strip dipole," *IEEE Trans. Antennas Propagat.*, vol. 32, no. 11, pp. 1179–1186, Nov. 1984.

[29] R. W. Jackson and D. M. Pozar, "Full-wave analysis of microstrip open-end and gap discontinuities," *IEEE Trans. Microwave Theory Tech.*, vol. 33, no. 10, pp. 1036–1042, Oct. 1985.

[30] W. C. Chew, *Wave and Fields in Inhomogeneous Media*. New York: IEEE, 1995.

[31] K. A. Michalski, "Extrapolation methods for Sommerfeld integral tails," *IEEE Trans. Antennas Propagat.*, vol. 46, no. 10, pp. 1405–1418, Oct. 1998.

[32] F. Ling and J. M. Jin, "Discrete complex image method for Green's functions of general multilayer media," *IEEE Microw. Guided Wave Lett.*, vol. 10, no. 10, pp. 400–402, Oct. 2000.

[33] Y. Liu, L.-W. Li, T.-S. Yeo, P.-S. Kooi, and M.-S. Leong, "Calculation of spatial-domain Green functions for multiayered media using DCIM with automatic han-

dling of surface wave poles," *IEE Proc. Microw. Antennas Propag.*, vol. 151, no. 3, pp. 236–240, Jun. 2004.

[34] T. Sphicopoulos, V. Teodoridis, and F. E. Gardiol, "Dyadic Green function for the electromagnetic field in multilayer isotropic media: an operator approach," *Proc. Inst. Elect. Eng.*, vol. 132, no. pt. H, pp. 329–334, Aug. 1985.

[35] D. H. S. Cheng, "On the formulation of the dyadic Green's function in a layered medium," *Electromagn.*, vol. 6, no. 2, pp. 171–182, 1986.

[36] L. Vegni, R. Cicchetti, and P. Capece, "Spectral dyadic Green's function formulation for planar integrated structures," *IEEE Trans. Antennas Propagat.*, vol. 36, no. 8, pp. 1057–1065, Aug. 1988.

[37] M. I. Aksun and R. Mittra, "Derivation of closed-form Green's functions for a general microstrip geometry," *IEEE Trans. Microwave Theory Tech.*, vol. 40, no. 11, pp. 2055–2062, Nov. 1992.

[38] N. Kinayman and M. I. Aksun, "Comparative study of acceleration techniques for integrals and series in electromagnetic problems," *Radio Sci.*, vol. 30, no. 6, pp. 1713–1722, Nov.-Dec. 1995.

[39] Y. Ge and K. P. Esselle, "New closed-form Green's functions for microstrip structures theory and results," *IEEE Trans. Microwave Theory Tech.*, vol. 50, no. 6, pp. 1556–1560, June 2002.

[40] V. N. Kourkoulos and A. C. Cangellaris, "Accurate approximation of Green's functions in planar stratified media in terms of a finite sum of spherical and cylin-

drical waves," *IEEE Trans. Antennas Propagat.*, vol. 54, no. 5, pp. 1568–1576, May 2006.

[41] R. R. Boix, F. Mesa, and F. Medina, "Application of total least squares to the derivation of closed-form Green's functions for planar layered media," *IEEE Trans. Microwave Theory Tech.*, vol. 55, no. 2, pp. 268–280, Feb. 2007.

[42] Y. L. Chow, J. J. Yang, D. G. Fang, and G. E. Howard, "A closed-form spatial Green's function for the thick microstrip substrate," *IEEE Trans. Microwave Theory Tech.*, vol. 39, no. 3, pp. 588–592, Mar. 1991.

[43] M. I. Aksun, "A robust approach for the derivation of closed-form Green's functions," *IEEE Trans. Microwave Theory Tech.*, vol. 44, no. 5, pp. 651–658, May 1996.

[44] Y. Liu, L.-W. Li, T.-S. Yeo, and M.-S. Leong, "Application of DCIM to MPIE-MoM analysis of 3-D PEC objects in multilayered media," *IEEE Trans. Antennas Propagat.*, vol. 50, no. 2, pp. 157–162, Feb. 2002.

[45] N. V. Shuley, R. R. Boix, F. Medina, and M. Horno, "On the fast approximation of Green's functions in MPIE formulations for planar layered media," *IEEE Trans. Microwave Theory Tech.*, vol. 50, no. 9, pp. 2185–2192, Sep. 2002.

[46] V. I. Okhmatovski and A. C. Cangellaris, "Evaluation of layered media Green's functions via rational function fitting," *IEEE Microw. Wireless Compon. Lett.*, vol. 14, no. 1, pp. 22–24, Jan. 2004.

[47] M. Yuan, T. K. Sarkar, and M. Salazar-Palma, "A direct discrete complex image method from the closed-form Green's functions in multilayered media," *IEEE Trans. Microwave Theory Tech.*, vol. 54, no. 3, pp. 1025–1032, Mar. 2006.

[48] L. Zhuang, G. Zhu, Y. Zhang, and B. Xiao, "An improved discrete complex image method for Green's functions in multilayered media," *Microw. Opt. Technol. Lett.*, vol. 49, no. 6, pp. 1337–1340, June 2007.

[49] A. G. Polimeridis, T. V. Yioultsis, and T. D. Tsiboukis, "An efficient pole extraction technique for the computation of Green's function in stratified media using a sine transformation," *IEEE Trans. Antennas Propagat.*, vol. 55, no. 1, pp. 227–229, Jan. 2007.

[50] F. Mesa, R. R. Boix, and F. Medina, "Closed-form expressions of multilayered planar Green's functions that account for the continuous spectrum in the far field," *IEEE Trans. Microwave Theory Tech.*, vol. 56, no. 7, pp. 1601–1614, July 2008.

[51] A. Alparslan, M. I. Aksun, and K. A. Michalski, "Closed-form Green's functions in planar layered media for all ranges and materials," *IEEE Trans. Microwave Theory Tech.*, vol. 58, no. 3, pp. 602–613, Mar. 2010.

[52] Q. H. Liu and W. C. Chew, "Application of the conjugate gradient fast Fourier Hankel transfer method with an improved fast Hankel transform algorithm," *Radio Sci.*, vol. 29, pp. 1009–1022, Aug. 1994.

[53] R. C. Hsieh and J. T. Kuo, "Fast evaluation of the Sommerfeld integrals for Green's functions of open microsrip structures," *IEEE AP-S Int. Symp.*, vol. 4, pp. 1826–1829, Jun. 1998.

[54] T. J. Cui and W. C. Chew, "Fast evaluation of Sommerfeld integrals for EM scattering and radiation by three-dimensional buried objects," *IEEE Trans. Geosci. Remte Sensing.*, vol. 37, no. 2, pp. 887–900, Mar. 1999.

[55] W. Cai and T.-J. Yu, "Fast calculations of dyadic Green's functions for electromagnetic scattering in a multilayer medium," *J. Comput. Phys.*, vol. 165, pp. 1–21, Nov. 2000.

[56] M. Brun, S. Guenneau, and A. B. Movchan, "Achieving control of in-plane elastic waves," *Applied Physics Letters*, vol. 94, no. 6, p. 061903, Feb. 2009.

[57] B. Chapuis, N. Terrien, and D. Royer, "Excitation and focusing of lamb waves in a multilayered anisotropic plate," *Journal of the Acoustical Society of America*, vol. 127, no. 1, pp. 193–203, Jan. 2010.

[58] W. Shu, X. Lv, H. Luo, and S. Wen, "Green's function integral equation method for propagation of electromagnetic waves in an anisotropic dielectric-magnetic slab," *Conference on Metamaterials: Foundamentals and Applications III*, vol. 7754, Aug. 2010.

[59] J. J. Ramsey, E. Pan, W. W. Chung, and Z. M. Wang, "Superlattice growth via MBE and Green's function techniques," *Nanoscale Research Letters*, vol. 5, no. 8, pp. 1272–1278, Aug. 2010.

[60] T. Iwayama and T. Watanabe, "Green's function for a generalized two-dimensional fluid," *Phys. Rev. E*, vol. 82, no. 3, p. 036307, Sep. 2010.

[61] C. M. Krowne, "Determination of the Green's function in the spectral domain using a matrix method: Application ot radiators or resonators immersed in a complex anisotropic layered medium," *IEEE Trans. Antennas Propagat.*, vol. 34, pp. 247–253, Feb. 1986.

[62] J. L. Tsalamengas, "Interaction of electromagnetic waves with general bianisotropic slabs," *IEEE Trans. Microwave Theory Tech.*, vol. 40, no. 10, pp. 1870–1878, Aug. 1992.

[63] F. Olyslager and D. D. Zutter, "Rigorous full-wave analysis of electric and dielectric waveguides embedded in a multilayered bianisotropic medium," *Radio Sci.*, vol. 28, no. 5, pp. 937–946, Sep. 1993.

[64] L.-W. Li, J.-H. Koh, T.-S. Yeo, M.-S. Leong, and P.-S. Kooi, "Analysis of radiowave progapagtion in a four-layered anisotropic forest environment," *IEEE Trans. Geosci. Remote Sensing*, vol. 37, no. 4, pp. 1967–1979, July 1999.

[65] G. Antonini, "Advanced models for transient analysis of lossy and dispersive anisotropic planar layers," *International Journal of Numerical Modelling-Electronic Networks Devices and Fields*, vol. 23, no. 1, pp. 1–19, Jan.-Feb. 2010.

[66] C. T. Tai, *Dyadic Green Functions in Electromagnetic Theory*. New York: IEEE, 1993.

[67] L.-W. Li, J.-H. Koh, T.-S. Yeo, M.-S. Leong, and P.-S. Kooi, "Cylindrical vector eigenfunction expansion of Green dyadics for multilayered anisotropic media and its application to four-layered forest," *IEEE Trans. Antennas Propagat.*, vol. 52, no. 2, pp. 466–477, Feb. 2004.

[68] S. M. Ali and S. F. Mahmoud, "Electromagnetic fields of buried sources in stratified anisotropic media," *IEEE Trans. Antennas Propagat.*, vol. 27, no. 5, pp. 671–678, Sep. 1979.

[69] J. K. Lee and J. A. Kong, "Dyadic Green's functions for layered anisotropic medium," *Electromagn.*, vol. 3, no. 2, pp. 110–130, Apr. 1983.

[70] T. M. Habashy, S. M. Ali, J. A. Kong, and M. D. Grossi, "Dyadic Green's functions in a planar stratified, arbitrarily magnetized linear plasma," *rs*, vol. 26, no. 3, pp. 701–715, May-June 1991.

[71] R. H. Jansen, "The spectral-domain approach for microwave integrated circuits," *IEEE Trans. Microwave Theory Tech.*, vol. 33, no. 10, pp. 1043–1056, Oct. 1985.

[72] D. M. Pozar and S. M. Voda, "A rigorous analysis of a microstrip feed patch antenna," *IEEE Trans. Antennas Propagat.*, vol. 35, no. 12, pp. 1343–1350, Dec. 1987.

[73] S. Wu, H. Y. Yang, N. G. Aexopoulous, and I. Wolff, "A rigorous dispersive characterization of microstrip cross and T junctions," *IEEE Trans. Microwave Theory Tech.*, vol. 38, no. 12, pp. 1837–1844, Dec. 1990.

[74] W. Schwab and W. Menzel, "On the design of planar microwave components using multilayer structures," *IEEE Trans. Microwave Theory Tech.*, vol. 40, no. 1, pp. 67–72, Jan. 1992.

[75] M. I. Aksun and R. Mittra, "Choices of expansion and testing functions for the method of moments in electromagnetic problems," *IEEE Trans. Microwave Theory Tech.*, vol. 41, no. 3, pp. 503–509, Mar. 1993.

[76] D. C. Chang and J. X. Zheng, "Electromagnetic modeling of passive circuit elements in mmic," *IEEE Trans. Microwave Theory Tech.*, vol. 40, no. 9, pp. 1741–1747, Sep. 1992.

[77] R. A. Kipp, C. H. Chan, A. T. Yang, and J. T. Yao, "Simulation of high-frequency integrated circuits incorporating full-wave analysis of microstrip discontinuities," *IEEE Trans. Microwave Theory Tech.*, vol. 41, no. 5, pp. 848–854, May 1993.

[78] R. Gillard, J. Corre, M. Drissi, and J. Citerne, "A general treatment of matched terminations using integral equations-modeling and application," *IEEE Trans. Microwave Theory Tech.*, vol. 42, no. 12, pp. 2545–2553, Dec. 1994.

[79] T. J. Cui, W. Wiesbeck, and A. Herschlein, "Electromagnetic scattering by multiple three-dimensional scatterers buried under multilayered media-part I: Theory," *IEEE Trans. Geosci. Remote Sensing*, vol. 36, no. 2, pp. 526–534, Mar. 1998.

[80] J. L. Tsalamengas and N. Uzunoglu, "Radiation from a dipole in the proximity of a general anisotropic grounded layer," *IEEE Trans. Antennas Propagat.*, vol. 33, no. 2, pp. 165–172, Feb. 1985.

[81] J. L. Tsalamengas, "Electromagnetic fields of elementary dipole antennas embedded in stratified general gyrotropic media," *IEEE Trans. Antennas Propagat.*, vol. 37, no. 3, pp. 399–403, Mar. 1989.

[82] J. L. Tsalamengas and N. K. Uzunoglu, "Radiation from a dipole near a general anisotropic layer," *IEEE Trans. Antennas Propagat.*, vol. 38, no. 1, pp. 9–16, Jan. 1990.

[83] E. L. Tan and S. Y. Tan, "Unbounded and scattered field representations of the dyadic Green's functions for planar stratified bianisotropic media," *IEEE Trans. Antennas Propagat.*, vol. 49, no. 8, pp. 1218–1225, Aug. 2001.

[84] A. Erteza and B. K. Park, "Nonuniqueness of resolution of Hertz vector in presence of a boundary, and a horizontal dipole problem," *IEEE Trans. Antennas Propagat.*, vol. 17, no. 3, pp. 376–378, May 1969.

[85] S. M. Rao, D. R. Wilton, and A. W. Glisson, "Electromagnetic scattering by surfaces of arbitrary shape," *IEEE Trans. Antennas Propagat.*, vol. 30, no. 3, pp. 409–418, May 1982.

[86] R. Bunger and F. Arndt, "Efficient MPIE approach for the analysis of three-dimensional microstrip structures in layered media," *IEEE Trans. Microwave Theory Tech.*, vol. 45, no. 8, pp. 1141–1153, Aug. 1997.

[87] N. Kinayman and M. I. Aksun, "Efficient use of closed-form Green's functions for the analysis of planar geometries with vertical connections," *IEEE Trans. Microwave Theory Tech.*, vol. 45, no. 5, pp. 593–603, May 1997.

[88] A. W. Glisson and D. R. Wilton, "Simple and efficient numerical methods for problems of electromagnetic radiation and scattering from surfaces," *IEEE Trans. Antennas Propagat.*, vol. 28, no. 5, pp. 593–603, Sep. 1980.

[89] J. R. Mosig and F. E. Gardiol, "General integral equation formulation for microstrip antennas and scatterers," *Inst. Elec. Eng., Proc.*, vol. 132, no. pt. H, pp. 424–432, Dec. 1985.

[90] W. A. Johnson, "Analysis of vertical, tubular cylinder which penetrates an air-dielectric interface and which is excited by an azimuthally symmetric source," *Radio Sci.*, vol. 18, no. 6, pp. 1273–1281, Nov.-Dec. 1983.

[91] K. A. Michalski, "The mixed-potential electric field integral equation for objects in layered media," *Arch. Elek. Übertragung.*, vol. 39, no. 5, pp. 317–322, Sep.-Oct. 1985.

[92] K. A. Michalski and D. Zheng, "Electromagnetic scattering and radiation by surface of arbitrary shape in layered mediadpart ii: Implementation and results for contiguous halp-space," *IEEE Trans. Antennas Propagat.*, vol. 38, pp. 345–352, Mar. 1990.

[93] ——, "Rigorous analysis of open microstrip lines of arbitrary cross section in bound and leaky regimes," *IEEE Trans. Microwave Theory Tech.*, vol. 37, no. 12, pp. 2005–2010, Dec. 1989.

[94] D. Zheng and K. A. Michalski, "Analysis of arbitrarily shaped coax-fed microstrip antennas with thick substrates," *Electronics Letters*, vol. 26, no. 12, pp. 794–795, June 1990.

[95] N. W. Montgomery and D. R. Wilton, "Analysis of arbitrary conducting periodic structures embedded in layered media," *Dig. IEEE AP-S Int. Symp.*, vol. 3, pp. 1889–1892, June 1990.

[96] J. Chen, A. A. Kishk, and A. W. Glisson, "MPIE for conducting sheets penetrating a multilayer medium," *Dig. IEEE AP-S Int. Symp.*, vol. 2, pp. 1346–1349, June 1994.

[97] F. Mesa and F. Medina, "Numerical computation of the space-domain mixed potential Gree's functions for planar layered structures with arbitrarily magnetized ferrites," *IEEE Trans. Antennas Propagat.*, vol. 52, no. 11, pp. 3019–3024, Nov. 2004.

[98] D. C. Fang, J. J. Yang, and G. Y. Desisle, "Discrete image theory for horizontal electric dipoles in a multilayered medium," *Proc. Inst. Elect. Eng.*, vol. 135, no. pt. H, pp. 297–303, Oct. 1988.

[99] R. W. Hamming, *Numerical Methods for Scientists and Engineers*. New York: Dover Publications, 1973.

[100] G. Dural and M. I. Aksun, "Closed-form green's function for general sources and stratified media," *IEEE Trans. Microwave Theory Tech.*, vol. 43, no. 7, pp. 1545–1552, July 1995.

[101] Y. Hua and T. K. Sarkar, "Generalized pencil-of-function method for extracting poles of an EM system from its transient response," *IEEE Trans. Antennas Propagat.*, vol. 37, no. 2, pp. 229–234, Feb. 1989.

[102] M. I. Aksun and G. Dural, "Clarification of issues on the closed-from Green's functions in stratified media," *IEEE Trans. Antennas Propagat.*, vol. 53, no. 11, pp. 3644–3653, Nov. 2005.

[103] D. P. Ghosh, "The application of linear filter theory to the direct interpretatin of geoelectrical resistivity sounding measurements," *Geophys. Prospecting*, vol. 19, no. 2, pp. 192–217, June 1971.

[104] ——, "Inverse filter coefficients for the computation of apparent resistivity standard curves for a horizontally stratified earth," *Geophys. Prospecting*, vol. 19, no. 4, pp. 769–775, Dec. 1971.

[105] U. C. Das and D. P. Ghosh, "The determination of filter coefficients for the computation of standard curves for dipole resistivity sounding over layered earch by linear digital filtering," *Geophys. Prospecting*, vol. 22, no. 4, pp. 765–780, Dec. 1974.

[106] H. K. Johansen, "An interactive computer/graphic-display-terminal system for interpretation of resistivity soundings," *Geophys. Prospecting*, vol. 23, no. 3, pp. 449–458, Sep. 1975.

[107] M. Bernabini and E. Cardarelli, "The use of filtered Bessel functions in direct interpretation of geoelectrical soundings," *Geophys. Prospecting*, vol. 26, no. 4, pp. 841–852, Dec. 1978.

[108] W. L. Anderson, "Numerical integration of related Hankel transforms of orders 0 and 1 by adaptive digital filtering," *Geophysics*, vol. 44, no. 7, pp. 1287–1305, July 1979.

[109] ——, "A hybrid fast Hankel transform algorithm for electromagnetic modeling," *Geophysics*, vol. 54, no. 2, pp. 263–266, Feb. 1989.

[110] N. B. Christensen, "Optimized fast Hankel transform filters," *Geophys. Prospecting*, vol. 38, no. 5, pp. 545–568, Jul. 1990.

[111] S.-A. Teo, M.-S. Leong, S.-T. Chew, and B.-L. Ooi, "Complete location of poles for thick lossy grounded dielectric slab," *IEEE Trans. Microwave Theory Tech.*, vol. 50, no. 2, pp. 440–445, Feb. 2002.

[112] I. Daubechies, *Ten Lectures on Wavelets*. Philadephia: SIAM, 1992.

[113] S. M. Ali, T. M. Habashy, and J. A. Kong, "Spectral-domain dyadic Green's function in layered chiral media," *J. Opt. Soc. Am. A*, vol. 9, no. 3, pp. 413–423, 1992.

[114] N. Engheta, D. L. Jaggard, and M. W. Kowarz, "Electromagnetic waves in faraday chiral media," *IEEE Trans. Antennas Propagat.*, vol. 40, no. 4, pp. 367–374, Apr. 1992.

[115] S. Barkeshli, "Electromagnetic dyadic Green's functions for multilayered symmetric gyroelectric media," *Radio Sci.*, vol. 28, no. 1, pp. 23–36, Jan.-Feb. 1993.

[116] S. A. Tretyakov and A. A. Sochava, "Proposed composite material for nonreflecting shields and antenna radomes," *Electron. Lett.*, vol. 29, no. 12, pp. 1048–1049, June 1993.

[117] S. Mudaliar and J. K. Lee, "Dyadic Green's functions for a two-layer biaxially anisotropic medium," *J. Electromagnetic Waves Applicat.*, vol. 10, no. 7, pp. 909–923, Jan. 1996.

[118] W. Ren, "Dyadic Green's functions and dipole radiations in layered chiral media," *J. Appl. Phys.*, vol. 75, no. 1, pp. 30–35, Jan. 1994.

[119] C. W. Qiu, S. Zouhdi, and A. Razek, "Modified spherical wave functions with anisotropy ratio: application ot the analysis of scattering by multilayered anisotropic shells," *IEEE Trans. Antennas Propagat.*, vol. 55, no. 12, pp. 3515–3523, Dec. 2007.

[120] W. W. Hansen, "A new type of expansion in radiation problems," *Phys. Rev.*, vol. 47, no. 2, pp. 139–143, Jan. 1935.

[121] ——, "Directional characteristics of any antenna over a plane earth," *J. Appl. Phys.*, vol. 7, no. 12, pp. 460–465, Dec. 1936.

[122] P. H. Pathak, "On the eigenfunction expansion of electromagnetic dyadic Green's functions," *IEEE Trans. Antennas Propagat.*, vol. 31, no. 6, pp. 837–846, Nov. 1983.

[123] J. A. Kong, *Electromagnetic Wave Theory*. Canada: John Wiley Sons, 1986.

[124] G. Dural and M. I. Aksun, "Closed-form Green's functions for general sources and stratified media," *IEEE Trans. Microwave Theory Tech.*, vol. 43, no. 7, pp. 1545–1552, July 1995.

[125] C. H. Stoyer, "Electromagnetic fields of dipoles in stratified media," *IEEE Trans. Antennas Propagat.*, vol. 25, no. 4, pp. 547–552, July 1977.

[126] M. Zhang, L. W. Li, and Y. F. Tian, "An efficient approach for extracting poles of Green's functions in general multilayered media," *IEEE Trans. Antennas Propagat.*, vol. 56, no. 1, pp. 269–273, Jan. 2008.

[127] P. Ylä-Oijala and M. Taskinen, "Multilayered media Green's functions for MPIE with general electric and magnetic sources by the Hertz potential approach," *Prog. Electromagnetic Res.*, vol. 33, pp. 141–165, 2001.

[128] W. L. Anderson, "Fast Hankel transforms using related and lagged convolutions," *ACM Trans. Mathe. Software*, vol. 8, no. 4, pp. 344–368, Dec. 1982.

[129] D. Guptasarma and B. Singh, "New digital linear filters for hankel J_0 and J_1 transforms," *IEEE Trans. Microwave Theory Tech.*, vol. 45, no. 5, pp. 745–762, Sep. 1997.

[130] F. N. Kong, "Hankel transform filters for dipole antenna radiation in a conductive medium," *Geophysical Prospecting*, vol. 55, no. 1, pp. 83–89, Jan. 2007.

[131] H. K. Johansen and K. Sørensen, "Fast Hankel transforms," *Geophys. Prospecting*, vol. 27, pp. 876–901, 1979.

[132] M. Abramowitz and I. A. Stegun, *Hankbook of Mathematical Function*. New York: Dover Publications, 1972.

[133] C. J. Ong and L. Tsang, "Time domain Green's functions for lossy and dispersive multilayered media," *IEEE Microw. Wireless Compon. Lett.*, vol. 13, no. 9, pp. 339–401, Sep. 2003.

[134] A. R. Djordjević, R. M. Biljić, V. D. Likar-Smilianić, and T. K. Sarkar, "Wideband frequency-domain characterization of FR-4 and time-domain causality," *IEEE Trans. Electromagn. Compat.*, vol. 43, no. 4, pp. 662–667, Nov. 2001.

[135] J. Bernal, F. Medina, and R. R. Boix, "Full-wave analysis of nonplanar transmission lines in layered medium by means of MPIE and complex image theory," *IEEE Trans. Microwave Theory Tech.*, vol. 49, no. 1, pp. 177–185, Jan. 2001.

[136] R. R. Boix, A. L. Fructos, and F. Mesa, "Closed-form uniform asymptotic expansions of Green's functions in layered media," *IEEE Trans. Antennas Propagat.*, vol. 58, no. 9, pp. 2934–2945, Sep. 2010.

[137] A. J. Mackay and A. Cc, "An improved pencil-of-function method and comparisons with traditional methods of pole extraction," *IEEE Trans. Antennas Propagat.*, vol. 35, no. 4, pp. 435–441, Apr. 1987.

[138] B. P. Wu and L. Tsang, "Fast compuation of layered medium Green's functions of multilayers and lossy media using fast all-modes methods and numerical modi-

fied steepest descent path method," *IEEE Trans. Microwave Theory Tech.*, vol. 56, no. 6, pp. 1446–1454, June 2008.

[139] N. Hojjat, S. Safavi-Naeini, and Y. L. Chow, "Numerical computation of complex image Green's functions for multilayer dielectric media: near-field zone and the interface region," *Proc. Inst. Elect. Eng.-Microw. Antennas Propag.*, vol. 145, no. 6, pp. 449–454, Dec. 1998.

[140] N. Felsen and L. B. Marcuvitz, *Radiation and Scattering of Waves*. New York: Wiley, 1994.

[141] W. C. Chew, "Sommerfeld integrals for left-handed materials," *Microw. Opt. Technol. Lett.*, vol. 42, no. 5, pp. 369–373, July 2004.

[142] W. Shu and J. Song, "Sommerfeld integration path for double negative metamaterials," *IEEE AP-S Int. Symp.*, pp. 1–4, July 2008.

[143] J. R. Wait, "Fields of a horizontal dipole over a stratified anisotropic half-space," *IEEE Trans. Antennas Propagat.*, vol. 14, no. 6, pp. 790–792, Nov. 1966.

[144] J. A. Kong, "Electromagnetic fields due to dipole antennas over stratified anisotropic media," *Geophysics*, vol. 37, no. 6, pp. 985–996, Dec. 1972.